University of Nottingham
UK | CHINA | MALAYSIA

The interplay of ascorbic acid and collagen deposition in the extracellular matrix of paediatric medulloblastoma

Thesis submitted to the University of Nottingham for the degree of

Master of Research

November 2025

Menil Dholakia BSc

Supervisors: Prof Ian Kerr and Prof Beth Coyle

University of Nottingham

ABSTRACT

Medulloblastoma is the most common malignant paediatric brain tumour, accounting for roughly 20% of all paediatric cancers of the central nervous system (CNS). Medulloblastoma can be divided into four molecular subgroups: Wingless (WNT), Sonic Hedgehog (SHH), Group 3 and Group 4. SHH medulloblastoma is prevalent in infants (0-3 years) and adults. Current multimodal treatments, such as maximal surgical resection, craniospinal irradiation, and chemotherapy, have improved patient survival; however, they are still associated with significant long-term neurocognitive side effects in infants and the current treatment regimen does not eliminate the chances of tumour relapse, leading to poorer outcomes and quality of life for patients. Recent research indicates that extracellular matrix (ECM) composition and deposition modulate tumour behaviour and therapy response in SHH medulloblastoma. Ascorbic acid (AA), also known as vitamin C is an important co-factor in collagen production and has concentration dependant dual functionality as an antioxidant or pro-oxidant that may affect tumour microenvironmental dynamics and chemotherapy response. This study endeavours to link AA, collagen deposition, and chemotherapy response in SHH medulloblastoma models. DAOY (*TP53* mutant) and ONS-76 (*TP53* wild-type) cell lines were used to create 3D spheroid models that closely replicated SHH tumour architecture. Spheroids were treated with AA at physiological (100μM) and supraphysiological (2.5mM) concentrations, both alone and in conjunction with the chemotherapeutic drug cisplatin. Immunofluorescence imaging revealed that high-dose AA (2.5mM) increased extracellular collagen deposition and ECM density, but lower doses (100μM) produced minimal structural alterations. Functional experiments combining AA and cisplatin treatment revealed that physiological AA concentrations had a cytoprotective impact, lowering cisplatin-induced cytotoxicity, whereas supraphysiological dosages dramatically increased spheroid disintegration, decreasing spheroid viability. Molecular investigations indicated that the transporters of AA and its oxidised form dehydroascorbic acid (DHA) namely, SLC23A2 (SVCT2) and SLC2A10 (GLUT10), have a modest differential expression between the two SHH cell lines. Inhibition of SVCT2 and GLUT transporters with sulfinpyrazone and cytochalasin B, respectively, reduced AA uptake and modified redox homeostasis. The findings from this study suggest that supraphysiological concentrations of AA functions as a pro-oxidant, increasing cytotoxic impact of chemotherapy, whereas physiological levels retain antioxidant and protective properties, and thus work in favour of the tumour. These findings open a promising avenue for improvement in medulloblastoma therapy, in turn improving patient outcomes. Overall, this study demonstrates that pharmacological AA could be an effective adjuvant in SHH medulloblastoma treatment, given that concentration, transporter expression, and tumour subtype are carefully assessed throughout clinical translation.

ACKNOWLEDGEMENTS

A heartfelt thank you to my family, without their support I wouldn’t be where I am today.

I am deeply grateful to my supervisors Prof Ian Kerr and Prof Beth Coyle for giving me an opportunity to work on such a compelling project.

A warm and heartfelt thanks to Deb Briggs for everything she has done for myself, my project and the lab group.

I extend my appreciation to my peers and colleagues’ part of the research group.

Table of Contents

COMMON ABBREVIATIONS

AA ascorbic acid

DHA dehydroascorbic acid

SHH sonic hedgehog (signalling pathway)

WNT wingless (signalling pathway)

ROS reactive oxygen species

H_2O_2 hydrogen peroxide

OH^- hydroxyl radical

SVCT sodium dependent vitamin C transporter

GLUT10 glucose transporter 10

ECM extracellular matrix

IF immunofluorescence

COL1 collagen type I

LAM laminin

WHO world health organisation

TME tumour microenvironment

ASC^- ascorbyl radical

Chapter 1: Introduction

1.1 Features of Medulloblastoma

Medulloblastoma (MB) is the most prevalent malignant brain tumour in children and rarely detected in adults. It is an embryonal tumours of the central nervous system (CNS) (Pickles et al., 2018) and is responsible for 20% of all paediatric tumours found within the CNS (Kaatsch et al., 2001). Despite only accounting for 4-5% of childhood cancers, MB represents 10% of all cancer-related deaths in paediatrics (Pizer and Clifford, 2009). MBs arise and primarily locate within the cerebellum (Raffel, 2004) (Fig 1.1).

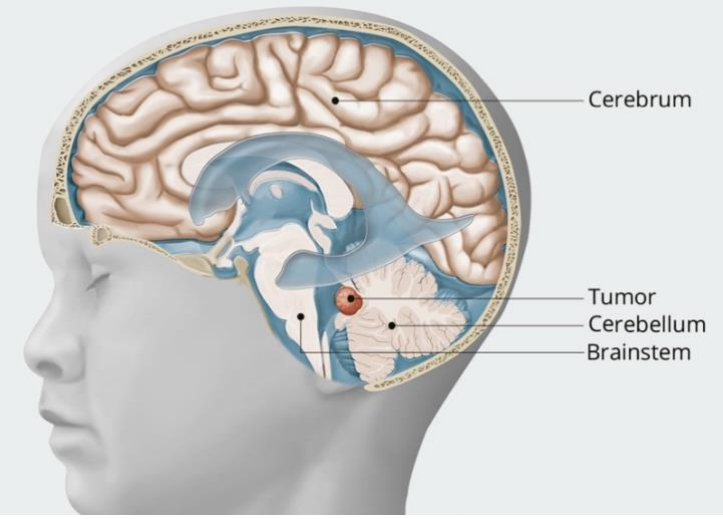

Figure 1.1 Localisation of medulloblastoma within the brain. MBs are found in the cerebellum which is the infratentorial region of the brain. They arise in the cerebellar vermis and protrude into the fourth ventricle, often taking over it completely. (Image obtained from (neurochirurgie.insel.ch).

1.1.1 Epidemiology and Clinical Characteristics

Smoll and Drummond (2012) examined the surveillance, epidemiology and end results (SEER) database ranging from 1973 to 2007 and found that comparing incidence of medulloblastomas in children with adults, there was 10-fold difference seen, in turn suggesting children to be more at risk. The annual incidence was estimated to be 6.0 per million children, which is around 450 new paediatric cases per annum. It was extrapolated that the largest prevalence at 44% was found in children aged 4 to 9, followed by ages 10 to 16 years at 23% and 0 to 3 years at 12% (Kool et al., 2012). Furthermore, the peak of incidence is found to be at age 7, where a higher incidence is seen in boys than girls (Gurney and Kadan-Lottick, 2001) with the male-to-female gender ratio being at 1.5:1 (Ciucci et al., 2014).

Since the posterior fossa is responsible for controlling balance, posture and complex motor functions, patients often manifest symptoms of irritability, tiredness, nausea and vomiting, morning headaches, anorexia, and behavioural abnormalities (Millard and De Braganca, 2016). Spreading of medulloblastoma to the spine influences symptoms of spinal pain, abnormal bowel and bladder functions and weakness/numbness within the limbs (National Cancer Institute, 2024).

1.1.2 Diagnosis and Metastasis

Medulloblastoma is one of the posterior fossa tumours that are differentially diagnosed by radiology. Initially a neurological examination is performed on the patient and followed by first line neuroimaging using computed tomography (CT) (Poussaint et al., 2015). Magnetic resonance imaging (MRI) is a more frequent and required diagnostic approach and has started to replace the use of CT scans (Dangouloff-Ros et al., 2021). MRI scans are used for follow-up monitoring of the tumour as well as pre- and post-surgery monitoring. The high cellular density feature of MB tumours results in hyperintense (white) on T2-weighted MRI and hypointense (grey/black) on T1-weighted MRI (Massimino et al., 2016).

Medulloblastoma tumours extend laterally, with the spinal cord being the most common metastases (Bühring et al., 2002). Up to 40% of individuals have spinal metastases, which are most frequently observed in the thoracic and lumbosacral regions, making it vital to perform spinal MRI before initiating treatment (Massimino et al., 2016). At the time of diagnosis, about 20–25% of patients had spread to other parts of the nervous system, including the spinal leptomeninges.

1.1.3 Treatment and Prognosis

Radiotherapy and chemotherapy are the common therapy approaches for all paediatric MB patients with acute and/or chronic sequelae (Padovani et al., 2019). A child's age, risk assessment, and the tumour’s molecular subgroup all influence the multidisciplinary treatment of medulloblastoma. About 70% of infants (children under the age of three but more recently under the age of six) diagnosed are cured with multimodal treatment methods that involve adjuvant platinum- and alkylator-based chemotherapy, maximal surgical resection, and craniospinal irradiation (CSI) (Gajjar et al., 2006b, Leary et al., 2021). Traditionally, children older than three years will undergo chemotherapy following surgery, followed by CSI with a boost to the tumour location (sometimes with concurrent chemotherapy). Infants frequently receive intensive chemotherapy with stem cell rescue or intrathecal therapy instead of immediate post-operative radiation therapy (Jackson and Packer, 2023).

Surgery/resection is another management method of medulloblastoma involving surgical removal of tumour. Children that get the safest maximal resection; the successful removal of brain tumour without disrupting neurological functions have been demonstrated to have better outcomes. Decompression of hydrocephalus; a buildup of cerebrospinal fluid (CSF) within the brain, is frequently possible with extensive resection, negating the necessity for long-term ventriculoperitoneal shunting (attaching a tube to drain excess CSF) (Zeltzer et al., 1999). Additionally, 10-40% of patients, following a surgical removal of medulloblastoma can be at the risk of developing posterior fossa syndrome (PFS). Due to the prevalence of language impairment, PFS is often referred to as cerebellar mutism syndrome. Other related symptoms, such as ataxia/hypotonia, supranuclear cranial nerve palsies, and emotional instability, can also occur (Khan et al., 2021).

Around one-third of patients experience an incurable tumour and the regimen of therapies have long-term negative impacts, where tumour is found metastatic at diagnosis or is sized >1.5cm^2 post-surgery (Gilbertson, 2004). Overall,

medulloblastoma patients are known to have a poor prognosis, especially in patients less than 3 years of age (Duffner et al., 1986). In older children who have previously received multimodal therapy, relapse of medulloblastoma can be much more difficult to treat than the initial tumour with the survival rate being less than 10% after a repeat of treatments (surgery, radiotherapy or high-dose chemotherapy) (Juraschka and Taylor, 2019). Patients with high-risk disease continue to have worse outcomes (60–70% 5-year event-free survival and overall survival), which is why more research is being done on treatment intensification techniques. This also shadows the importance of the development of new, biologically guided treatments for MBs (Gajjar et al., 2021, von Bueren et al., 2016).

New, focused therapy approaches that aim to lower toxicity and increase survival rates have been developed as a result of recent molecular discoveries about the pathophysiology of medulloblastoma. These days, molecularly based strategies concentrate on blocking signalling pathways that are unique to particular subgroups. For example, MYC and CDK (cyclin-dependent kinases) inhibitors are being investigated for Group 3 cancers, which are frequently linked to MYC amplification and a poor prognosis, whereas SMO and GLI inhibitors are being investigated for SHH-driven malignancies (Lazow et al., 2022).

Furthermore, epigenetic modifiers like histone deacetylase (HDAC) inhibitors show promise in reprogramming transcriptional dysregulation in aggressive subgroups (Jaeger et al., 2020, Zwergel et al., 2018), and immunotherapy-based interventions like immune checkpoint inhibitors, vaccine strategies, and CAR-T cell therapies are being researched to counteract tumour immune evasion (Poggi et al., 2025). Even though many of these approaches are still in the early stages of clinical or preclinical development, they mark a substantial move towards precision medicine in the treatment of medulloblastoma, where the molecular and genetic profile of the tumour is increasingly used to guide treatment rather than a standard therapeutic approach (Lazow et al., 2022).

1.1.4 Classifications of Medulloblastoma

Classifying medulloblastoma depends on histopathology; often carried out by a neuropathologist, and the molecular biology involved in the tumour development. There are different clinical risks associated to the histological and molecular heterogeneity present in this tumour (Orr, 2020). Older WHO classification system of CNS tumours divided medulloblastoma into two distinct generic designations: histologically determined (classic, large cell/anaplastic (LC/A), desmoplastic/nodular (D/N) and medulloblastoma with extensive nodularity (MBEN) medulloblastomas) and molecularly determined medulloblastomas. However, in the more recent WHO classification shines importance on the molecular subgroups of medulloblastoma and their corresponding subtypes (**figure 1.2.**) (Louis et al., 2021).

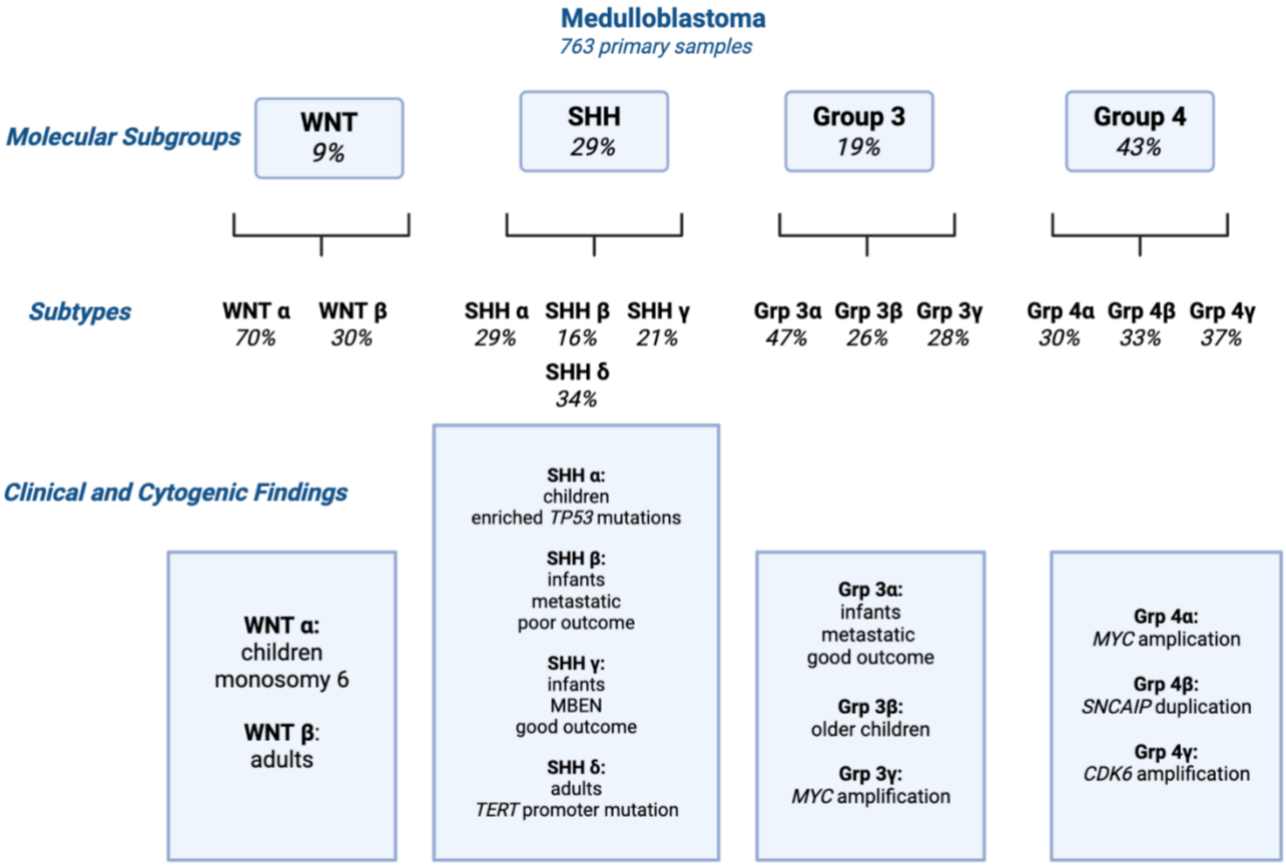

Figure 1.2 Molecular subgroups and subtypes of medulloblastoma. Four subgroups (WNT, SHH, Group 3 and Group 4) of medulloblastomas and their corresponding 12 subtypes with the related clinical/cytogenic information per subtype. Figure adapted from Cavalli et al. (2017).

1.1.4.1 Molecular Subtypes

Molecular subgroups of medulloblastomas defined by transcriptomic profiling are Wingless (WNT), Sonic Hedgehog (SHH), Group 3 and Group 4 (Louis et al., 2016). Due to inherent intra-subgroup heterogeneity, there are 12 subtypes characterised within the four molecular subgroups (**figure 1.2.**). WNT and SHH medulloblastomas are distinctly recognisable and separate in most transcriptional and methylation profiling investigations, exhibiting low overlap with other subgroups (Taylor et al., 2012). On the other hand, new integrative multi-omics and developmental research has shown that neither Group 3 and Group 4 tumours have a key molecular driver and has a significant overlap these subgroups (Hendrikse et al., 2022, Smith et al., 2022).

1.1.4.1.1 Wingless (WNT)

The WNT subgroup is characterised by the aberrant activation of the WNT signalling pathway (**figure 1.3.**) leading to the development of tumour. This occurs due to mutations in genes part of the WNT signalling pathway e.g. *APC* and *CTNNB1* (encodes b-catenin) genes. Upon the activation of WNT signalling, b-catenin levels are upregulated and is translocated to the nucleus where it acts as a transcription activator, leading to cell cycle progression and differentiation (Ellison et al., 2005).

Therefore, common features for characterising WNT-activated medulloblastomas are CTNNB1 stabilisation and nuclear localisation of β-catenin (Skowron et al., 2015).

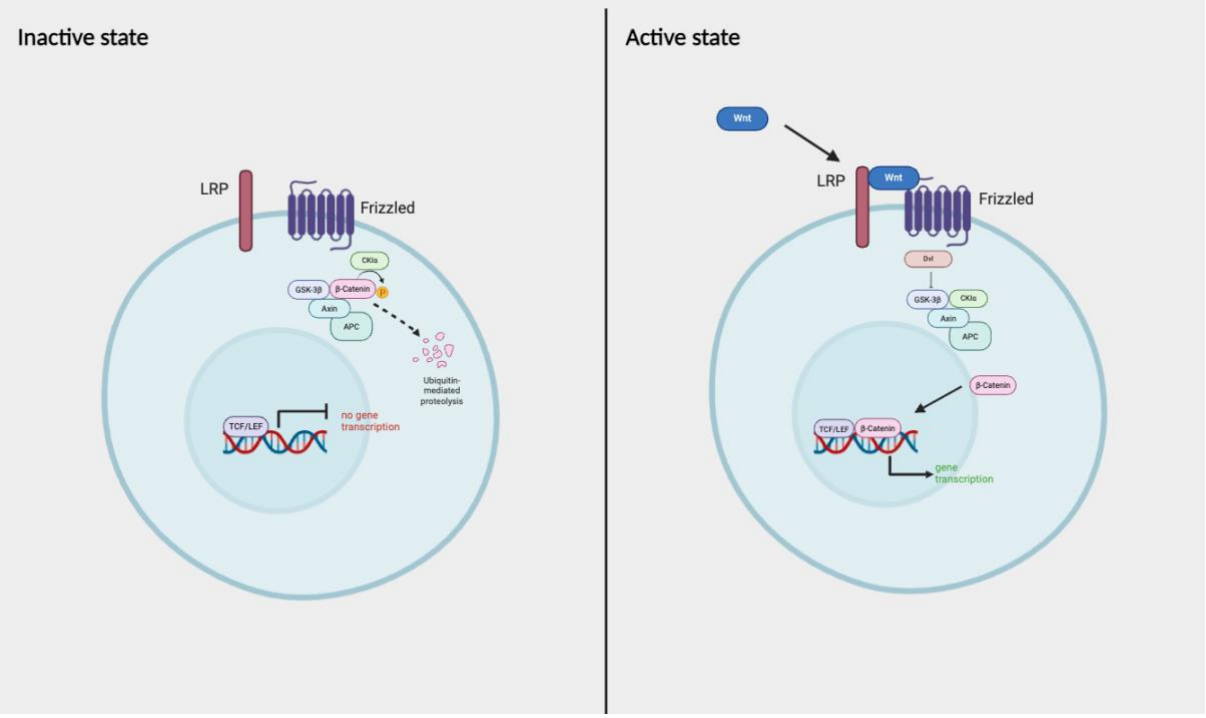

Figure 1.3 Overview of the WNT signalling pathway. The WNT signalling pathway in the absence of WNT protein is in an inactive state and protein complexes such as AXIN, APC, serine/threonine kinase GSK-3, CK1, and E3 ubiquitin ligase β-trcp break down β-catenin (via ubiquitin-mediated proteolysis). In the presence of WNT proteins (active state), binding to its receptors LRP and Frizzed, with the help of dishevelled protein (Dvl), the WNT signal transduces downstream from cell membrane by inhibiting the ubiquitous breakdown of β-catenin. β-catenin is then translocated into the nucleus where it interacts with TCF/LEF (T cell factor/lymphocyte enhancer factor 1) and activates transcription of target genes involved in cell proliferation, differentiation, survival and migration. Abnormal activation of the WNT signalling pathway can give rise to tumours, as seen in medulloblastoma (Cruciat and Niehrs, 2013, Liu et al., 2022).

WNT-activated medulloblastoma is the most well-known subgroups and often results in a positive long-term prognosis compared to other subgroups (Gajjar et al., 2006a) with 95% of patients with WNT medulloblastoma surviving (Ellison et al., 2005). WNT tumours account for 10% of all medulloblastoma tumours and patients with WNT subgroup tumours have a favourable prognosis (Kool et al., 2012). WNT medulloblastomas are not readily metastatic and display an even gender distribution ratio (Kool et al., 2012). Research done on mouse models by Gibson et al. (2010) suggest that WNT medulloblastomas originate from the progenitors of the lower rhombic lip of the cerebellum and in humans, WNT-activated tumours are found adjacently to the brainstem.

1.1.4.1.2 Sonic Hedgehog (SHH)

The SHH subgroup of medulloblastomas has its name derived from the Sonic Hedgehog signalling pathway (**figure 1.4.**). SHH is a secreted protein that belongs to the hedgehog family of proteins and has been well-preserved throughout evolution. It is essential for the development of the CNS as it plays a role in sending signals that induce cell differentiation (Ingham and McMahon, 2001). Tumours in this subgroup are initiated by the abnormal activation of their SHH signalling pathway which overloads the expression of *GLI2* (GLI family zinc finger 2) transcription factor target resulting in uncontrollable granule cell proliferation (Hatten and Roussel, 2011). Sonic Hedgehog medulloblastoma transcriptionally mimics the granule cell precursor (GCP) lineage, aligning with other studies indicating that SHH medulloblastomas originate from GCPs in the exterior granular layer (Wechsler-Reya and Scott, 1999).

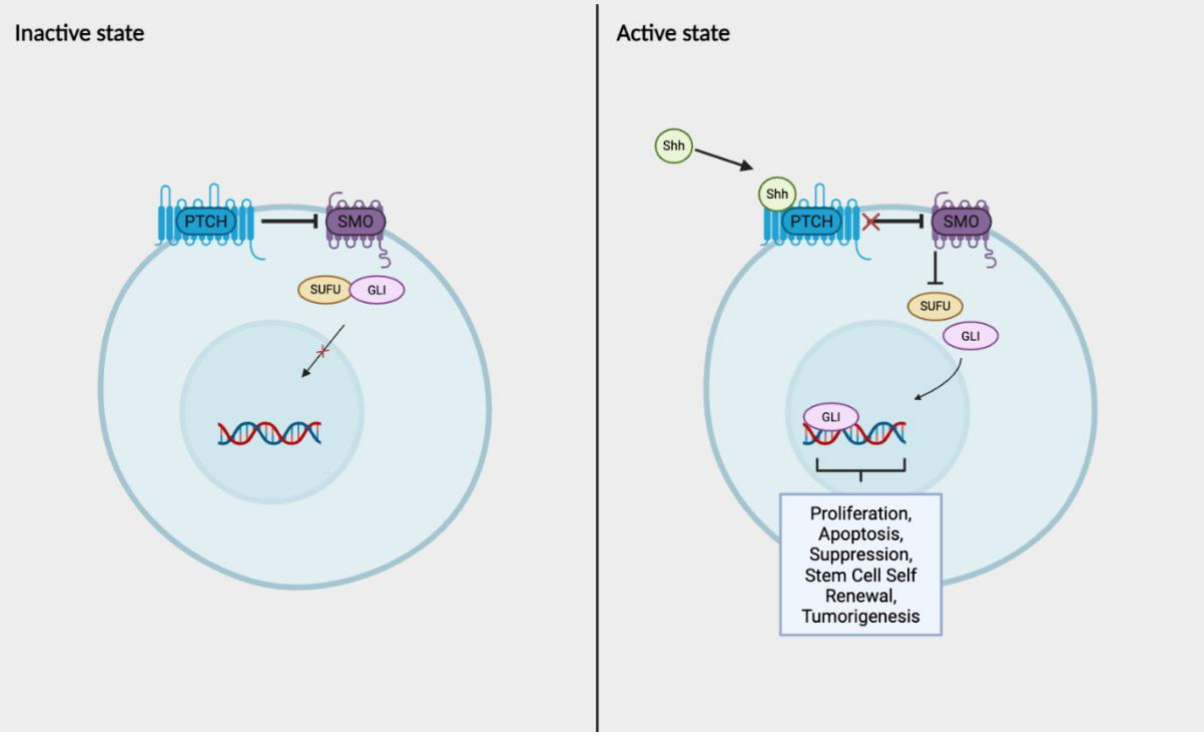

Figure 1.4 Overview of the SHH signalling pathway. SHH pathway in inactive state (absence of SHH) and active state (presence of SHH). SHH is a secreted morphogen, which controls the development of many organs including the central nervous system. In the active state, smoothened (SMO) inhibition is relieved when SHH binds to its receptor Patched 1 (PTCH1), activating the pathway. The tumour suppressor protein SUFU is inhibited by activated SMO, which also promotes the conversion of GLI factors into transcriptional activators of growth-promoting, stemness and survival genes which drives cell proliferation, apoptosis, suppression, stem cell renewal and even tumorigenesis; when pathway is aberrantly activated, as seen in medulloblastomas. When the SHH morphogen is not present (inactive state), direct transcriptional repression or SUFU-mediated GLI repressor synthesis actively suppresses the transcription of SHH target genes (Jiang and Hui, 2008, Smit et al., 2022).

Unlike the WNT subgroup, patients with SHH medulloblastoma have an intermediate prognosis and a 5-year survival rate that lies between 60-80% (Cho et al., 2011). SHH-activated medulloblastomas account for 30% of all medulloblastomas and almost all these cases are in infants (0-3 years) and adult (>16 years) (Gajjar et al., 2014). Shh-MB consists of four molecular subtypes: SHH-α, SHH-β, SHH-γ and SHH-δ. SHH-α which is seen to affect children aged 3-16 years, has the worse prognosis. SHH-β and SHH-γ subtypes are seen in infant tumours (<3 years) where SHH-β subtyped tumour carries worse survival outcomes for these infants than SHH-γ. SHH-δ subtype accounts mainly for adult tumours and results in a favourable prognosis (Cavalli et al., 2017)

Individuals with germline mutations in SHH receptor PTCH1 (protein patched homolog 1) and *SUFU* (suppressor of fused homolog) are predisposed to medulloblastoma (Brugières et al., 2010, Taylor et al., 2000). Similarly, somatic mutations of PTCH1, *SUFU* and *SMO* (smoothened) and amplifications of *GLI1* and *GLI2* leads to sporadic generation of medulloblastomas (Northcott et al., 2011a, Northcott et al., 2009). Each SHH subtype has unique gene mutation patterns, with SHH-α and δ displaying a greater mutation burden compared to SHH-β and γ (Skowron et al., 2021). About 21% of SHH medulloblastomas are enriched with *TP53* mutations. These tumours can be categorised as either: "SHH-activated *TP53*-mutant" or “SHH-activated *TP53*-wild-type”. Two-thirds of mortality in children over five is caused by tumours with *TP53* mutations (Zhukova et al., 2013).

1.1.4.1.3 Group 3

Group 3 tumours commonly develop in infants (0-3 years) and children. This subgroup accounts around 25% of all medulloblastoma cases and tends to affect males twice as more than females. Group 3 tumours in infants readily display LC/A histology and have an overall metastasis rate of 30% for all age groups and for infants alone it is 47%; the highest frequency of tumour being metastatic at diagnosis (Kool et al., 2012). Group 3 are aggressive tumours with worst prognosis among the four medulloblastoma subgroups, with a 5-year overall survival just over 50% in comparison to 70% for the other subgroups (Thompson et al., 2016).

According to recent single-cell transcriptomic research, progenitor populations of the early upper rhombic lip (structure of the developing cerebellum) are the source of Group 3 and Group 4 medulloblastomas' shared developmental trajectory (Smith et al., 2022, Vladoiu et al., 2019). Transcriptional and developmental studies indicate that Group 3 tumours develop from undifferentiated progenitor cells from the early stages of rhombic lip and the transcriptional pathways of Group 3 tumours corresponds to early glutamatergic progenitors, seen before neuronal development (Gibson et al., 2010, Lin et al., 2016).

Group 3 tumours harbour *MYC* amplifications as a key distinguishable feature with an occurrence in 15-20% of Group 3 patients alongside whole-chromosome abnormalities and isochromosome 17q which are also prevalent in these tumours (Northcott et al., 2012). The *MYC* amplification seen in Group 3 tumours can cause fusions between the long non-coding RNA *PVT1* (Plasmacytoma Variant Translocation 1) and second exon of *MYC* (Patapoutian and Reichardt, 2000). Another common alteration seen in Group 3 patients is the amplification of *OTX2*

(orthodenticle homeobox 2) transcription factor which is observed in around 10% of Group 3 patients (Bai et al., 2012).

1.1.4.1.4 Group 4

With an intermediate 5-year overall survival of 75%, Group 4 is the most prevalent subgroup of medulloblastoma, accounting for more than 40% of medulloblastoma cases. As mentioned before, Group 4, like Group 3 tumours originate from the upper rhombic lip of the developing cerebellum. According to transcriptomic analyses, Group 4 tumours originate from progenitors of the upper rhombic lip which rise to unipolar brush cells (UBCs) within the developing cerebellum (Vladoiu et al., 2019).

Group 4 tumours carry higher isochromosome 17q compared to Group 3 and the loss of X chromosome is readily seen in female patients with Group 4 medulloblastomas (Northcott et al., 2011b). Furthermore, in around 17% of Group 4 patients, the overexpression of *PRDM6* (PR/SET domain 6), a tumour repressor, has been found to drive tumorigenesis of Group 4 medulloblastomas (Northcott et al., 2017).

1.2 Tumour Microenvironment (TME) in Medulloblastoma

The tumour microenvironment (TME) affects the efficacy of targeted therapies and is crucial in controlling the development, growth, and dissemination of tumours. Components that make up the TME are: blood and lymphatic vessels, the extracellular matrix (ECM), supporting stromal cells such as mesenchymal stromal cells, and pericytes, immune cells including tumour-associated macrophages (TAM), T and B lymphocytes, dendritic cells, neutrophils, and natural killer (NK) cells along with signalling molecules like cytokines, chemokines and growth factors (van Bree and Wilhelm, 2022).

The TME of brain cancers plays a dynamic and significant role in the development, spread, metastasis, and response to treatment. The presence of resident cells specific to the central nervous system (microglia, astrocytes, and neurones), the specialised vasculature of the blood-brain barrier (BBB), and a distinct extracellular matrix (ECM) composition, the microenvironment of brain tumours differs significantly from that of extracerebral cancers (Perus and Walsh, 2019, Quail and Joyce, 2017). Tumour cells, neural-progenitor-derived cells, astrocytes, microglia/myeloid cells, endothelial/pericyte units, and ECM components like laminin, vitronectin, and proteoglycan-modifying enzymes make up the TME in medulloblastoma tumours. These tumour cells communicate with one another through cytokines, growth factors (IGF-1, IL-4, IL-6, and CCL2), and developmental ligands (such as WNT and SHH proteins). Variation in the TME between the molecular subgroups of medulloblastomas may contribute to treatment resistance and recurrence of the tumour (van Bree and Wilhelm, 2022, Yang et al., 2024).

The immunosuppressive environment observed in medulloblastoma may be influenced by the immune-modulatory properties of collagens in the TME. Collagen's immune-modulatory qualities have been linked to a number of cancer types. In these cases, high-density collagen inhibits T-cell migration, infiltration and activity, and drives macrophage polarisation towards a TAM immunosuppressive phenotype

(Dustin and de Fougerolles, 2001, Larsen et al., 2020, van Bree and Wilhelm, 2022). Furthermore, the increased or decreased deposition of collagen in tumours can be linked to increased malignancy (Arnold et al., 2010, Levental et al., 2009).

1.2.1 Extracellular Matrix (ECM) in Medulloblastoma

The normal ECM environment of the brain is made up of glycoproteins, proteoglycans like chondroitin sulphate and heparan sulphate, glycosaminoglycans, and growth factors. Proteins like collagen and fibronectin are also present. During tumour development within the brain, ECM integrity is lost as a result of force-mediated physical remodelling, post-translational changes, proteolytic degradation, and abnormal ECM deposition (Lam et al., 2019). The dysregulated remodelling of the ECM in cancers causes a variety of biophysical and biochemical alterations that impact cell signalling, ECM stiffness, cell migration, and tumour growth (Egeblad et al., 2010). There are four mechanisms of ECM remodelling: 1) ECM deposition, 2) post-translational modification, 3) degradation of the ECM and 4) force-mediated modification of the ECM (Winkler et al., 2020).

Trombetta-Lima et al. (2021) compared the proteome profiles of medulloblastoma and glioblastoma with cerebellum and neocortex. Both tumour types showed unique ECM signatures. The medulloblastoma displayed an ECM profile that was rich in collagens (COL1A1, COL5A2, and COL6A3), proteoglycans (lumican) and glycoproteins. Upregulation of the genes encoding for these fibrous proteins was seen in the SHH and WNT subgroups.

1.2.2 Collagen in Medulloblastoma ECM

Collagen is composed of three polypeptide α-chains, which exhibit a polyproline-II shape, a right-handed supercoil, and a one-residue stagger between neighbouring chains. The key amino acids that make up the structure of collagen are glycine, proline and hydroxyproline (**figure 1.5.**) (Brodsky and Persikov, 2005). 28 distinct varieties of collagen have been identified in vertebrates, from which type I collagen is the most common due to its vital role it plays in tissues. In the ECM of many connective tissues, type I collagen is the most abundant fibrillar collagen. It forms long, triple-helical fibrils that are resistant to shear and tensile pressures, giving these tissues vital mechanical strength and structural integrity (Gelse et al., 2003). Prior to the formation of collagen in a triple helical structure, collagen goes through several post-translational changes via hydroxylation and cross-linking reactions in the endoplasmic reticulum (Boot-Handford and Tuckwell, 2003, Shoulders and Raines, 2009).

The synthesis and regulation of collagen is known to be intricate, with the involvement of various intracellular and extracellular processes along with many molecular modifications and enzymatic reactions specifically tailored for collagen. Ascorbic acid (AA) is a well-known co-factor involved in the biosynthetic process of collagen, where it's primary role as a to co-factor in the enzymatic hydroxylation of proline to form hydroxylysine in the procollagen precursor to form stable collagen (**figure 1.6.**) (Pinnell, 1982).

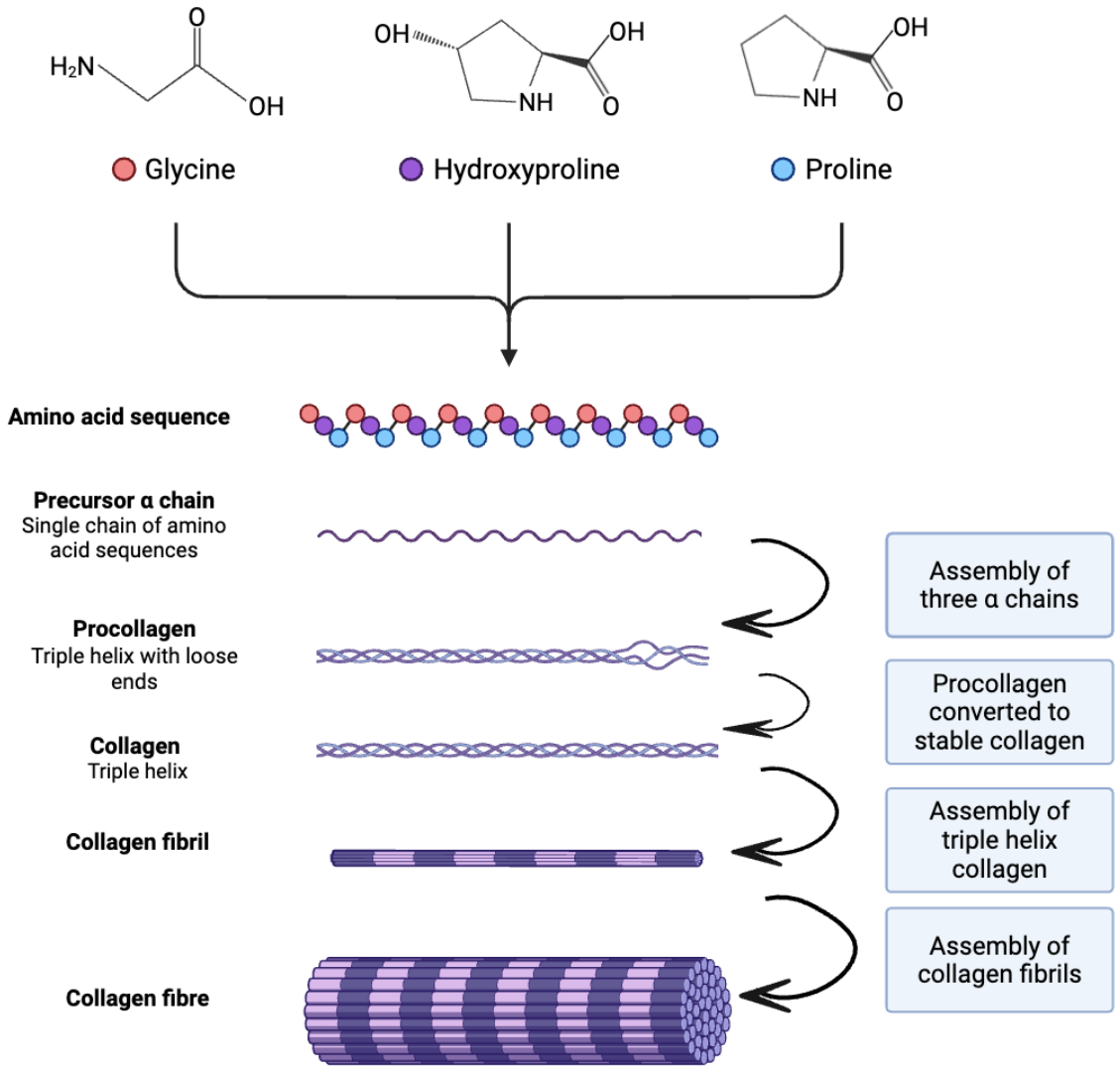

Figure 1.5 Structural composition of collagen. Adapted from (Sobczak-Kupiec et al., 2021)

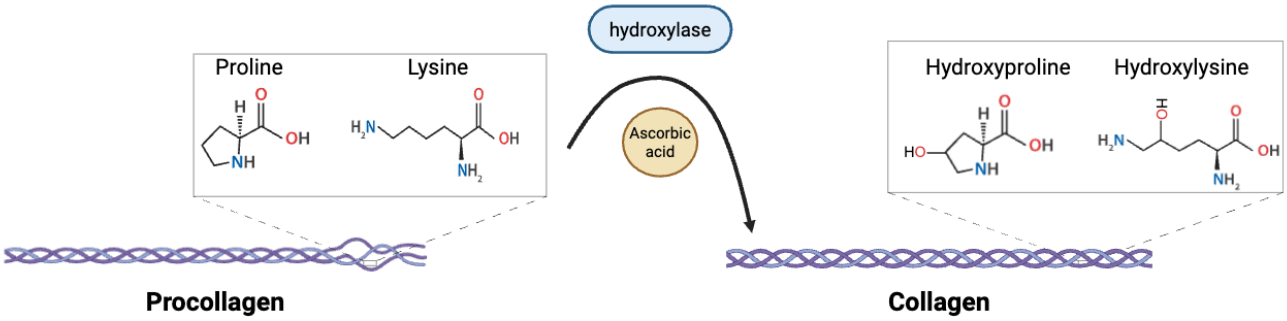

Figure 1.6 Hydroxylation of proline and lysine residues with AA as co-factor. Proline and lysine residues on procollagen make it unstable. To form a stable collagen triple helix, the proline and lysine residues found on procollagen chains are hydroxylated by prolyl hydroxylase and lysyl hydroxylase. Ascorbic acid acts as a co-factor to the hydroxylase enzymes in this reaction. In this intermediate step of

collagen synthesis, ascorbic acid is vital in stabilising procollagen before collagen fibrils can be formed (Pinnell, 1985).

In human ovarian tumours, it was demonstrated that increased type I collagen biosynthesis is correlated with tumour aggressiveness linking ECM remodelling and deposition with tumour invasion and cancer (Zhu et al., 1995). This increase in deposition in turn disrupts processes like cell polarity, cell-cell adhesion and can increase cell signalling which as a result facilitates tumour growth. ECM remodelling significantly impacts gene expressions, migration, proliferation, differentiation and treatment response and overall cell biology of the tumour (Paszek and Weaver, 2004). Another example of this is seen in breast cancers, where collagen in the tissue gradually thickens, linearises, and stiffens in tandem with tumour development, as a result, encouraging cell migration into the ECM and giving rise to metastasis (Wyckoff et al., 2007).

Medulloblastomas also show overexpression of type I collagen compared to normal cerebellum (Ramaswamy et al., 2001). The best characterised receptors for type I collagen are integrin membrane proteins. One α chain and one β chain make up the heterodimeric glycoproteins, integrins. The β1 subunit (ITGB1) is shared by all type I collagen-binding integrins (White et al., 2004). Immunohistochemical data from Liang et al. (2008) not only displays strong collagen deposition in medulloblastoma tumours but suggests that collagen interacting with integrins may activate signalling pathways that enhance tumours ability to adhere, invade and survive.

Moreover, gene expression of type I and type VI collagens is significantly high in the SHH subgroup of medulloblastomas in comparison to Group 3 and with immunohistochemical staining, these collagens form a dense outer shell structure which distinctly characterise SHH tumours (**figure 1.7**.; (Linke et al., 2023)). Subsequently, analysis carried out by Linke et al. (2023) of the large genomic dataset from Cavalli et al. (2017) found *COL1A1* and *COL6A1* to correlate with better survival outcomes for patients with SHH medulloblastoma, proposing that the collagen dense ECM shell structure results in a favourable prognosis for patients in the SHH subgroup.

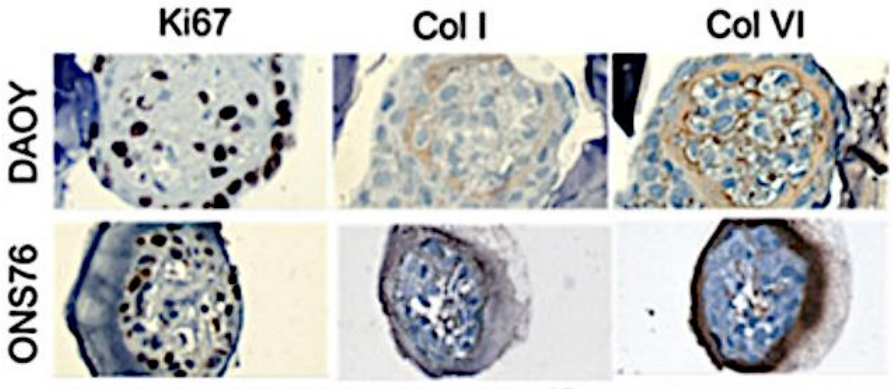

Figure 1.7 SHH spheroid models showing dense collagen "shell-like" structure. Immunohistochemical staining on SHH spheroid models by Linke et al. (2023) revealed thick shell structures of Col I and Col VI. Image adapted from (Linke et al., 2023).

1.3 Ascorbic Acid (AA)

Ascorbic acid colloquially known as Vitamin C is a water-soluble molecule that is a reducing agent and donor antioxidant (Du et al., 2012a). Humans do not sustain the ability to synthesise AA making them dependent on supplement and food sources to meet the sufficient requirement of AA. Furthermore, the uptake of AA in the intestinal tract is strictly regulated (Graumlich et al., 1997). AA is vital for collagen synthesis as deficiency of AA/Vitamin C gives rise to scurvy (Njus et al., 2020). Ascorbyl radical (Asc^-) and dehydroascorbic acid (DHA), respectively, are products of AA, when it goes through one-electron oxidations, twice consecutively (**figure 1.8.**). The rate of oxidation for AA is heavily dependent on pH and the presence of catalytic metals (Buettner and Jurkiewicz, 1996). AA in the absence of catalytic metals can undergo pH-dependant autoxidation, which leads to the production of hydrogen peroxide (H_2O_2) (Calcutt, 1951).

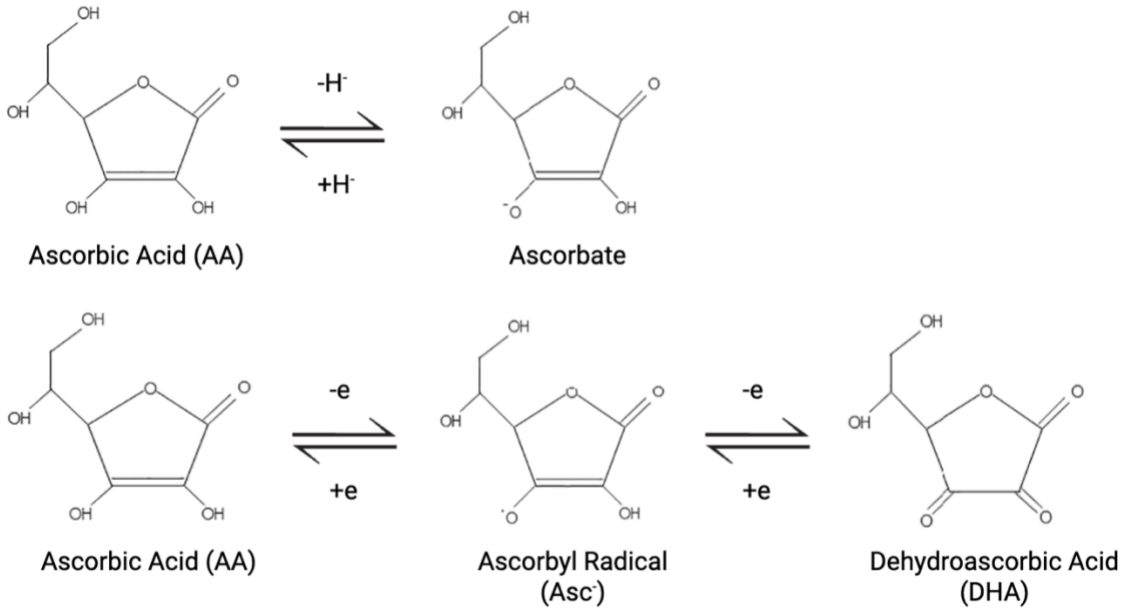

Figure 1.8. Ascorbic acid deprotonation and oxidation. Ascorbate anion is formed when AA loses a proton. When ascorbic acid loses an electron (oxidised) it forms an ascorbyl radical (Asc^-). DHA is formed when the intermediate Asc^- is oxidised. Adapted from (Pozzer et al., 2021).

Humans can source AA and DHA which are absorbed within the small intestine. AA is taken up by sodium dependent vitamin C transporters (SVCTs) whereas the oxidised form DHA is taken up by sodium independent glucose transporters (GLUTs). Upon uptake, DHA is readily reduced back to AA (Welch et al., 1995). The primary function of GLUTs is to transport glucose, however due to glucose molecules and DHA molecule sharing structural resemblances DHA can also be transported.

1.3.1 Antioxidant and Pro-oxidant Properties of AA

AA is fundamentally the most common low molecular weight antioxidant human cells use. It contributes to controlling levels of reactive oxygen species (ROS) and simultaneously enhance the potency of other antioxidants. ROS species are generated during cellular metabolism and cellular stress. Primary sources of ROS

are the mitochondrial respiratory chain and enzymes like xanthine oxidases (XO) and NADPH oxidases (NOXs) (Sies and Jones, 2020). AA neutralises ROS and damaging free radicals by readily donating an electron, and in turn becomes an ascorbyl radical (**figure 1.8.**). Ascorbyl radicals are non-damaging, unreactive and can easily be reduced back to AA by reductases dependant on NADH/NADPH (Linster and Van Schaftingen, 2007). Additionally, ascorbyl radicals can form AA and DHA by undergoing pH-dependant disproportionation reactions (Bielski et al., 1981).

An opposing property of AA is that it can act as a pro-oxidant, meaning AA can promote oxidative stress. This can occur when AA encounters catalytic metal ions (Buettner and Jurkiewicz, 1996). When AA is being oxidised to ascorbyl radical, it can also act as reducing agent, where it can reduce ferric iron (Fe3+) to ferrous iron (Fe2+) and cooper ions (Cu2+) to cooper atoms (Cu). Generated Fe2+ can reduce O_2 to a superoxide radical which dismutates to give H_2O_2 and O_2 (Du et al., 2012a). Subsequently, the Fenton reaction sees Fe2+ react with H_2O_2 to form Fe3+. This reaction also generates an oxidising hydroxyl radical, and thus, with the presence of AA, the recycling of Fe2+ to Fe3+ is highly mediated. As a result, releasing ROS species from H_2O_2 (Du et al., 2012a). The Haber-Weiss reaction is an iron catalysed reaction that involves the generation of highly reactive hydroxyl radicals, when a superoxide reacts with H_2O_2 (Kehrer, 2000).

1.3.2 Transport of AA and DHA

As briefly mentioned before, AA and DHA are transported by two families of transporters, SVCTs and GLUTs, respectively. All animal cells rely on the availability of functional AA transporters, which control the distribution of this molecule between extracellular and intracellular fluids (and between subcellular organelles) regardless of their capacity for biosynthesis. SVCTs and GLUTs allows both the reduced (AA) and oxidised (DHA) forms of AA, respectively, to pass across the plasma membrane (Savini et al., 2008).

Two key SVCT proteins for AA uptake are SVCT1 and SVCT2 (Tsukaguchi et al., 1999). These are plasma membrane glycoproteins, encoded by *SLC23A1* (SVCT1) and *SLC23A2* (SVCT2) genes. They are dependent on the sodium ion electrochemical gradient across the plasma membrane to facilitate the uptake of AA against a concentration gradient (Wilson, 2005). They exhibit distinct mechanistic features and tissue distribution, pointing to various physiological purposes. While SVCT2 shields metabolically active cells from oxidative stress, SVCT1 contributes to the equilibrium of AA throughout the body. SVCT1 has lower affinity for AA and thus AA concentrations in plasma are tightly regulated (Padayatty et al., 2004).

Human SVCT1 transporters are predominantly found in the brush-border surfaces of the intestines for intestinal AA absorption and in kidneys for renal re-absorption of AA (Savini et al., 2008). In contrast, SVCT2 has a higher affinity for AA and is found in osteoblasts and various tissues like, neural, neuroendocrine, exocrine and endothelial where high oxidative stress occurs (Wilson, 2005). AA may preferentially accumulate at locations where it is required due to regulation of SVCT2 at the mRNA or protein level (Savini et al., 2008). Within the family of SVCTs, there are also two orphan transporters SVCT3 and SVCT4, that have no known substrates, leaving

SVCT1 and SVCT2 being the only functional proteins within this family (Takanaga et al., 2004).

GLUTs are mammalian glucose transporters that primarily transport glucose, but some of which can also transport DHA, the oxidised version of AA. DHA makes up less than 2% of the AA found in plasma and cells under normal circumstances (Hosoya et al., 2004).

GLUTs are encoded by the *SLC2* gene family, of which there are 14 of them. These are further subdivided phylogenetically into classes I, II and III (Joost et al., 2002). Initially, it was proposed for GLUTs to catalyse the transport of glucose, however this was found to be the case for only class I GLUTs and was later discovered that class II and III GLUTs do not primarily function to transport glucose. Selected GLUTs, specifically from class III, can have different substrates, depending on their cellular localisation and physiological conditions (Holman, 2020).

1.3.3 Role of AA in Cancer Treatments

A study conducted on 500 patients with heterogenous terminal cancers and giving the supplementation of high dose AA resulted in patients reporting subjective improvements such as a greater sense of wellbeing, more energy, enhanced alertness, decreased or eliminated discomfort, and improved appetite (Cameron and Pauling, 1976). However, overtime the use of high dose AA as a potential cancer treatment was disregarded due to many clinical trials failing to show beneficial results (Creagan et al., 1979, Moertel et al., 1985). With further investigations, it was revealed that the steady-state plasma concentrations of AA at 200 mg oral dosages are approximately 80μM. At this dose, the fraction of bioavailable AA declines, urine excretion rises, and relative absorption falls as dosages surpass 200mg. Even with a maximal oral dosage of 3g six times a day, peak plasma concentrations did not surpass ≈220μM (Graumlich et al., 1997, Padayatty et al., 2004). In contrast, investigations carried out using high dose AA intravenously, showed giving patients 10g of AA can result in a plasma concentration of 1-5mM (Drisko et al., 2003).

Glioblastoma, ovarian and pancreatic carcinomas compared to healthy cells, have greater susceptibility to cytotoxicity induced by AA (Chen et al., 2008). A similar study demonstrated that pancreatic cancer cells are more susceptible to higher levels of AA than normal cells and suggested that this was due to the existence of high ROS and low antioxidant enzyme levels in cancer cells (Liu et al., 2004). Less effective H_2O_2 elimination and heightened susceptibility to AA-induced cytotoxicity may result from the comparatively reduced activity of catalase, glutathione peroxidase, and peroxiredoxins found in cancer cells (Du et al., 2012a). The pro-oxidant effects of AA can be triggered in presence of Fe3+ and Cu2+. Cancer treatments like ionising radiation and certain chemotherapeutic drugs increase the presence of catalytic free iron, thus chemicals that raise catalytic iron levels may increase the cytotoxicity of AA at pharmacological levels (Carmine et al., 1995).

AA plays an important part in the treatment of cancer. Because of its antioxidative qualities, it gives patients relieve from radiation and chemotherapy side effects such as nausea and fatigue (Abiri and Vafa, 2021). Compared to utilising AA or chemotherapy alone, research indicates that high-dose AA combined with certain

anticancer drugs can more effectively reduce viability of cancer cells (Lee et al., 2019).

1.4 Hypothesis and Aims

Collagen is the main structural component of extracellular matrix (ECM) and plays a vital role in tumour growth and progression. Collagen biosynthesis depends on ascorbic acid (AA) supply, as seen in scurvy; a condition where a deficiency in vitamin C perturbs the production of collagen. In addition to its structural function, AA has pro-oxidant and antioxidant qualities, and its effectiveness is being researched in the treatment of cancer. However, its function in medulloblastoma is yet unclear. Prior research has demonstrated improved survival rates for patients with SHH-subgroup medulloblastomas that express high levels of collagen and portray a dense ECM shell-like structure. Expanding on this knowledge, we hypothesised that treatment with high-dose of AA may increase favourable survival outcomes for patients with SHH-medulloblastoma by increasing collagen deposition within the ECM. Furthermore, we hypothesised that co-treatment of high-dose AA with a chemotherapeutic agent can enhance the cytotoxicity properties of chemotherapy in SHH tumours. The aims of this thesis were to investigate:

I. Whether AA at higher concentrations contributes to an increase ECM deposition in SHH tumours
II. To validate the expression of AA and DHA transporters in SHH medulloblastoma tumour models
III. Whether the pro-oxidant effects of AA at higher concentrations enhances chemotherapy response in SHH tumours

Chapter 2: Materials and Methods

2.1 Cell Culture

Two cell lines that are SHH-patient derived were used in this study: DAOY and ONS-76. Both cell lines were cultured in their respective cell culture medium (**table 2.1.)** and grown in standard treated T-25 flasks. Cells were incubated at 37℃ with 5% CO_2 and humidified atmosphere. Both cell lines were cultured to generate 3D spheroid models, prepare pellets or subculturing cells when at 70-80% confluency.

Table 2.1. Details of the cell lines used in the study (Jacobsen et al., 1985, Yamada et al., 1989)

Cell Line	Sub-type TP53 status	Media	Source
DAOY	SHH-a TP53 mutant	Dulbecco's modified Eagle's medium (DMEM) + 10% foetal bovine serum (FBS)	Originates from tumour biopsy of desmoplastic cerebellar medulloblastoma in the posterior fossa of a 4-year-old white boy Cell line established by P.F. Jacobsen at the Royal Perth Hospital in Western Australia in 1985 (Wybranska et al., 2013)
ONS-76	SHH-b TP53 wild type	Roswell Park Memorial Institute-1640 (RPMI-1640) + 10% FBS	Originates from primary cerebellar medulloblastoma tumour specimen from a 2-year-old Japanese girl. Cell line was established in 1987 (Sun et al., 2012).

2.1.1 Thawing Frozen Stock of Cells

Cells were stored in cryogenic vials in liquid nitrogen for long term storage. To culture cells from frozen stock, cells were thawed at 37℃. Treated T-25 flasks were prepared by adding 4mL of pre-warmed culture media and contents of vials were gently pipetted into the flasks. Cells were incubated overnight at 37℃ with 5% CO_2 and humidified atmosphere. A media change was performed 24 h later to ensure efficient recovery of cells. Cells were grown until 70-80% confluency was reached.

2.1.2 Cell Growth and Maintenance

Cells were harvested when confluency in flasks reached around 70-80%. Both cell lines are adherent thus cells were passaged by aspirating medium from flasks and washing cells with phosphate buffer solution (PBS). 1mL of 1x Trypsin-ethylenediaminetetraacetic acid (EDTA) was used to detach cells from surface of a

T25 flask. Cells were incubated in Trypsin-EDTA for 5 min at 37℃. Trypsin-EDTA was inactivated by adding 4mL of respective culture medium to flasks. 5mL of these cell suspensions were centrifuged at 800 x *g* for 5 min to get cell pellets. After discarding supernatant, cell pellets were resuspended in their culture media and split in a 1:10 ratio. Cell suspension was seeded in new treated T25 flasks with pre-warmed culture media. Flasks were incubated at 37℃ with 5% CO_2 and humidified atmosphere. Medium change would be done 2 days after cells were seeded. Cells would reach 70-80% confluency around day 4 after seeding.

2.1.3 Preparation of Cell Pellets

Cell pellets were prepared for DNA and RNA isolation. Upon seeding cells into a T-25 flask at a ratio of 1:10, the remaining cell suspension was centrifuged at 800 x *g* for 5 min to generate a cell pellet. Cell pellets were resuspended with 1mL of PBS and transferred into an Eppendorf tube. Tubes were centrifuged again at 800 x *g* for 5 min. The supernatant was aspirated, and pellets were either used for molecular biology experiments directly after or stored at -80℃ for long term storage.

2.1.4 Freezing of Cells

Any remaining cell suspension after passaging of cells, was centrifuged at 800 x *g* for 5 min to create cell pellets. The supernatant was discarded, and cell pellets were resuspended in 1mL of freezing media (90% FBS and 10% DMSO). This cell suspension was transferred into 1mL cryogenic vials. Vials were placed in a Mr Frosty Freezing container overnight at -80℃ before transferring vials into liquid nitrogen for long term storage.

2.2 3D Spheroid Culture

3D spheroid models were generated using the two SHH cell lines, DAOY and ONS-76 to mimic SHH tumour environment. The spheroid culture methods followed in this study have previously been optimised by Roper and Coyle (2022).

2.2.1 Preparation of Neurosphere Media

Spheroid generation and culture was done in neurosphere media. Neurosphere media composed of DMEM/F-12 supplemented with B-27, N-2, Heparin, epidermal growth factor (EGF) and basic fibroblast growth factor (bFGF) (**table 2.2.**). Fresh neurosphere media was prepared before generation of spheroids and stored at 4℃ for no longer than 2 weeks.

Table 2.2. details of the components to make up neurosphere growth media.

Media components	Stock Product Details	[Final]
Dulbecco's Modified Eagle's Medium/Nutrient Mixture F-12 (DMEM/F-12)	Gibco, 11320033	---
B-27 supplement	50x 10mL Gibco, 17504044	2%
N-2 supplement	100X in 5mL Gibco, 17502048	1%
epidermal growth factor (EGF)	0.1mg/mL Gibco, PHG0315	20ng/mL
basic fibroblast growth factor (bFGF)	0.1mg/mL Gibco, PHG0266	10ng/mL
Heparin	2mg/mL Stem Cell Technologies, 07980	2mg/mL

2.2.2 Spheroid Generation

DAOY and ONS-76 cells were cultured and grown as mentioned previously, until they reached a 70-80% confluency. Cells were harvested using Trypsin-EDTA and pelleted as mentioned in **section 2.1.2.** The pelleted cells were resuspended in neurosphere media, ready to be counted using a haemocytometer. Cells were resuspended in 1mL of neurosphere media. The haemocytometer consisted of a glass chamber were 10μL of the cell suspension was pipetted. Cells were then counted manually using a brightfield microscope. Using a standard click counter the number of cells was calculated in each square of the chamber. The total number of cells in the suspension was calculated using this formula:

Total Number of Cells per mL = Average Number of Cells per Square x 10^4

After cell counting, DAOY and ONS-76 cells were seeded into 96 well ultra-low attachment (ULA) plates (Corning, 7007) at a seeding density of 175 cells per well. These cells were seeded into a total volume of 200μL neurosphere media per well. To control the edge-effect and minimise evaporation of media, the outer wells of the ULA plates were filled with 200μL of PBS and contained no cells. Cells were placed in a 37℃ incubator with 5% CO_2 and humidified atmosphere to grow into spheroids. At day 4 of spheroid generation, a media change was performed, where half of the media (100mL) in all wells was replaced with 100mL of fresh neurosphere media.

All images of spheroids were taken on using the ZOE Fluorescent Cell Imager (BioRad) using the brightfield view. It was featured with an inbuilt calibration scale of 100mm (microns). At day 4 of spheroid generation the spheroids reached around 250mm in diameter when seeded at 175 cells per well.

2.3 Immunofluorescence (IF)

DAOY and ONS-76 spheroid models were stained for collagen and laminin to observe the structure of the ECM in these spheroid models. Spheroids were treated with two concentrations of AA, physiological (100μM) and supraphysiological (2.5mM) for 48-72 h to investigate the effects of different AA concentrations has on the ECM of spheroids.

2.3.1 Treating with AA and Transferring of Spheroids

Spheroids were generated as previously mentioned and day 4 spheroids were treated with 100μM and 2.5mM AA by removing 100μL of media in well and replacing it with 100μL of neurosphere media with 2x concentrated AA treatments. Spheroids were then incubated at 37℃ with 5% CO2 and humidified atmosphere. After 48 and 72 h post treatment, spheroids were transferred from ULA plate into a 96 well black wall plate by cutting ~2cm of a P200 pipette tip. Using this tip and a P200 pipette, around 150μL of volume of the ULA plate well was transferred into the 96 well black-walled plate, ensuring the spheroid was also successfully transferred. Once all spheroids were transferred into the 96 well black-walled plate, the plate was checked under a light microscope to reassure the presence of all spheroids, ensuring a successful transfer.

2.3.2 Staining of Spheroids for Collagen and Laminin

After the transfer of spheroids, the media in which the spheroids were transferred in was carefully removed, leaving around 50-75μL in the well to eliminate the loss of spheroid. To fix the spheroids, 100μL of 4% paraformaldehyde was added to each well and spheroids were incubated for 15 min at room temperature. After 15 min of fixation, PFA was carefully removed, and spheroids were washed twice in 100μL PBS. Spheroid plate was observed under light microscope in between all wash steps; this was done throughout the experiment to ensure no spheroids had been lost during the process. Spheroids were then permeabilised using 0.1% Triton X-100 in PBS (PBX) and incubated for 30 min at room temperature. PBX was removed and spheroids were washed twice with 100μL PBS. After permeabilization, 100μL of blocking buffer (10% goat serum in PBS) was added to each well and spheroids were incubated for an hour at room temperature. After the incubation the blocking buffer was removed, and spheroids were incubated in 70μL/well of either collagen (COL-1) or laminin (LAM A1+A2) primary antibodies (**table 2.3**). Spheroids were incubated for an hour at room temperature in primary antibodies. Spheroids were then washed twice with 100μL PBT (0.1% Tween-20 in PBS) for 10 min (first wash) and 15 min (second wash), at room temperature. Around 70μL of corresponding secondary antibody (**table 2.3**) was added to each well and incubated for an hour at room temperature and protected from light. Secondary antibody was carefully

removed from each well and spheroids were washed again twice with PBT as described before. After the PBT washes, spheroids were briefly equilibrated in PBS (~100μL/well). A counterstain was done to stain the nuclei of cells within the spheroids using 70μL of Hoechst 33342 (**table 2.3**). Spheroids were incubated in Hoechst for 5-10 min at room temperature, protected from light.

Table 2.3. Details of the antibodies and nuclear stain used for the immunofluorescence experiment.

Antibodies (Abs)/Stain	[Stock] Dilution	Ab Type Host Species	Product details
COL-1	1.4mg/mL 1:100	Primary Rabbit	Abcam, ab6308
LAMA1+A2	1mg/mL 1:100	Primary Rabbit	Abcam, ab7463
Alexa-Fluor 488 Anti-Rabbit	2mg/mL 1:100	Secondary Goat	Invitrogen™, A-11008
Hoechst 33342	20mM 1:4000	-	Thermo Scientific™, 62249

2.3.3 Confocal Imaging and Analysis

All IF stained spheroids where imaged using the ZEISS Celldiscover 7 (CD7) automated imaging system. For basic microscopy image acquisition and analysis was conducted on the ZEISS ZEN Lite software. If needed, further image processing was done on ImageJ2 software and quantitative data was processed on Microsoft Excel and GraphPad Prism® (version 9.4.1).

2.4 Molecular Biology

Preliminary data looking at the expression of AA and DHA transporters (SVCTs and GLUTs) and their correlation to survival outcomes in patients with SHH medulloblastoma showed that high expression of the AA transporter SVCT2 (*SLC23A2*) correlated with poorer survival outcomes in patients with SHH tumour type whereas in patients expressing high levels of GLUT10 (*SLC2A10*) transporter correlated to better survival outcomes (Jones, 2024). Therefore, gene and protein level expression of these two transporters were investigated in DAOY and ONS-76 cell lines.

2.4.1 RNA Isolation

DAOY and ONS-76 cell pellets were generated using methods described above. RNA was then extracted from these cell pellets using the Qiagen RNeasy Mini Kit (Qiagen, 74104) following the manufacturer's protocol. The concentration and purity of the eluted RNA was then measured using NanoDrop before storing RNA samples

at -80℃. Before loading any RNA sample, the nanodrop was calibrated by using a blank sample of nuclease-free water. RNA was analysed by pipetting 1μL of eluted RNA sample on to the NanoDrop sampling arm. The value of ~2.0 for the 260/280nm absorbance ratio was an indicator of 'pure' RNA. The sampling arm was cleaned with nuclease free water before and in between the loading of RNA samples.

2.4.2 Complementary DNA (cDNA) Synthesis

In order to run a qRT-PCR (quantitative reverse transcription-polymerase chain reaction) on DAOY and ONS-76 cell lines, the RNA isolated as described above was synthesised to cDNA. For the synthesis of cDNA, 2μg of RNA samples was diluted with nuclease-free water in 0.2mL PCR tubes achieving a final volume of 11μL. To this 1μL of dNTPs (deoxynucleotide triphosphates) and 1μL of random primers (**table 2.4.**) were added to samples and were incubated at 65℃ for 5 min then on ice for 1 min. After incubation, 1μL of 0.1M DTT (dithiothreitol), 1μL of RNaseOUT™ (ribonuclease inhibitor) 1μL of Superscript™ III reverse transcriptase (or 1μL of nuclease-free water in samples for no reverse transcriptase (NRT) controls and 4μL of 5x First Strand Buffer (**table 2.4.**) were added to the sample to make a final volume of 20μL. After adding the components of the reaction mix, samples were placed in a thermal cycler with a cDNA synthesis programme set at:

Temperature °C	Time (min)
25	5
50	60
70	15

Upon the completion of programme, the newly synthesised cDNA samples were stored at -20℃.

Table 2.4. Details of the reagents used for the synthesis of cDNA

Reagents	**[Stock]** **Product details** **Storage**
dNTP mix	25mM Thermo Scientific™, R1121 Store -20℃
Random primers	3µg/µL Invitrogen™, 48190011 Store -20℃
DTT	100mM Invitrogen™, 18080044 Store -20℃
First Strand Buffer	5x Invitrogen™, 18080044 Store -20℃
Superscript™ Reverse Transcriptase III	10,000 units at 200 U/µL Invitrogen™, 18080044 Store -20℃
RNaseOUT™	5000 units at 40U/µL Invitrogen™, 10777019 Store -20℃

2.4.3 Primer Designing

SVCT2 and *GLUT10* primers were designed using NCBI primer blast (https://www.ncbi.nlm.nih.gov/tools/primer-blast/) and Primer3 (https://primer3.ut.ee/). Ensembl site (http://www.ensembl.org/index.html) was used to view the genomic sequence and exon locations of the *SVCT2* and *GLUT10* genes. SnapGene tool (https://www.snapgene.com) was used to plan and visualise the potential primer pairs designed and additionally aid in the selection of optimal pairs. Information about all primer pairs designed shown in **Appendix A.**

2.4.4 Optimising Primer Annealing Temperatures Using Gradient PCR

To optimise the annealing temperature and specificity of primers a temperature gradient PCR was performed. In this method, several different annealing temperatures were used on control cDNA using the primer pairs designed. Reactions for each annealing temperature were conducted in 0.2mL PCR tubes to which 10µL of iQ™ SYBR® Green Supermix, 0.5µL of forward (FWD) and reverse (REV) primers (all primer pairs were ordered from Sigma-Aldrich which were reconstituted in nuclease-free water to make 1mL stock of 100µM primers, which were diluted further in nuclease-free water to make 10µM working aliquots), 8µL nuclease-free water and 1µL of 10ng/µL cDNA (**table 2.5.**). If 2ng of RNA was used to synthesise the cDNA, then the concentration of newly synthesised cDNA was ~100ng/µL. To get 1µL of 10ng/µL of cDNA for this experiment, 0.1µL of 100ng/µL cDNA was diluted with 0.9µL of nuclease-free water. NRT control samples were diluted in the same way. The PCR was then conducted using the thermal cycler. The settings of the PCR programme were set at:

Steps (with No. of cycles)		Time period	Temperature (°C)
Initial denaturation		2 minutes	95
Denaturation	x40 cycles	15 seconds	95
Annealing		30 seconds	56-63 (varied)
Extension		30 seconds	72
Final extension		5 minutes	72
Hold		-	4

To determine the optimal annealing temperature of the primer pairs for SVCT2 and GLUT10 genes **(table 2.6.)**, temperatures ranging from 56℃ to 63℃ were used for the annealing step of the PCR cycle and these PCR reactions with a range of annealing temperatures were analysed by agarose gel electrophoresis (**section 2.5.5.) (figure 2.1.).** This displayed the annealing temperature at which most product was yielded for the primer pair, which in turn identified as the optimal annealing temperature for that primer pair. Further optimisation of primers shown in **Appendix B**.

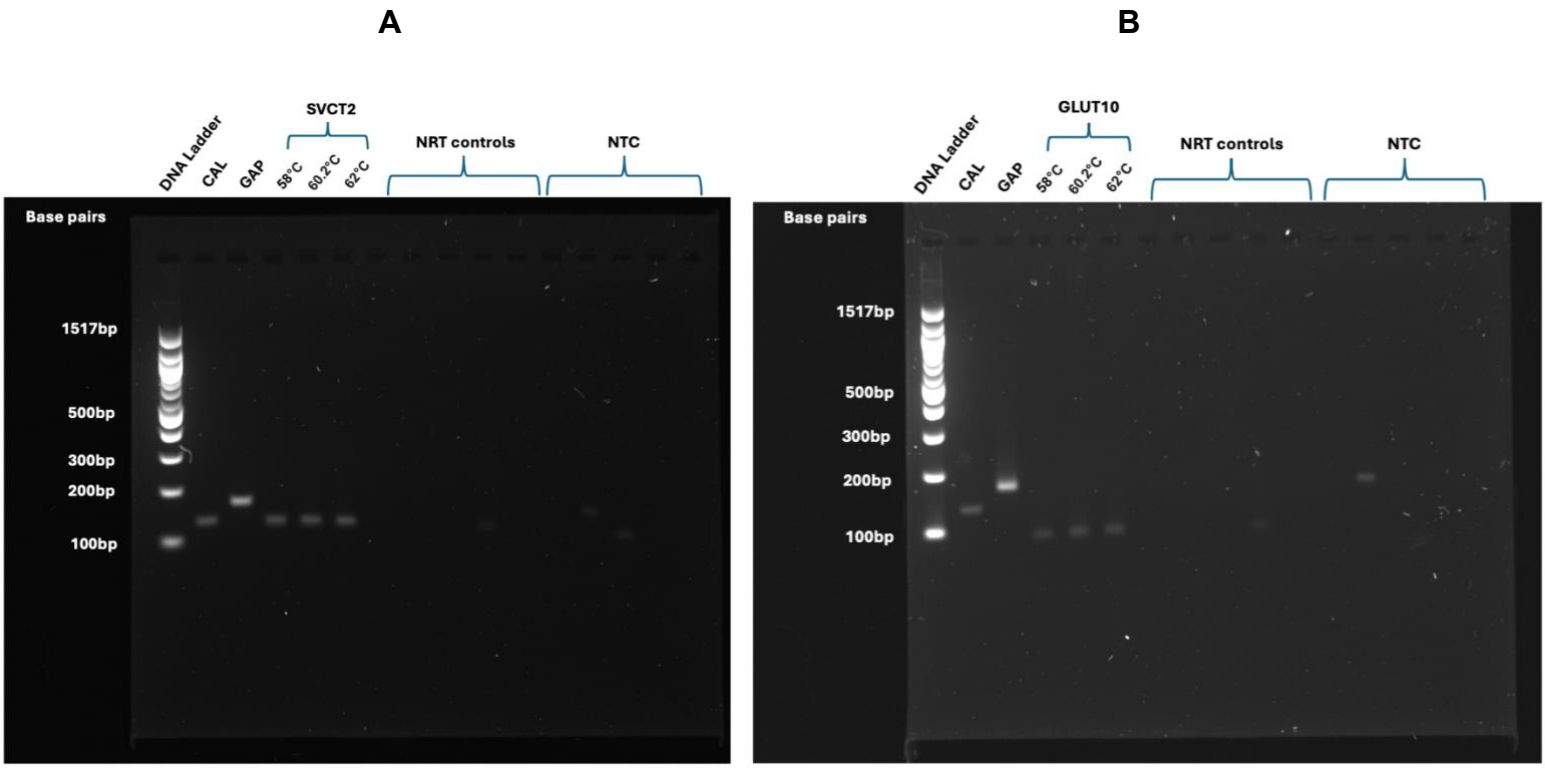

Figure 2.1. Images of agarose gel electrophoresis showing PCR products generated during the optimisation of annealing temperatures for SVCT2 primer pair (**A**) and GLUT10 primer pair (**B**). Gradient PCR was performed across a range of temperatures (56℃ to 63℃), with representative temperatures shown while full range of annealing temperature shown in the appendix. No reverse transcriptase (NRT) control included to eliminate any reagent contamination, and no template control (NTC) included to eliminate presence of genomic DNA in sample. Calnexin (CAL) and GAPDH (GAP) were used as positive controls. Expected product size for SVCT2 gene was at 132 bp, GLUT10 at 91 bp, CALNEXIN at 137 bp and GAPDH at 173 bp.

Table 2.5. Details of the reagents used for gradient PCR

Reagent	[Stock]	[Final]	Product details
iQ™ SYBR® Green Supermix	100 x 50µL reactions	-	BioRad, 1708880 Store -20℃
FWD primer	10µM	250nM	Sigma-Aldrich Store -20℃
REV primer	10µM	250nM	Sigma-Aldrich Store -20℃
cDNA	100ng/µL	10ng/µL	- Store -20℃
Nuclease free H_2O	-	-	- Store 25℃

2.4.5 Agarose Gel Electrophoresis

To visualise the products of the gradient PCR, PCR samples were loaded onto 2% agarose gel as the observed product length of all PCR products was <500 base pairs.

2.4.5.1 Preparing Agarose Gel

To obtain a 2% gel, 1 gram of agarose was weighed out and added to 50mL of 1x TBE (Tris-Borate-EDTA) buffer in a conical flask. The TBE buffer with agarose was microwaved for around 1 min in 15-30 second intervals, swirling flask in between and ensuring the agarose melts completely whilst not overheating the gel mixture. Once gel is a clear colour, 5µL of SYBR™ Safe DNA gel stain (Invitrogen™, 10328162) was added to the gel mixed by swirling. The gel was left to cool for 3-5 min at room temperature or until the surface of flask reached a comfortable temperature to hold for 5-10 s. Once gel was cooled accordingly, it was poured into its chamber with comb attached to form wells when set. Gel was left a room temperature to completely set.

2.4.5.2 Loading samples

Once gel was set, the comb was removed and was placed into the tank with gel still intact in the chamber. 2µL of 6x purple gel loading dye (New England Biolabs®, B7025S) was mixed with 10µL of PCR sample in a 0.5mL tube. The sample and dye were mixed well using a P20 pipette. TBE buffer was added over the agarose gel to flush out the wells and to fill up the tank (until entire gel and its wells were covered in TBE buffer). 12µL of sample and dye mixture were pipetted into each well alongside a DNA ladder with a base pair range relevant to the PCR product. This was then electrophoresed at 120 V for 45 min. Upon completion of the electrophoresis, the gel was imaged using a Bio-Rad® ChemiDoc imaging system.

2.4.6 qRT-PCR Gene Expression of *SVCT2* and *GLUT10*

qRT-PCR using SYBR-green chemistry was conducted to evaluate the relative gene expression of SVCT2 and GLUT10 in DAOY and ONS-76 cell lines. All qRT-PCR reactions were conducted in Applied Biosystems™ MicroAmp™ optical 96-Well reaction plates (Thermo Fisher Scientific, 4306737) in triple technical replicates for 5 experimental repeats (n=5). The master mix in each well comprised (same as section 2.5.4.) of 10µL of SYBR green supermix, 0.5µL of FWD and REV primers (*SVCT2*, *GLUT10* and housekeeping genes *calnexin* and *GAPDH*) (**table 2.6.**), 8µL nuclease free water and 1µL of 10ng/µL cDNA (**table 2.5.**). For each cDNA sample, a separate no transcript control (NTC) was also prepared where 1µL of cDNA was replaced with nuclease free water. NRT controls were also ran, where 1µL of cDNA was replaced with 1µL of NRT sample (generated during cDNA synthesis; section 2.5.2.). Once the plate was loaded with all the relevant samples, it was sealed using Applied Biosystems™ MicroAmp™ optical adhesive film (Thermo Fisher Scientific, 4311971). Upon optimisation, the annealing temperatures for both SVCT2 and GLUT10 primers was set at 60℃. Annealing temperature for control primers calnexin and GAPDH had previously been optimised to 60℃. The plate was then placed in the QuantStudio™ 5 Real-Time PCR machine, running the following programme:

Steps (with No. of cycles)		Time period	Temperature (°C)
Initial denaturation		2 minutes	95
Denaturation	x40 cycles	15 seconds	95
Annealing		30 seconds	60
Extension		30 seconds	72
Melt curve		Sections of 0.5°C increasing every 5 seconds	65-95

Table 2.6. Sequences of optimised SVCT2 and GLUT10 primers (FWD +REV) and housekeeping genes used for the qRT-PCR gene expression.

Primer	FWD/REV	Sequence (5' to 3')	Product size
SVCT2	FWD	TAGCCCCGTGGTTTAAGGTT	132 bp
	REV	CACAGGCGTAGTAGTCACCA	
GLUT10	FWD	TGGTCTTTGTCAGTGCCTTC	91 bp
	REV	GCTCTTCCTCGTATCTCCAC	
Calnexin	FWD	AGCCAAGAAAGACGATACCG	137 bp
	REV	CAGAGATGGCATGATGCTTG	
GAPDH	FWD	ATGTTCGTCATGGGTGTGAA	173 bp
	REV	GTCTTCTGGGTGGCAGTGAT	

2.4.7 Gene Expression Analysis

qRT-PCR results were analysed using the ΔCt method (Livak and Schmittgen, 2001), where Ct represents the cycle number where the PCR reaction produces fluorescence, distinguishable from any background noise. For this analysis the level of gene expression was normalised to the housekeeping genes calnexin and GAPDH by the following methods:

$$\Delta Ct = \text{average } \Delta Ct \text{ (}\textit{gene of interest}\text{)} - \text{average } \Delta Ct \left(\frac{\textit{calnexin} + \textit{GAPDH}}{2} \right)$$

$$\text{Relative gene expression} = 2^{-\Delta Ct}$$

All raw data was visualised and extracted from the Design & Analysis 1 (DA1) software; compatible with the QuantStudio™ 5 Real-Time PCR machine (Thermo Fisher Scientific). ΔCt values were calculated using Microsoft Excel and subsequent analysis of gene expression was conducted on GraphPad Prism® (version 9.4.1).

2.5 Treating Spheroids with AA and Cisplatin

Spheroids were generated and grown to day 4 where they were approximately 250-300mm in diameter. To assess the influence of high-dose AA on spheroid response to chemotherapy, day 4 spheroids were treated with a physiological concentration (100μM) and supraphysiological/high-dose (2.5mM) of AA (Carr and Frei, 1999), with and without the chemotherapeutic agent cisplatin. 1μM of cisplatin was used for all treatment experiments as the IC_{50} of cisplatin in 3D spheroid models was calculated to be at 1μM by Roper and Coyle (2022). AA and cisplatin treatments (**table 2.7.**) were prepared in neurosphere media on the day of experiment at a 2X concentration in Eppendorf tubes. 100μL of pre-existing media in wells of the ULA plate was removed using a P100 pipette and replaced with 100μL of the 2X treatments prepared, making total volume in each well 200μL with 1x final concentration of all treatments. Untreated spheroids and spheroids with 0.1% (v/v) DMSO (vehicle control) served as controls. Spheroids were treated with 1μM cisplatin, 100μM AA and 2.5mM alone and in combination. After adding treatment, spheroids were incubated at 37℃ with 5% CO_2 and humidified atmosphere. Spheroids were observed and imaged on ZOE fluorescent cell imager, using brightfield, at 0 (pre-treatment), 24, 48 and 72 h post treatment. Effect of the AA and cisplatin co-treatment on spheroid viability was measured with live dead staining of treated spheroids (**section 2.6**).

Table 2.7. Details of AA and cisplatin used in this experiment

Compound	Stock	Vehicle	Storage	Product Details
Ascorbic Acid	1M	PBS	Powder = room temperature, protected from light Stock solution = -80℃ freezer	Sigma-Aldrich, A92902
Cisplatin	1mM	DMSO	Powder = 2-8℃ fridge, protected from light Stock solution = -80℃ freezer	Sigma-Aldrich, 232120

2.5.1 Imaging and Size Analysis of Spheroids

Spheroids were imaged at before the addition of treatments (0 h) and 24, 48 and 72 h post treatments. All images of spheroids were taken on the ZOE fluorescent cell imager (BioRad) on brightfield view. Area (A) of spheroids were obtained using the 'Freehand Tool' to outline the spheroids at all timepoints. Using the area values, the radius (r) and volume (V) were calculated on Microsoft Excel, using these formulas:

$$r = \frac{\sqrt{A}}{\pi} \qquad v = \frac{4}{3}\pi r^3$$

2.5.1.1 Statistical Analysis of Spheroid Size Change

Measurements of spheroid area and volume at 24, 48, and 72 h after treatment were represented as a percentage change after being normalised to sizes obtained for pre-treatment (0 h). Statistical analysis was performed using a two-way mixed effect model with Geisser-Greenhouse correction to account for individual spheroid size variation. Tukey's multiple comparison test was carried out to compare each treatment group. Statistical significance was set at $p<0.05$. All analyses were conducted using GraphPad Prism® (version 9.4.1).

2.6 Live Dead Staining of Spheroids

A live dead staining was performed on spheroids post treatment, to measure spheroid viability. Calcein AM (Invitrogen™, C3100MP) was used for the staining of live cells and propidium iodide (Invitrogen™, P1304MP) was used to stain for dead cells. 70% EtOH (ethanol) was used as dead stain control. The stock solutions for Calcein AM and PI were thawed to room temperature and photo-protected by covering stock and working solutions in aluminium foil. A fresh 21x staining solution was made using PBS. The number of wells was used to determine the volumes of each component:

Calcein-AM (CAM): number of wells × 0.21µL

Propidium Iodide (PI): number of wells × 0.42µL

PBS volume = (number of wells × 10µL) − (Calcein AM + PI volumes)

To make the 21x staining solution, these components were mixed in an Eppendorf tube and slightly vortexed. Tube was photo-protected by aluminium foil. Without removing any preexisting medium, 10µL of this 21× staining solution was added straight to each well. After being loosely covered with aluminium foil to keep out light, spheroids were incubated for one hour at 37 °C in a humidified environment with 5% CO_2. After incubation, spheroids were imaged on the ZOE fluorescent microscope using the green channel (CAM/live stain) and red channel (PI/dead stain).

2.6.1 Quantification of Live/Dead Stained Spheroids

ImageJ2 software used to evaluate fluorescence pictures of live and dead stained spheroids. Regions of interest (ROIs) were manually established around individual spheroids in each image using the freehand tool. Using the integrated density parameter chosen in the "Set Measurements" dialogue, the "Measure" function was used to determine each channel's integrated density (ID). The background fluorescence was adjusted by multiplying the area of the spheroid ROI by the mean background intensity, which was calculated from three ROI-free sections in each image. Using Microsoft Excel software. the corrected IDs, the spheroid were calculated using the following formula:

$$\text{Spheroid Viability (\%)} = \frac{\text{Live (green ID)}}{\text{Live (green ID) + Dead (Red ID)}}$$

2.6.2 Statistical Analysis of Live/Dead Stained Spheroids

Measurements of spheroid viability were represented as percentage after being normalised to untreated control group. Statistical analysis was performed using a one-way ANOVA with Dunnett's multiple comparison test to compare each treatment group with untreated spheroids. Statistical significance was set at $p<0.05$. All analyses were conducted using GraphPad Prism (version 9.4.1).

Chapter 3: Investigating the Effect of AA on ECM Deposition in SHH Spheroids

3.1 Overview

The extracellular matrix (ECM) is a dynamic web of proteins and polysaccharides that supports tissues structurally and controls important cellular functions like migration, proliferation, and differentiation (Frantz et al., 2010a). The ECM influences mechanical characteristics, modifies signalling pathways, and influences drug delivery and resistance in tumours, all of which contribute to the tumour microenvironment (TME) (Lu et al., 2012). Furthermore, the development, invasiveness, and mechanical characteristics of cancer cells are significantly influenced by ECM remodelling (Girigoswami et al., 2021). ECM remodelling and composition have been linked to tumour growth, invasiveness, and treatment response in the SHH subgroup of medulloblastomas, as collagen dense “shell” structure found in these tumours characterises a better prognosis (Linke et al., 2023). Additionally, prolyl and lysyl hydroxylases, which hydroxylate and stabilise collagen, depend on AA as a cofactor to facilitate appropriate collagen folding and extracellular secretion (Peterkofsky, 1991b).

Collagen, especially types I and IV, are an important structural element of the ECM, and its structure and deposition are strictly controlled during tissue homeostasis and cancer growth (Rozario and DeSimone, 2010). Another key structure of the ECM is laminin. It is essential for preserving the integrity of the ECM, promoting cell adhesion, migration, differentiation, and enabling interactions with collagen networks (Domogatskaya et al., 2012a). In solid tumours, dysregulation of collagen and laminin deposition has been linked to increased tumour aggressiveness, decreased chemosensitivity and has altered tissue stiffness (Lu et al., 2011). Therefore, evaluating the ECM composition within tumour models is essential to comprehending the ways in which the ECM is crucial in navigating tumour biology.

As mentioned previously, in order to stabilise the collagen triple helix and encourage its release into the extracellular space, prolyl and lysyl hydroxylases require AA as a cofactor, making AA a crucial element in collagen biosynthesis (Peterkofsky, 1991b) and beyond its structural function, AA also modifies signalling pathways that control ECM formation and remodelling and helps maintain cellular redox equilibrium. AA availability has a direct impact on ECM deposition in cancer cells, which may change the mechanical characteristics, architecture and response to chemotherapy in SHH spheroid models (Wohlrab et al., 2022, Mandl et al., 2009).

3D spheroid models represent the TME very well, including the ECM structure of the tumour (Friedrich et al., 2009). Techniques like immunofluorescence staining allows the special visualisation of ECM proteins within spheroid models, which in turn offers information about the distribution, density, and structure of ECM in response to experimental perturbations, like drug treatments. In this chapter SHH spheroid models were treated with physiological AA (100µM) and supraphysiological AA (2.5mM) to understand whether AA availability may alter the ECM deposition in SHH medulloblastoma spheroids.

3.2 Visualising Type I Collagen and Laminin in SHH Spheroids Treated with AA

To visualise the distribution of extracellular matrix (ECM) components, particularly collagen and laminin, SHH spheroids treated with either low (100μM) or high (2.5mM) doses of AA. Day 4 SHH spheroids were treated with AA and incubated for 48-72 h. Upon incubation, spheroids were stained for immunofluorescent labelling of type I collagen (COL1) and laminin (LAM) (**section 2.3**). Collagen staining was primarily seen more in spheroid periphery, indicating that collagen fibres are primarily found in the outer extracellular matrix (ECM) area or "shell-like" layer surrounding the spheroid. Laminin staining, on the other hand, was seen all around the spheroid, suggesting a more consistent distribution in both the centre and periphery areas (**figure 3.1**). Qualitative observation of these images displays slight increase in fluorescence intensity of collagen staining, as the concentration of AA treatment increased for DAOY spheroids compared to ONS-76 spheroids. This is observed for both cell lines. However, fluorescence quantification could not be accurately conducted because the experiment was only repeated twice, with limited technical repeats due to considerable spheroid loss throughout the staining and transferring process. The observed distribution patterns of collagen and laminin under the two treatment conditions are qualitatively illustrated by representative confocal pictures.

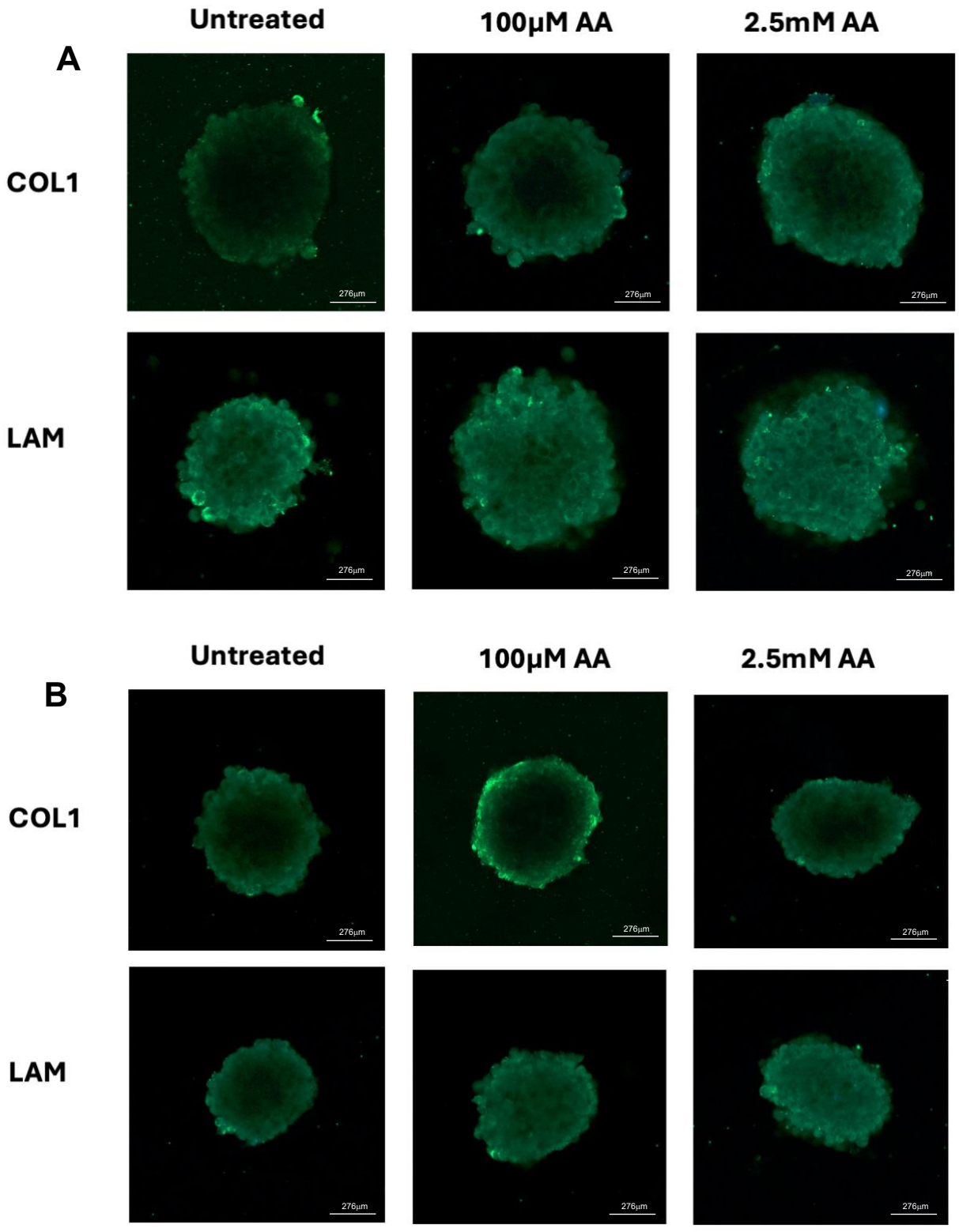

Figure 3.1 Immunofluorescence staining of SHH spheroids for type I collagen (COL1) and laminin (LAM). Representative confocal microscopy images of DAOY (**A**) and ONS-76 (**B**) spheroids stained for collagen and laminin. Confocal images taken using ZEISS Celldiscover 7 and processed using ZEISS ZEN Lite software. Spheroids were either untreated or treated with 100µM of AA (low) or 2.5mM (high) and stained for type I collagen (COL-1) or laminin (LAM A1+A2). Scale bar = 276µm.

3.3 Discussion

The spatial distribution patterns of laminin and type I collagen seen in this chapter offer initial qualitative proof that the ECM organisation in SHH medulloblastoma spheroids is both biologically significant and structured. The more diffuse visual distribution of laminin throughout the spheroid body and the peripheral accumulation of collagen are consistent with the architectural characteristics reported in SHH medulloblastoma tumours in vivo and start to suggest how AA availability may regulate this structure.

3.3.1 ECM structure in SHH spheroids

The qualitative pattern seen in SHH spheroids staining for collagen is consistent with earlier research indicating that these tumours have a structured extracellular matrix organisation, with collagen tending to build up in an outer "shell-like" ECM layer and other matrix proteins, like laminin, dispersed more widely throughout the spheroid. This pattern aligns with research findings published by Linke et al. (2023), where they showed that SHH medulloblastoma nodules contribute to a unique shell architecture surrounding the tumour masses by forming an exterior ECM rich in collagens and small leucine-rich proteoglycans (SLRPs). Similar spatial structure may be reflected in the peripheral location of collagen, which could assist the structural integrity and compartmentalisation of SHH spheroids.

Laminin staining, on the other hand, was more widely dispersed throughout the spheroid, including the core areas. This is in line with laminin's known functions as a component of the basement membrane that interacts with various cell types in various tissue compartments (Domogatskaya et al., 2012b). Collagen IV and other ECM elements are known to interact with laminin networks to create a structural framework that promotes cell adhesion, polarity, and signalling (Yurchenco, 2011). The more distributed laminin within the spheroid body maybe displaying the active laminin deposition in contract to collagen seen more around the periphery of the spheroid body. The varied spatial arrangement of both laminin and type I collagen preliminarily seen may imply that laminin and collagen have separate but complimentary structural functions within SHH spheroids, with laminin sustaining the larger cellular scaffold and collagen mainly contributing to the outer structural shell.

3.3.2 The Effect of AA on SHH Spheroid ECM

In DAOY spheroids, there was a qualitative rise in collagen fluorescence intensity as AA concentration increased; this impact was less noticeable in ONS-76 spheroids. This can be supported by AA's recognised function as a cofactor for prolyl-4-hydroxylase and lysyl hydroxylase, enzymes necessary for hydroxylating proline and lysine residues during collagen production (Peterkofsky, 1991a). Under hydroxylated procollagen chains cannot fold into a stable triple helix in the absence of sufficient AA, and instead of being released into the extracellular space, they are kept in the endoplasmic reticulum and broken down (Gorres and Raines, 2010).

In addition to its direct enzymatic function in collagen biosynthesis, AA's antioxidant qualities and impact on epigenetic regulators like TET enzymes and HIF-1α may also influence ECM remodelling (Camarena and Wang, 2016, Maekawa et al., 2022).

According to Gilkes et al. (2014), HIF-1α, which is stabilised under hypoxic circumstances typical of the spheroid core, is known to upregulate matrix metalloproteinases (MMPs) and suppress collagen crosslinking enzymes such lysyl oxidase (LOX), contributing to a more disordered extracellular matrix. Therefore, the observed increases in structured collagen deposition at higher AA dosages, specifically in DAOY SHH spheroids can be partly explained by AA-mediated destabilisation of HIF-1α, however further research is necessary to fully understand this mechanism.

Overall, this pilot investigation supports the idea that ECM composition is crucial to SHH medulloblastoma architecture by providing qualitative evidence that collagen and laminin occupy discrete spatial niches inside SHH spheroids tumour models.

3.3.3 Limitations

The interpretive reach of this chapter's conclusions is limited by several significant constraints, regardless of the biological significance of these observations. The high loss of spheroids throughout the immunofluorescence staining procedure was the biggest technical obstacle. The frequent washing and transfer procedures necessary for the IF staining experiment had resulted in the loss of almost two thirds of the spheroids. This in turn significantly reduced the quantity of technical and biological replicates available for study. Due to the small sample size, quantitative image analysis could not be carried out (Schindelin et al., 2012). As a result, all observations are still qualitative and are to be viewed as preliminary data rather than definitive. In cell biology research, credible quantitative comparisons are generally thought to need at least three independent biological duplicates with numerous technical replicates per condition. At this point, observed patterns cannot be differentiated from experimental variability due to lack experiment repeats.

Furthermore, this experiment only looked at type I collagen and laminin, two components of the extracellular matrix. Fibronectin, collagen IV, tenascin, and other proteoglycans are just a few of the many additional proteins that make up the ECM, where it may be differentially regulated by AA and contribute to the overall mechanical and signalling properties of the TME (Frantz et al., 2010b). Looking at more than two components that make up the ECM may paint a wider picture of the complexities the ECM holds within a spheroid.

3.3.4 Future Work

This investigation has quite a lot of scope to build up on the qualitative findings via several optimisation and experimental approaches. Optimising the workflow for handling and staining spheroids should be the top focus to reduce spheroid loss. This might be accomplished by using wide-bore pipette tips to lessen mechanical shear pressures during transfer or using low-binding microcentrifuge tubes (Nunes et al., 2019). To enable statistical comparison of fluorescence intensities across treatment conditions using suitable quantitative methodologies, a minimum of three independent biological replicates should be carried out after a dependable protocol has been established.

An essential supplementary method that would allow the direct measurement of ECM protein expression and secretion levels in response to AA therapy is western blotting. Whole cell lysates and media collected from AA-treated DAOY and ONS-76 spheroids could be probed with antibodies against type I collagen and laminin α1/α2, fibronectin, and collagen IV to provide a quantitative measure of intracellular protein levels and extracellular secretion. As this precisely detects the secreted portion of ECM proteins, which represents the net output of collagen production and hydroxylation downstream of AA activity (Peterkofsky, 1991).

Chapter 4: Investigating AA and DHA transporters in SHH medulloblastoma

4.1 Overview

Ascorbic acid, also known as vitamin C, is an essential micronutrient that plays a crucial role in cellular redox equilibrium, collagen formation, and epigenetic control. The sodium-dependent vitamin C transporters (SVCTs) and the glucose transporters (GLUTs) are the two transporter families responsible for its intracellular distribution and uptake. Among these, GLUT10 (encoded by SLC2A10) is involved in the intracellular recycling of ascorbate and the transport of dehydroascorbic acid (DHA), whereas SVCT2 (encoded by SLC23A2) mediates the active transport of reduced AA (Corti et al., 2010, Linster and Van Schaftingen, 2007). Previous bioinformatic investigations that involved screening 8 known DHA/AA transporter genes in medulloblastoma patient gene datasets from Pfister et al (2011) and Cavalli et al (2017) identified SLC2A10 (GLUT10) and SLC23A2 (SVCT2) genes significantly differentially expressed in SHH (**figure 4.1**) (Jones, 2024). Jones (2024) found high expression of SVCT2 was associated with poor survival outcomes whilst better survival results were associated with high GLUT10 expression. These results imply that SVCT2 and GLUT10 might be functionally distinct redox regulators in SHH tumours, potentially affecting their responsiveness to treatment and metabolic adaptability.

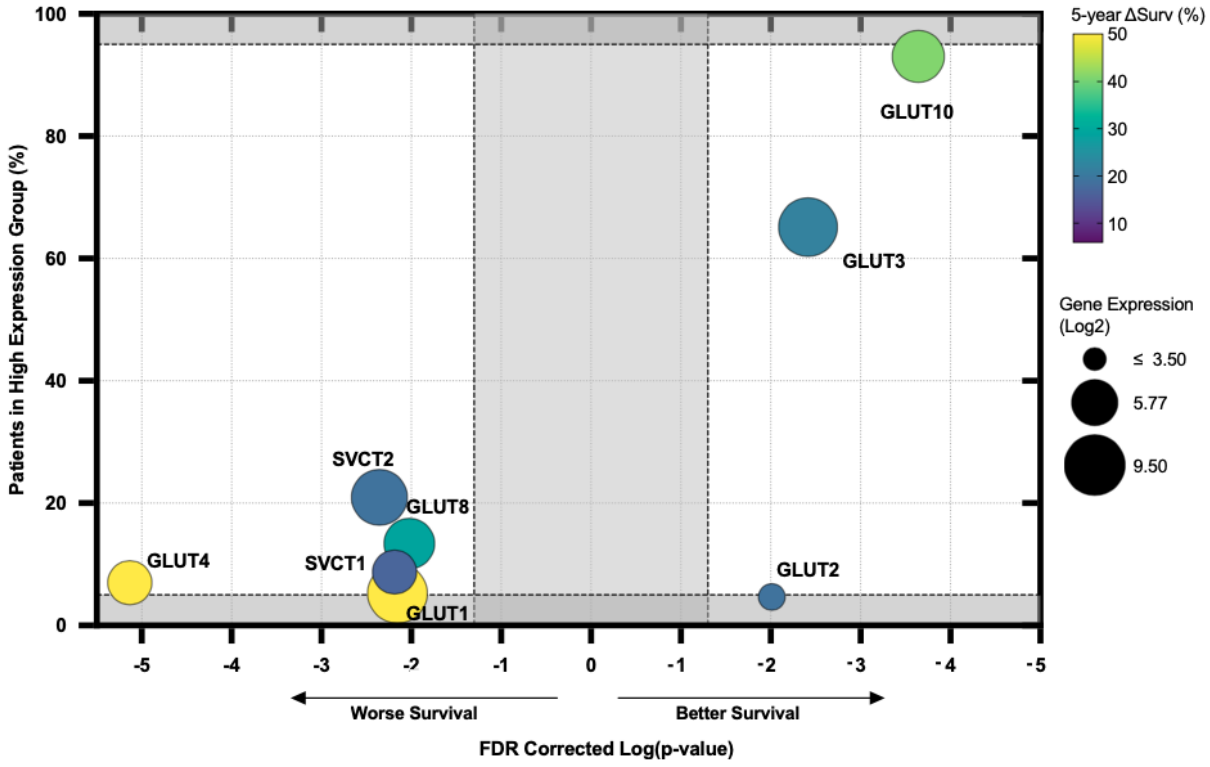

Figure 4.1 Association of 8 known AA/DHA transporters to survival outcomes in patients with SHH medulloblastoma. Bubble plot representing the 8 known AA/DHA transporters and their expression associated to patient survival outcome. Furthermore, for GLUT10 Kaplan-Meier analysis separated patients into the top 85% (high expressing) and bottom 15% (low expressing). This separation being strongly correlated with patient outcome (corrected log p-value= -3.641) and patients expressing high SVCT2 at 21% and low expressing SVCT2 at 79% correlating strongly with a negative patient outcome (corrected log p-value = -2.356) (Jones, 2024). SHH patient dataset n=172 (Cavalli et al 2017).

4.2 Gene Expression of SVCT2 and GLUT10 in SHH Spheroids

Quantitative PCR (qRT-PCR) was used to measure the levels of SLC23A2 and SLC2A10 gene expression in two well-known SHH medulloblastoma cell line spheroid models, DAOY (**figure 4.2** (**A**)) and ONS-76 (**B**). In order to create two opposing models, one enriched for SVCT2 expression and the other for GLUT10, the objective was to ascertain expression levels of GLUT10 and SVCT2 transporters and if two cell lines (DAOY and ONS-76) could be identified with different expression levels of these transporters to generate differential transporter expression models that mirrored good and poor patient outcome.

In DAOY and ONS-76 spheroids, quantitative PCR analysis showed detectable expression of both *SVCT2* and *GLUT10*, presented as relative expression ($2^{-\Delta CT}$) and normalised to housekeeping genes (*GAPDH* and *CALNEXIN*). qPCR and relevant analysis were carried out via methods mentioned in **section 2.4.6** and **2.4.7.** SVCT2 expression appeared higher in DAOY spheroids than in ONS-76 (**figure 4.2**). To ascertain whether the observed variations in gene expression between the two cell lines were statistically significant, an unpaired t-test was performed and according to the analysis SVCT2 and GLUT10 expression did not differ significantly ($p>0.05$) amongst the two SHH cell lines.

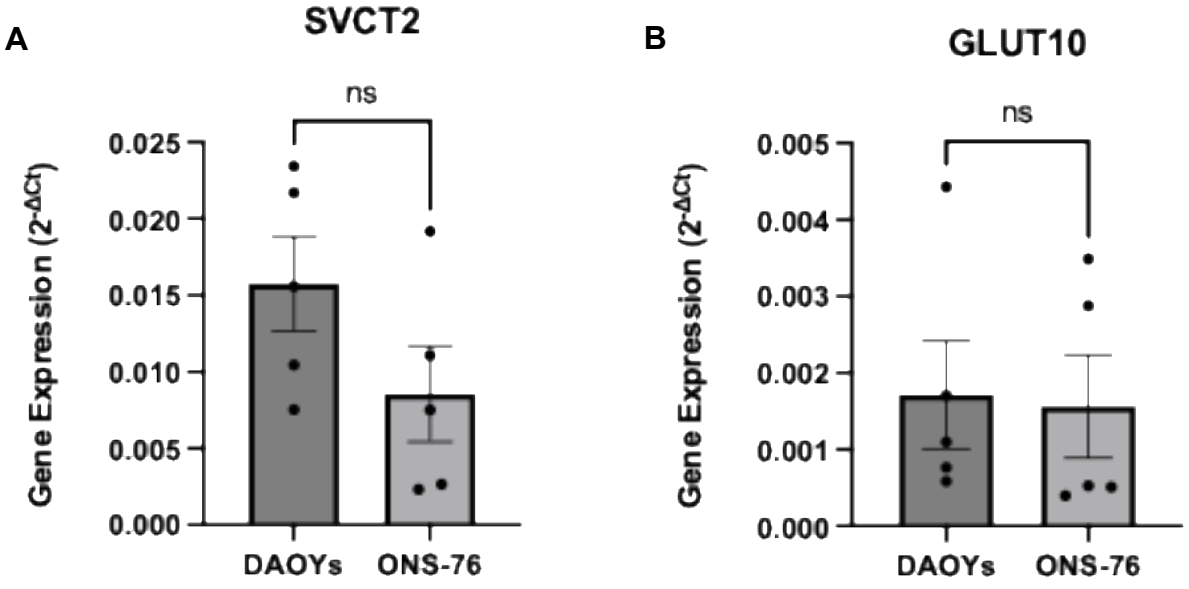

Figure 4.2 Relative gene expression of SVCT2 (*SLC23A2*) and GLUT10 (*SLC2A10*) in DAOY and ONS-76 SHH cell lines. The ΔCT method (**section 2.4.7**) was used to calculate the relative gene expression levels of SVCT2 (**A**) and GLUT10 (**B**) in DAOY and ONS-76 cell lines. Error bars represent the mean ± SEM; n=5 with 3 internal replicates. An unpaired (two-tailed) t-test was performed to assess statistical differences in gene expression of each transporter between the two cell lines; statistical significance measured at *p<0.05.* Unpaired t-test results; **A**) SVCT2, *p=0.14, ns* and **B**) GLUT10, *p=0.88, ns*.

4.3 Discussion

4.3.1 Differential Expression of SVCT2 and GLUT10 in SHH spheroids

The low expression of SVCT2 in DAOY spheroids is in line with previous studies showing that SVCT2 is frequently activated in hypoxic or aggressive tumour environments, where higher AA absorption supports collagen synthesis and cellular survival under oxidative stress (Li et al., 2020, Wohlrab et al., 2022). This may indicate that to maintain redox homeostasis, DAOY spheroids rely more on AA mediated antioxidant defences. This could be crucial in densely packed spheroids that undergo localised hypoxia. On the other hand, as GLUT10 has been linked to DHA transfer to mitochondria, which improves antioxidant recycling and mitochondrial efficiency, the trend of increased GLUT10 expression in ONS-76 spheroids may represent a more oxidative and less hypoxic cellular phenotype (Lee et al., 2010). This implies that there is heterogeneity within the SHH subgroup, as demonstrated by the DAOY and ONS-76 cell lines, where tumours in the same subgroup may differ in their intrinsic metabolic pathways, affecting how they maintain redox equilibrium and their chemosensitivity as well as their response to AA.

4.3.2 The Rationale for Investigating SVCT2 and GLUT10

Previous bioinformatic analysis of two separate medulloblastoma patient datasets served as the basis for the decision to concentrate on GLUT10 and SVCT2 rather than the larger panel of AA/DHA transporters (Cavalli et al., 2017, Northcott et al., 2011b). SLC2A10 (GLUT10) and SLC23A2 (SVCT2), two of the eight known AA/DHA transporter genes screened, were found to be the most significantly differentially expressed in the SHH subgroup and, crucially, showed conflicting correlations with patient survival (Jones, 2024), This difference has biological significance: GLUT10 mainly facilitates DHA transport and its intracellular recycling back to ascorbate, especially within the mitochondria, whereas SVCT2 is the main transporter in charge of the active uptake of reduced ascorbate into cells (Tsukaguchi et al., 1999). The fact that these two transporters, which play complementary but mechanistically different roles in the ascorbic acid redox cycle, should exhibit conflicting prognostic signals raises the possibility that they represent essentially distinct metabolic states within SHH tumours. Therefore, examining both transporters simultaneously provides an insight to examine how AA import and DHA recycling interact in relation to tumour redox biology and treatment response.

4.3.3 Limitations

It is difficult to draw firm conclusions on differential transporter expression between the two cell lines because the observed differences in SVCT2 and GLUT10 expression between DAOY and ONS-76 spheroids did not reach statistical significance ($p=0.14$ and $p=0.88$, respectively). The biological diversity of spheroid culture models which are known to show heterogeneity in cell density, hypoxic gradients, and nutritional availability depending on spheroid size, may contribute to the lack of significance (Däster et al., 2017, Hirschhaeuser et al., 2010). Despite

several experimental repeats (n=5), to increase statistical power, spheroids normalised to size could be used for future research.

This investigation was limited to the mRNA level using qPCR and gene expression does not always correspond to protein abundance or transporter activity. Protein stability and post-transcriptional and post-translational regulatory processes can significantly separate mRNA and protein levels. The functional significance of the observed transcriptional variations is still unclear in the absence of complementary western blotting or immunofluorescence evidence verifying SVCT2 and GLUT10 expression at a protein level.

Furthermore, the two SHH medulloblastoma cell lines used in this investigation, DAOY and ONS-76, might not fully represent the molecular heterogeneity of the SHH subgroup. Although both cell lines are well-known models, their unique genetic origins and mutation profiles may have an independent impact on transporter expression regardless of SHH pathway activity. These results might be more broadly applicable if more SHH cell lines or patient-derived models were included.

To better understand the metabolic profile of SHH spheroids a Seahorse XF Cell Mito Stress Test was also used to evaluate oxygen consumption rate (OCR) and mitochondrial activity in treated spheroids. However, there were a lot of technical difficulties with spheroid-based metabolic profiling. Spheroid transfer into Seahorse plates needed significant accuracy, and the assay was spheroid size-dependent and variability in our SHH spheroid integrity and size prevented consistent results from being produced within the allotted time, even after several optimisation attempts. However, further refinement of this technique, possibly by embedding spheroids in suitable matrix or employing specialist 3D culture plates may gather important information about the oxidative metabolism and mitochondrial respiration in SHH spheroids and how AA and DHA transporters may be influenced in these processes.

4.3.4 Future Work

These preliminary results justify additional research into how AA and DHA transport patterns may contribute to functional variation between SHH models, even if the observed differences were not statistically significant. Stronger proof of transporter expression patterns and their subcellular localisation would come from validation at the protein level using methods like Western blotting or immunofluorescence, which may be beneficial for future research. Subsequently, functional assays that measure intracellular AA and DHA uptake, mitochondrial ROS, NADPH/$NADP^+$ ratios, and sensitivity to supraphysiological AA with or without cisplatin would test whether transporter expression predicts treatment response, as demonstrated in other preclinical systems where vitamin C changed central carbon metabolism and redox state and pharmacologic AA increased chemosensitivity in pancreatic cancer models (Espey et al., 2011). Overall, these were the first steps in investigating the expression of AA and DHA transporters in SHH tumour models. The potential metabolic variability within this subgroup may be reflected by the observed differences in SVCT2 and GLUT10 expression between DAOY and ONS-76 spheroids, indicating that differences in AA/DHA absorption and redox management may affect tumour behaviour and treatment response. Determining how these transporters affect AA metabolism and contribute to the redox dynamics of SHH

medulloblastomas will need building on our study through integrated metabolic profiling and protein-level validation.

To obtain accurate oxygen consumption rate (OCR) and extracellular acidification rate (ECAR) data, future research should also focus on optimising Seahorse-based metabolic profiling for spheroid models, such as by using standardised spheroid sizes or a more thorough spheroid transferring technique. Building on the initial efforts in this investigation, this would allow direct evaluation of whether variations in transporter expression correlate with variations in oxidative phosphorylation and glycolytic activity.

To improve the potential of this study it is important to include more GLUT and SVCT transporter family members in addition to GLUT10 and SVCT2. GLUT4 (*SLC2A4*) is particularly interesting since it is an insulin-regulated transporter that is primarily linked to the uptake of glucose in muscle and adipose tissue, but it has also been shown to transport DHA and has been found in situations involving brain tumours (Medina and Owen, 2002, Rumsey et al., 1997). Jones (2024) shows many other GLUT transporters linked to different survival outcomes for patients. GLUT4 is one potential candidate that would be interesting to research alongside GLUT10 as expression of GLUT4 was shown to be associated with the worst survival outcome in patients with SHH medulloblastoma. Investigating these two transporters would address the question of how two transporters that belong to the same family influence such opposite survival outcomes.

Finally, stable knockdown or overexpression of SVCT2 and GLUT10 utilising short hairpin RNA (shRNA) (Rossi et al., 2023) or CRISPR-Cas9 (Ran et al., 2013) gene editing techniques would enable direct examination of functional involvement in AA metabolism, redox control, and sensitivity to AA and cisplatin co-treatment in DAOY and ONS-76 spheroid models.

Chapter 5: Investigating the Effect of AA and Cisplatin Co-treatment on SHH Spheroid Models

5.1 Overview

The conventional medulloblastoma treatment regimens include surgical removal of tumours, craniospinal irradiation, and chemotherapies like cyclophosphamide, vincristine and cisplatin. Long-term neurotoxicity and tumour recurrence continue to be major clinical issues despite increases in survival, highlighting the need for therapeutic approaches that maximise effectiveness while limiting adverse effects.

AA has gained attention as a possible adjuvant in cancer treatment. In addition to its traditional functions as an antioxidant and a cofactor in the synthesis of collagen, AA has concentration-dependent redox effects that can alter viability of cancer cells. This is seen in pancreatic cancer cells, where pharmacological concentrations of AA were shown to synergise with the chemotherapy gemcitabine (Espey et al., 2011). AA is a strong antioxidant that scavenges reactive oxygen species (ROS) and preserves intracellular redox equilibrium at physiological doses (≤100μM). On the other hand, AA demonstrates pro-oxidant characteristics at pharmacological or supraphysiological concentrations (≥1mM), producing hydrogen peroxide and free radicals that specifically destroy cancer cells with weakened antioxidant defences (Du et al., 2012b, Espey et al., 2011).

Cisplatin is a platinum-based chemotherapy (**figure 5.1**) that targets DNA and causes crosslinking along with generating ROS to induce cytotoxicity in cancer cells. It is a widely used chemotherapeutic agent, either alone or in combination with other therapies, especially in head and neck cancer (Forastiere, 1994). However, there is a chance that cancer cells can develop resistance towards cisplatin by upregulating antioxidants like glutathione (GSH) and catalase (Godwin et al., 1992, Spitz et al., 1993).

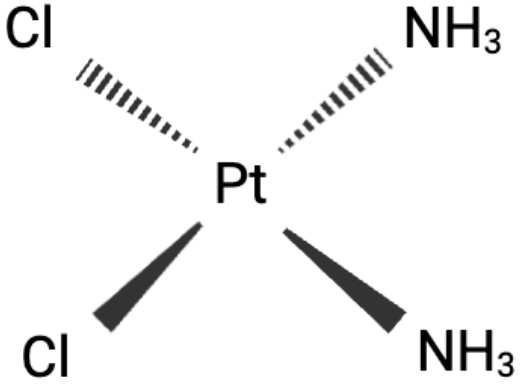

Figure 5.1 The chemical structure of cisplatin (chemotherapeutic agent).

Preclinical research shows that high-dose AA increase cancer cell sensitivity to cisplatin by increasing oxidative stress, decreasing intracellular GSH, and compromising DNA repair processes. This is seen in Dalton's lymphoma tumour cells and gastric cancer cells (Ghavami and Sardari, 2020, Longchar and Prasad, 2015). Despite seeing the promising effects of AA as a co-treatment with cisplatin in a handful of other cancer cell lines, along with other chemotherapeutic agents, very little of this has been explored in medulloblastomas (Wilson et al., 2014). This promising property of AA is also under-explored in 3D tumour models despite 3D models best resembling the TME compared to 2D cultures. This chapter examines how ascorbic acid (AA) at physiological (100μM) and supraphysiological (2.5mM)

levels affects the integrity, viability and susceptibility of SHH medulloblastoma spheroid models to chemotherapy.

5.2 Changes in SHH Spheroid Morphology Post AA and Cisplatin Co-treatment

DAOY and ONS-76 spheroids were grown to day 4 (**section 2.2.2**) and treated with 100μM AA, 2.5mM AA, 1μM cisplatin alone and in combination (100μM AA + 1μM cisplatin, 2.5mM + 1μM cisplatin) (**section 2.5**). Brightfield microscopy was used to analyse spheroid morphology at 0 (pre-treatment), 24, 48, and 72 h after treatment in order to evaluate the structural and morphological effects of ascorbic acid (AA) and cisplatin, both separately and together. This experiment was repeated three times to ensure reliability and precision of results.

Throughout the observation period, the morphology of the untreated control and 0.1% DMSO vehicle control spheroids remained spherical and compact. Similarly, spheroids treated with 100μM AA and 2.5mM AA alone had no visible change to spheroid morphology and remained healthy and viable. On the other hand, spheroids treated with cisplatin alone (1μM) showed obvious symptoms of cytotoxic stress which was reflected in the unhealthy morphology of these spheroids. Subsequent spheroid disintegration was seen, increasing with timepoints. This was expected as cisplatin is a chemotherapeutic agent forming DNA crosslinks that halt DNA replication and transcription along with generating ROS as well as causing mitochondrial dysfunction (Florea and Büsselberg, 2011).

Both DAOY (**figure 5.1 (A)**) and ONS-76 (**figure 5.1 (B)**) spheroids showed much better structural preservation when treated with cisplatin and 100μM AA (physiological) in comparison to when treated with cisplatin alone. There were noticeably fewer disassociated cells and less spheroid disintegration. Spheroid disassociation was increased over time in treatment group, but at a lesser extent compared to cisplatin alone and in combination supraphysiological AA (2.5mM) This effect on spheroid morphology indicates that cisplatin-induced damage was partially offset by AA at physiological concentrations. AA largely serves as an antioxidant at physiological doses, scavenging reactive oxygen species and promoting redox equilibrium; thus cytoprotecting the spheroids from cisplatin induced toxicity (Du et al., 2012b).

However, co-treatment of cisplatin and supraphysiological AA (2.5 mM) in spheroids of both cell lines, caused significant morphological degradation. As early as 24 h post treatment, there was noticeable spheroid disintegration, which got worse with time. After 72 h, the spheroids showed signs of significant loss of spherical structure and increased cell disassociation. This suggests that supraphysiological AA increases cisplatin cytotoxicity causing an increase in tumour death than cisplatin alone. This finding coincides with research from other cancer models where high-dose AA boosts chemotherapy via its pro-oxidant pathway (Chen et al., 2008, Lee et al., 2019).

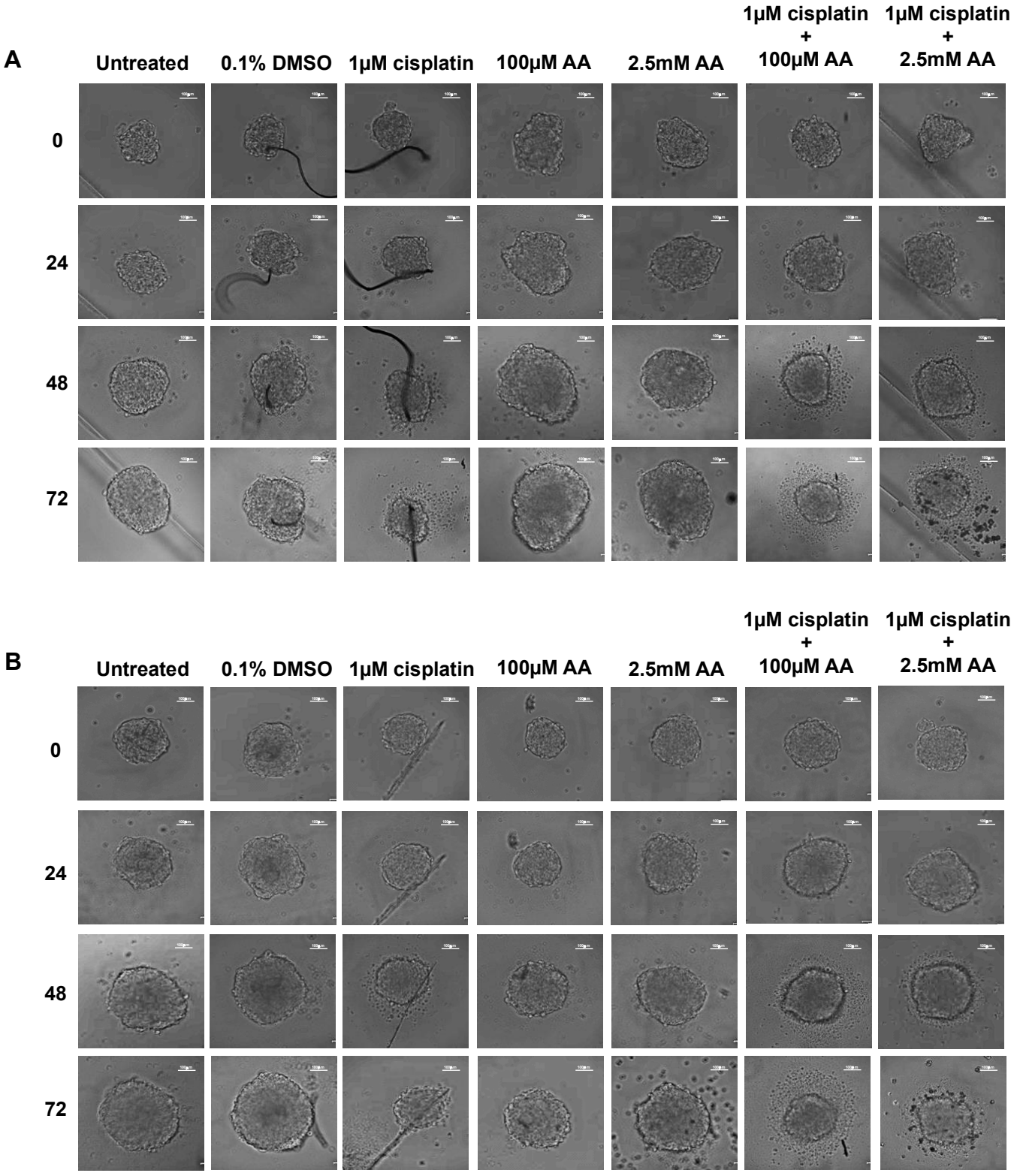

Figure 5.1 Brightfield images of AA and cisplatin co-treated DAOY and ONS-76 spheroids. Representative images of DAOY (**A**) and ONS-76 (**B**) spheroids treated with media only (untreated), vehicle control (0.1% DMSO), 100μM AA, 2.5mM AA, cisplatin alone, or cisplatin in combination with 100μM or 2.5mM AA. Day 4 spheroids imaged before adding treatment (0) and then were imaged 24, 48 and 72 h after adding treatment. Images were taken on ZOE fluorescent cell imager on brightfield channel; n=3 with three internal replicates. Scale bar: [100μm].

5.3 Changes in SHH Spheroid Size Post AA and Cisplatin Co-treatment

Quantitative examination of spheroid growth dynamics was carried out by calculating projected area from brightfield images before AA treatment (**figure 5.2**) and AA and cisplatin co-treatment (**figure 5.3**) and 24, 48 and 72 h post-treatment in order to complement the qualitative morphological observations. Area all spheroid models were obtained as mentioned in **section 2.5.1.** Percentage change area of spheroids for 24, 48 and 72 h post-treatment timepoints were normalised to their pre-treatment followed by the appropriate statistical analysis (**section 2.5.1.1.**). Volumes of both DAOY and ONS-76 spheroids were estimated from area using formula mentioned in **section 2.5.1** and data representing estimated volumes is shown in **figures C1 and C2 (Appendix C).**

Over the course of 72 h, the mean area of spheroids increased gradually and consistently from 83,287 ± 35,779μm^2 (**mean ± SD, n=3**) at 0 h to 168,539 ± 55,547μm^2 at 72 h for DAOY spheroids and 91,031 ± 45,727μm^2 at 0 h to 196,528 ± 47,742μm^2 at 72 h for ONS-76 spheroids, indicating normal proliferation and cellular integrity maintenance. This was seen in both DAOY and ONS-76 spheroids and was consistently observed in all experimental repeats of n=3. This was also observed in the vehicle control group (0.1% DMSO) where mean area for DAOY spheroids treated with 0.1% DMSO increased from 98,985 ± 41,801μm^2 at 0 h to 197,916 ± 49,869μm^2 at 72 h and for ONS-76 spheroids treated with 0.1% DMSO, size increased from 105,334 ± 34900μm^2 at 0 h to 201,773 ± 45,158μm^2 at 72 h - which was expected as DMSO at 0.1% was not toxic to both DAOY and ONS-76 spheroids, thus allowing normal growth.

Upon obtaining area of DAOY and ONS-76 spheroids (untreated, 100μM and 2.5mM AA) using methods from **section 2.5.1**, two-way mixed effects model, with Geisser-Greenhouse correction revealed that only time had a significant effect in percentage change of spheroid area ($p<0.05$) in comparison to the AA treatment having a significant influence on the spheroid area ($p>0.05$). Both AA physiological and supraphysiological doses of AA did not portray a significant effect on the percentage changes in both DAOY and ONS-76 spheroid area (**figure 5.2**).

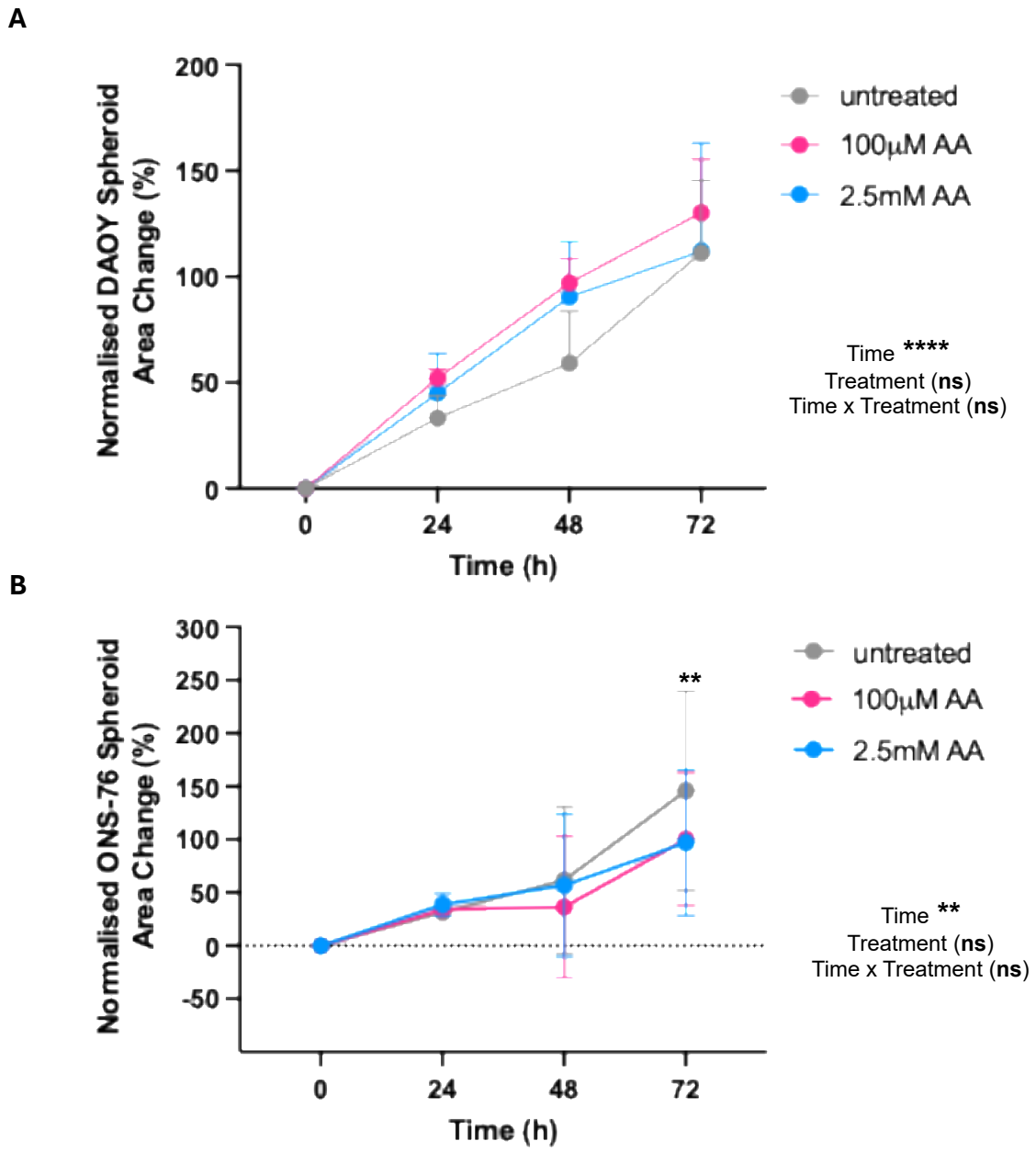

Figure 5.2 DAOY and ONS-76 spheroid growth post treatment of physiological (100µM) AA and supraphysiological (2.5mM) AA. Figure shows the percentage change in area for DAOY spheroids (**A**), and ONS-76 spheroids (**B**) treated with 100µM and 2.5mM doses of AA over a time course (0, 24, 48 and 72 h). Spheroid areas were normalised to that of pre-treatment (0 h). Data represents the mean ± SD (error bars); n=3 with 3 internal replicates per experiment. Untreated control - grey; 100µM AA - pink; 2.5mM AA - blue. A mixed-effects model with treatment and time as fixed effects and Geisser-Greenhouse correction (DAOY epsilon = 0.39; ONS-76 epsilon = 0.38) for sphericity variation and Tukey's multiple comparison test was used for statistical analysis. For DAOY spheroids (**A**) there was no statistically significant treatment effect (*p>0.05, p=0.47 (ns)*) or time and treatment interaction (*p>0.05, p=0.53 (ns)*). Time alone was found to have a substantial influence (*p<0.05, p<0.0001(****)*) on spheroid growth. For ONS-76 spheroids (**B**) there was no statistically significant treatment effect (*p>0.05, p=0.85 (ns)*) or time and treatment interaction (*p>0.05, p=0.87 (ns)*). Time alone was found to have a substantial influence (*p<0.05, p=0.0095 (**)*) on spheroid growth. Any non-significant pairwise comparisons not shown.

DAOY and ONS-76 spheroids were treated with cisplatin either alone or in combination with 100μM or 2.5mM AA (**figure 5.3**). Spheroids decreased in size as there was subsequent disintegration of the spheroid, qualitatively observed in **figure 5.1**. This is expected as spheroids are being treated with a chemotherapeutic agent that actions to decrease spheroid viability (**figure 5.4** and **figure 5.5**). DAOY cells, which are generated from a desmoplastic/nodular tumour, are known to have higher baseline proliferative capability and genetic instability. As briefly discussed before, the key factor that differentiates the cell lines from each other are its *TP53* status (DAOY = mutant, ONS-76 = wild-type) making DAOY cells comparatively more resilient to oxidative stress and cisplatin-induced apoptosis than ONS-76 cells, which exhibit stronger p53 activity and a more robust DNA damage response (Kool et al., 2012, Roper et al., 2021).

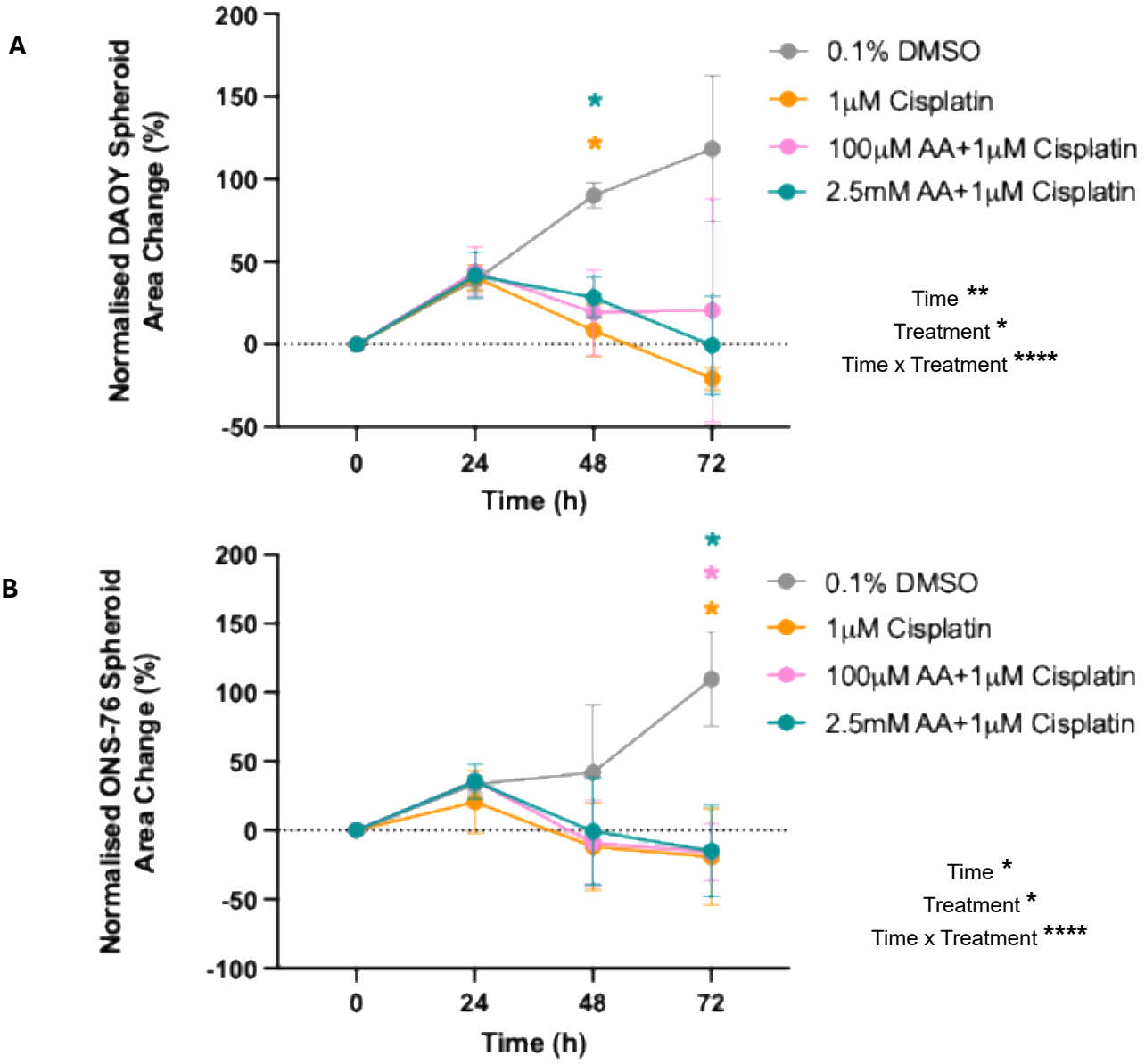

Figure 5.3 DAOY and ONS-76 spheroid growth post treatment with cisplatin alone and in combination with physiological (100μM) AA and supraphysiological (2.5mM) AA. Figure shows the percentage change in area for DAOY spheroids (**A**), and ONS-76 spheroids (**B**) treated with 1μM cisplatin alone or

as co-treatment with 100μM AA and 2.5mM AA over a time course (0, 24, 48 and 72 h). Spheroid areas were normalised to that of pre-treatment (0 h). Data represents the mean ± SD (error bars); n=3 with 3 internal replicates per experiment. 0.1% DMSO control - grey; 1μM cisplatin – orange; 100μM AA + 1μM cisplatin - pink; 2.5mM AA + 1μM cisplatin - teal. A mixed-effects model with treatment and time as fixed effects and Geisser-Greenhouse correction (DAOY epsilon = 0.40; ONS-76 epsilon = 0.45) for sphericity variation and Tukey's multiple comparison test was used for statistical analysis. For DAOY spheroids (**A**) time alone was found to have a significant effect on spheroid growth (*p<0.05, p=0.0086 (***)). Treatment alone (*p<0.05, p=0.014 (**)*) had a significant effect on spheroid growth. There was a substantial significant effect of time and treatment interaction on spheroid growth (*p<0.05, p<0.0001 (****)*). For ONS-76 spheroids (**B**) time alone also had a significant effect on area (*p<0.05, p=0.026 (**)*). Treatment alone also had effect on ONS-76 spheroid area (*p<0.05, p=0.049 (**)*). The interaction between time and treatment on ONS-76 spheroid area was also significant (*p<0.05, p<0.0001 (****)*). Tukey's multiple comparison test revealed significant difference in DAOY spheroid area between control group (0.1% DMSO) and 1μM cisplatin treatment groups at 48 h timepoint (shown by orange asterisk, *p<0.05, p=0.014*) and between control group and 2.5mM AA + 1μM cisplatin treatment group at 48h timepoint (shown by teal asterisk, *p<0.05, p=0.011*) (**A**). Tukey's multiple comparison test ran on ONS-76 spheroid area revealed significant difference in spheroid area between control group and 1μM cisplatin (orange asterisk, *p<0.05, p=0.034*), 100μM AA + 1μM cisplatin (pink asterisk, *p<0.05, p=0.03*) and 2.5mM AA + 1μM cisplatin (teal asterisk, *p<0.05, p=0.036*) treatment group at 72 h timepoint. Any non-significant pairwise comparisons not shown.

5.4 Validation of SHH Spheroid Viability Using Live/Dead Staining

After 72 h of treatment (endpoint), live/dead staining with Calcein AM (CAM) and Propidium Iodide (PI) was carried using exact methods from section 2.6. The live/dead staining was performed to confirm spheroid viability and ascertain if the detached cells seen were viable or dead. Live cells are stained by CAM; CAM is a non-fluorescent stain which is cell permeable and upon entering the cell can be converted to a green, fluorescent stain by the use of enzymes called esterases. PI stains dead cells red and can only enters into cells if they are dead and have a compromised cell membrane. Once inside the cell, PI binds to DNA where it fluoresces as red. As per protocol, untreated spheroid was incubated in 70% EtOH. for 30 min prior to live/dead staining, to ensure the maximum spheroid death to obtain a good dead stain control.

The visible morphological changes were confirmed by live/dead staining, which demonstrated that co-treatment with supraphysiological AA (2.5 mM) and cisplatin resulted in higher red fluorescence and greater spheroid disintegration than cisplatin alone, indicating enhanced cell death. Spheroids treated with physiological AA (100 μM) and cisplatin, on the other hand, showed more intact morphology and brighter green fluorescence, indicating higher spheroid viability. These findings suggest that whereas physiological AA protects against cisplatin toxicity, supraphysiological AA increases cisplatin-induced cytotoxicity (**figure 5.4**).

Untreated, vehicle, and AA-only treated spheroids displayed strong green fluorescence, indicating high viability. Cisplatin-treated spheroids showed increased red fluorescence and spheroid disintegration. Co-treatment with supraphysiological AA (2.5mM) and cisplatin resulted in greater red fluorescence and spheroid disintegration compared to cisplatin alone, suggesting enhanced cytotoxicity, while co-treatment with physiological AA (100µM) preserved spheroid integrity and green fluorescence, indicating a protective effect against cisplatin toxicity.

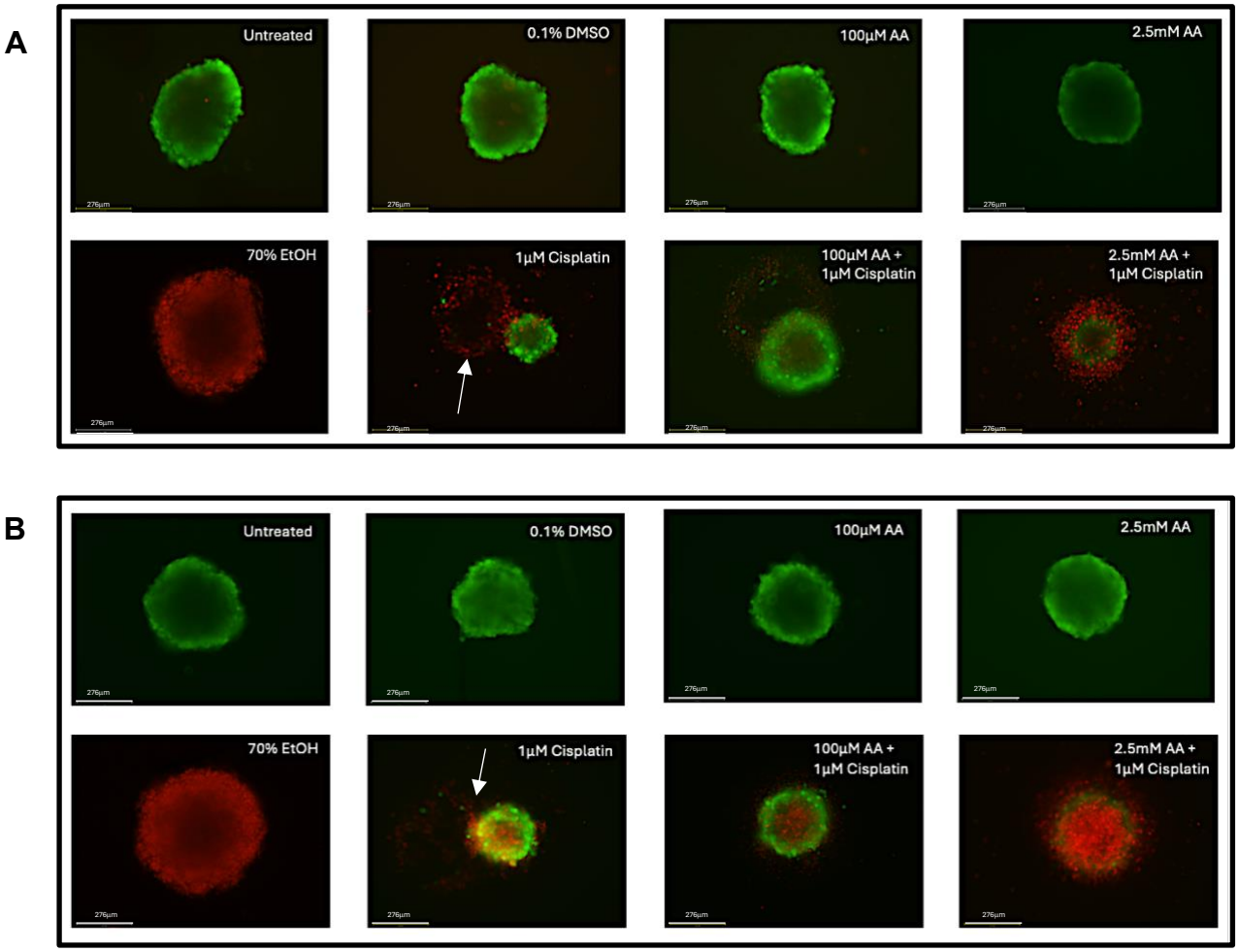

Figure 5.4 Live/dead staining of AA and cisplatin treated DAOY and ONS-76 spheroids. Representative fluorescence images showing DAOY (**A**) and ONS-76 (**B**) spheroids treated with media only (untreated), vehicle control (0.1% DMSO), 100µM AA, 2.5mM AA, cisplatin alone, or cisplatin in combination with 100 µM or 2.5mM AA. Spheroids were stained 72 h post treatment, to validate spheroid morphology change. Spheroids were stained with Calcein AM (CAM) and propidium iodide (PI). CAM stains live cells (green fluorescence) and PI stains dead cells (red fluorescence). Misplacement of dead cells represented by white arrows; due to overlay and not biological error. Scale bar = [276µm].

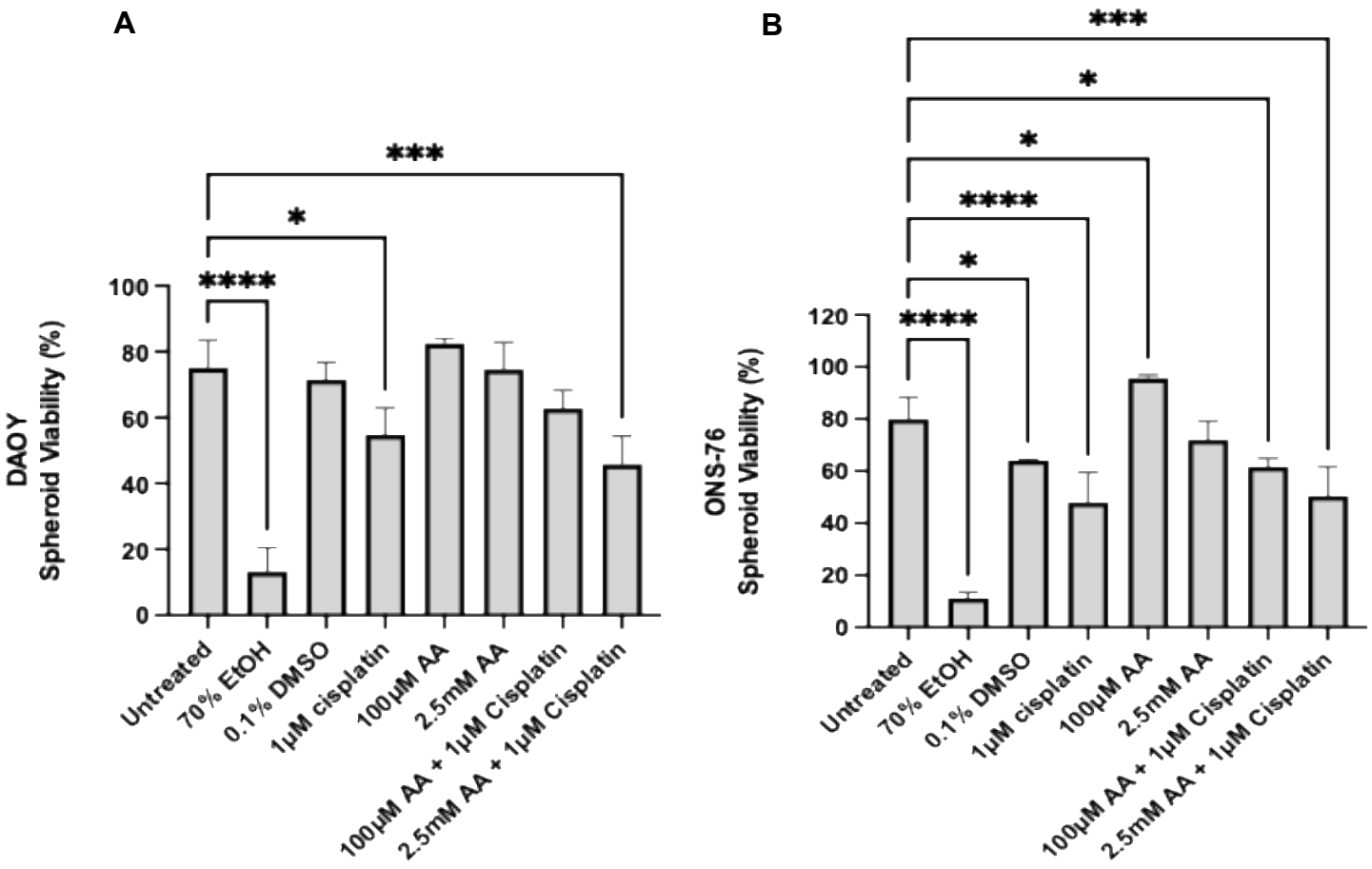

Figure 5.5 Spheroid viability post AA and cisplatin co-treatment. For DAOY (**A**) and ONS-76 (**B**) spheroid viability, the results were normalized to untreated spheroids. The results are given as a mean value of three independent experiments (n=3) ± SD. The integrated densities of each channel; green - live and red - dead were obtained on ImageJ2 software using methods from **section 2.6**. The statistical analysis was performed by the one-way ANOVA, using Dunnett's multiple comparisons tests comparing each treatment group to untreated control (**p<0.05, **p<0.01, ***p<0.001* and *****p<0.0001*.

5.6 Discussion

This chapter examined the influence of physiological and supraphysiological AA concentrations on SHH spheroids' response to chemotherapy.

5.6.1 Cytoprotecting Vs Cytotoxicity

The results potentially display that AA has a dose-dependent dual impact: at physiological concentrations (100 µM), AA may have a cytoprotective effect, while at supraphysiological concentrations (2.5 mM), it can increase the cytotoxicity induced by cisplatin. This dual functionality of AA as an antioxidant at physiological levels but a pro-oxidant at supraphysiological levels is well researched and thus shines a light on studying this dual functionality in cancers for a promising therapeutic outcome (Chen et al., 2005).

The classical approach of AA as an antioxidant, at physiological concentration, is to scavenge ROS and regulate cellular oxidative equilibrium (Padayatty et al., 2003). On the other hand, when coupled with cisplatin, supraphysiological AA (2.5 mM) dramatically accelerated spheroid disintegration and cell death. This finding is confirmed by previous research showing that pharmaceutical or high-dose AA can function as a pro-oxidant by producing hydrogen peroxide and free radicals that are specifically harmful to cancer cells with compromised antioxidant defences (Lim et al., 2016).

Moreover, based on the dynamic nature of chemical interactions, Chemical Dynamic Therapy (CDT) is a revolutionary tumour therapy strategy. Within tumour tissues, CDT produces harmful reactive chemicals through chemical reactions. These chemicals have the ability to cause oxidative reactions inside cells, which can harm proteins and nucleic acids, disrupt cellular homeostasis, and possibly even cause apoptosis. The Fenton reaction and the Haber-Weiss reaction are two chemical processes that are frequently used in CDT. A chemical process called the Fenton reaction, which is usually catalysed by H_2O_2 and transition metal ions like iron ions, creates hydroxyl radicals (Xuan et al., 2020). Conversely, the Fenton reaction is enhanced by the Haber-Weiss reaction. It increases the generation of ROS by converting hydrogen peroxide into superoxide anions and hydroxyl radicals through redox reactions (Guo et al., 2024).

5.6.2 DAOY Vs ONS-76

A biological increase in DAOY spheroid size was observed with treatment of AA. Whereas in ONS-76 spheroids, both doses of AA don't seem to increase spheroid size, and AA treated spheroids remain overall smaller than the untreated. This suggests a cell line specific growth-promoting effect of AA. This observation may be indicative of the key cell line specific difference which is their *TP53* status. *TP53* is the gene that encodes for the tumour suppressor protein p53. DAOY cell line hold a mutant *TP53*, whereas ONS-76 retains a wild-type *TP53,* resulting in a mutant p53 protein in DAOYs and a normal p53 protein (Bonfim-Silva et al., 2019). This difference in their *TP53* status may contribute to the way each cell line responds to AA (Koo et al., 2025). TP53 encodes p53, a tumour suppressor that controls antioxidant defence, DNA repair, and apoptosis. Wild type p53 can trigger antioxidant genes to buffer ROS, whereas mutant or null TP53 in cells frequently lack these defensive mechanisms (Sablina et al., 2005). High levels of AA produce ROS, resulting in enhanced chemosensitivity. TP53 status may potentially influence changes in response to AA treatments between the two spheroid models (Kaźmierczak-Barańska et al., 2020, Kim et al., 2012).

While DAOY spheroids (*TP53* mutant) showed partial resilience, ONS-76 spheroids (*TP53* wild-type) showed a more noticeable decrease in size and viability. This discrepancy most likely results from redox regulation mediated by p53. By activating genes linked to the oxidative stress response and mitochondrial integrity, wild-type p53 increases ROS-driven apoptosis (Vousden and Prives, 2009). These genotype-specific reactions imply that AA-based adjuvant therapy may be tailored based on the genetic makeup of the tumour. Moreover, AA can be explored in co-treatments with to other therapies besides chemotherapy. A plant-derived SMO (smoothened) inhibitor called cyclopamine has been shown to supress the SHH signalling pathway

(Chen et al., 2002). Combining this therapy adjuvant with AA may complement one others function of weakening signalling and creating redox imbalances in SHH tumours.

5.6.3 Inhibition of AA/DHA uptake

Furthermore, the pilot study of Inhibiting AA/DHA transport (**Appendix D**), to an extent reveals that the AA's role as an antioxidant and a pro-oxidant are influenced by its intracellular availability. While cytochalasin B, a pan-GLUT inhibitor, and sulfinpyrazone, a non-selective SVCT2 inhibitor, both demonstrated similar general trends in increasing cytotoxicity, their processes operate through different pathways of AA absorption and redox regulation.

While cytochalasin B and sulfinpyrazone both produced similar general patterns, their processes focus on different version of AA uptake and redox balancing pathways. While GLUT transporters, such as GLUT10, promote cellular entry of DHA, which is eventually reduced back to AA intracellularly, SVCT2 facilitates transport of the reduced form, AA (Corti et al., 2010). Inhibition of SVCT2 lowers intracellular AA in turn increases susceptibility to oxidative stress and drug-induced toxicity. On the other hand, inhibiting GLUT-mediated DHA uptake may prevent extracellularly oxidised AA from being recycled, changing extracellular redox conditions instead of intracellular AA.

These findings point to a potential therapeutic duality of AA in the treatment of medulloblastoma: supraphysiological or high-dose AA may act as a redox-sensitizing agent that increases chemotherapy-induced tumour death, while physiological AA may lessen cisplatin toxicity and cytoprotects the tumour. Supraphysiological AA has improved chemotherapeutic efficacy without raising systemic toxicity in additional cancer trials, supporting the wider clinical potential of ascorbate-based redox treatment (Longchar and Prasad, 2015, Stephenson et al., 2013). Using 3D spheroid models that closely mimic the tumour microenvironment (Friedrich et al., 2009), the findings here offer a crucial preclinical basis for developing redox-targeted combination treatments in SHH medulloblastoma.

5.6.1 Limitations

A common limitation with this study is that the clinical significance depends on pharmacological delivery methods like high-dose intravenous infusion because the concentrations of AA used in this investigation might not be easily attained within the tumour microenvironment under typical physiological settings. Additionally, the two cell lines used; DAOY and ONS-76 represent a limited genetic heterogeneity typical in SHH medulloblastoma, albeit providing a helpful comparison in TP53 status. The generalisability of these results across the larger SHH subgroup, which includes cancers with a variety of driver mutations, such as PTCH1, SUFU, and SMO, is limited by conclusions derived from two cell lines. Furthermore, the transporter inhibition data in Appendix D is pilot in nature, and the off-target effects of cytochalasin B and sulfinpyrazone, which are pan-GLUT and non-selective SVCT2 inhibitors, respectively, raise the risk of misinterpreting AA uptake and redox regulation mechanisms.

5.6.2 Future Work

Future research for this investigation should build on these findings by examining a wider variety of SHH medulloblastoma cell lines, especially those carrying PTCH1 and SUFU mutations to determine whether the same effect of AA is seen across the molecular diversity of other medulloblastoma subgroup (Kool et al., 2012, Northcott et al., 2012). To strengthen the validation of AA's cytoprotective and pro-oxidant properties, conducting molecular assays such as intracellular ROS quantification or western blotting for appropriate apoptotic markers may be of good practice (Trachootham et al., 2009, Traverso et al., 2013).

More selective inhibitors should be used to expand the pilot transporter inhibition study shown in **Appendix D** to gain a better understanding of how individual AA transport routes contribute to intracellular redox control. Although useful, the present usage of sulfinpyrazone and cytochalasin B poses a significant risk of off-target effects due to their non-selective and pan-GLUT inhibitory profiles, respectively, which complicates mechanistic interpretation. The relative contribution of the oxidised AA recycling pathway to intracellular redox balance might also be clarified by selectively knocking down SVCT and GLUT transporters in SHH medulloblastoma cell lines (Kwon et al., 2007). A clearer mechanistic connection between transporter activity, intracellular AA availability, and chemosensitivity in SHH medulloblastoma cells might be established by combining these knockdown techniques with direct intracellular AA quantification methods explored by Vislisel et al. (2007).

Furthermore, future expansion of this investigation can examine methods that directly regulate intracellular DHA concentrations instead of depending only on extracellular AA and DHA supplementation to modify intracellular redox state. Due to its dependence on GLUT transporter expression levels, extracellular pH, and the oxidative state of the tumour microenvironment, all of which can vary the uptake of extracellular AA/DHA (May et al., 1999, Rumsey et al., 1997). Instead, intracellular DHA accumulation can be controlled by blocking the enzymatic recycling of DHA back to AA, especially by focusing on the thioredoxin reductase systems that oversee intracellular DHA reduction (Wells et al., 1990). It would be anticipated that allowing DHA to build up inside cells without being recycled would reduce intracellular AA, change the redox balance in favour of oxidative stress, and possibly make cancer cells more susceptible to chemotherapy without the need for external AA administration.

Chapter 6: Conclusion

This study investigated the relationship between AA, its transporters and the ECM deposition in SHH spheroid models. The multi-functionality of AA as a co-factor in collagen synthesis, as an antioxidant and a pro-oxidant, this project aimed to explore form a bridge between collagen, AA and SHH medulloblastoma to make positive therapeutic revolutions at the same time bettering patient prognosis.

Previously conducted bioinformatic analyses on SHH patient derived data revealed high expression of SVCT2 correlated with poorest survival outcomes in patients were as high expression of GLUT10 correlated with best survival outcomes, compared to other AA and DHA transporters. These findings influenced the idea that expression of AA and DHA transporters may influence the way SHH tumours behave, metabolises and respond to treatment. Elaborating on this, this project aimed to understand the baseline expression of these transporters in SHH tumour models. Using qRT-PCT methods, demonstrated a level of difference of transporter expression between the two SHH cell lines DAOY and ONS-76. Despite no statistical difference, a general trend between SVCT2 expression in DAOY and ONS-76 was seen, where DAOY cells presented a higher expression of SVCT2 than ONS-76.

Spheroids treated with AA at physiological (100μM) and supraphysiological (2.5mM) concentrations, alone or in combination with cisplatin, showed unique redox-dependent effects. Physiological AA maintained spheroid morphology and viability, implying a cytoprotective and potentially a tumour-favourable effect. In contrast, supraphysiological AA dramatically enhanced cisplatin induced cytotoxicity, resulting in spheroid disintegration and increased cell death. A characteristic which is widely consistent with its pro-oxidant activity at the pharmacological level.

Immunofluorescence labelling of spheroids revealed that collagen concentrated mostly at the outer matrix border, generating a dense ECM shell, but laminin distribution was less defined. Although the data are qualitative, they imply that AA may impact ECM structure, which supports earlier evidence that collagen enrichment is a distinguishing hallmark of SHH tumours.

Inhibition experiments revealed additional mechanistic insights into transporter involvement. Sulfinpyrazone inhibited SVCT2 and impaired spheroid cohesiveness and survivability under physiological AA treatments, demonstrating that SVCT2-mediated AA uptake is required for intracellular redox homeostasis. In contrast, inhibiting GLUT-mediated DHA uptake with cytochalasin B altered spheroid morphology and increased cytotoxic responses in supraphysiological AA conditions, demonstrating the relevance of GLUT-mediated redox cycling under oxidative stress.

Overall, these findings build a foundation in suggesting that AA can play two roles in SHH medulloblastoma, depending on its concentration. Physiological AA promotes redox stability within the SHH tumour models whereas supraphysiological AA improves chemotherapeutic efficiency via oxidative processes that may be influenced by changing transporter function. This study highlights the important relationship between AA metabolism, transporter expression, and tumour microenvironment structure, providing mechanistic insight into how AA supplementation might be optimised as an adjuvant strategy in SHH medulloblastoma therapy.

REFERENCES

ABIRI, B. & VAFA, M. 2021. Vitamin C and Cancer: The Role of Vitamin C in Disease Progression and Quality of Life in Cancer Patients. *Nutrition and Cancer-an International Journal,* 73**,** 1282-1292.

ANDREAS RAABE , K. L., THOMAS PETUTSCHNIGG. 2025. *Medulloblastoma* [Online]. Neurosurgery Inselspital Bern: Univeristy of Bern. Available: https://neurochirurgie.insel.ch/erkrankungen-spezialgebiete/hirntumoren/medulloblastom [Accessed 09/01/2025 2025].

ANONYMOUS. 2024. *Medulloblastoma: Diagnosis and Treatment* [Online]. National Cancer Institute. Available: https://www.cancer.gov/rare-brain-spine-tumor/tumors/medulloblastoma [Accessed 09/01/2025 2025].

ARNOLD, S. A., RIVERA, L. B., MILLER, A. F., CARBON, J. G., DINEEN, S. P., XIE, Y., CASTRILLON, D. H., SAGE, E. H., PUOLAKKAINEN, P., BRADSHAW, A. D. & BREKKEN, R. A. 2010. Lack of host SPARC enhances vascular function and tumor spread in an orthotopic murine model of pancreatic carcinoma. *Disease Models & Mechanisms,* 3**,** 57-72.

BAI, R. Y., STAEDTKE, V., LIDOV, H. G., EBERHART, C. G. & RIGGINS, G. J. 2012. OTX2 Represses Myogenic and Neuronal Differentiation in Medulloblastoma Cells. *Cancer Research,* 72**,** 5988-6001.

BIELSKI, B. H. J., ALLEN, A. O. & SCHWARZ, H. A. 1981. MECHANISM OF DISPROPORTIONATION OF ASCORBATE RADICALS. *Journal of the American Chemical Society,* 103**,** 3516-3518.

BONFIM-SILVA, R., SALOMãO, K. B., PIMENTEL, T., MENEZES, C., PALMA, P. V. B. & FONTES, A. M. 2019. Biological characterization of the UW402, UW473, ONS-76 and DAOY pediatric medulloblastoma cell lines. *Cytotechnology,* 71**,** 893-903.

BOOT-HANDFORD, R. P. & TUCKWELL, D. S. 2003. Fibrillar collagen: the key to vertebrate evolution? A tale of molecular incest. *Bioessays,* 25**,** 142-151.

BRODSKY, B. & PERSIKOV, A. V. 2005. Molecular structure of the collagen triple helix. *In:* PARRY, D. A. D. & SQUIRE, J. M. (eds.) *Fibrous Proteins: Coiled-Coils, Collagen and Elastomers*. San Diego: Elsevier Academic Press Inc.

BRUGIèRES, L., PIERRON, G., CHOMPRET, A., BRESSAC-DE PAILLERETS, B., DI ROCCO, F., VARLET, P., PIERRE-KAHN, A., CARON, O., GRILL, J. & DELATTRE, O. 2010. Incomplete penetrance of the predisposition to medulloblastoma associated with germ-line SUFU mutations. *Journal of Medical Genetics,* 47**,** 142-144.

BUETTNER, G. R. & JURKIEWICZ, B. A. 1996. Catalytic metals, ascorbate and free radicals: Combinations to avoid. *Radiation Research,* 145**,** 532-541.

BüHRING, U., STRAYLE-BATRA, M., FREUDENSTEIN, D., SCHEEL-WALTER, H. G. & KüKER, W. 2002. MRI features of primary, secondary and metastatic medulloblastoma. *European Radiology,* 12**,** 1342-1348.

BURGESS, E. R., PRADITI, C., PHILLIPS, E., VISSERS, M. C. M., ROBINSON, B. A., DACHS, G. U. & WIGGINS, G. A. R. 2025. Role of Sodium-Dependent Vitamin C Transporter-2 and Ascorbate in Regulating the Hypoxic Pathway in Cultured Glioblastoma Cells. *Journal of Cellular Biochemistry,* 126**,** 16.

CALCUTT, G. 1951. THE FORMATION OF HYDROGEN PEROXIDE DURING THE AUTOXIDATION OF ASCORBIC ACID. *Experientia,* 7**,** 26-26.

CAMARENA, V. & WANG, G. F. 2016. The epigenetic role of vitamin C in health and disease. *Cellular and Molecular Life Sciences,* 73**,** 1645-1658.

CAMERON, E. & PAULING, L. 1976. Supplemental ascorbate in the supportive treatment of cancer: Prolongation of survival times in terminal human cancer. *Proc Natl Acad Sci U S A,* 73**,** 3685-9.

CAMPBELL, E. J., VISSERS, M. C. M., BOZONET, S., DYER, A., ROBINSON, B. A. & DACHS, G. U. 2015. Restoring physiological levels of ascorbate slows tumor growth and moderates HIF-1 pathway activity in Gulo -/- mice. *Cancer Medicine,* 4**,** 303-314.

CARMINE, T. C., EVANS, P., BRUCHELT, G., EVANS, R., HANDGRETINGER, R., NIETHAMMER, D. & HALLIWELL, B. 1995. PRESENCE OF IRON CATALYTIC FOR FREE-RADICAL REACTIONS IN PATIENTS UNDERGOING CHEMOTHERAPY - IMPLICATIONS FOR THERAPEUTIC MANAGEMENT. *Cancer Letters,* 94**,** 219-226.

CARR, A. & FREI, B. 1999. Does vitamin C act as a pro-oxidant under physiological conditions? *Faseb j,* 13**,** 1007-24.

CAVALLI, F. M. G., REMKE, M., RAMPASEK, L., PEACOCK, J., SHIH, D. J. H., LUU, B., GARZIA, L., TORCHIA, J., NOR, C., MORRISSY, A. S., AGNIHOTRI, S., THOMPSON, Y. Y., KUZAN-FISCHER, C. M., FAROOQ, H., ISAEV, K., DANIELS, C., CHO, B. K., KIM, S. K., WANG, K. C., LEE, J. Y., GRAJKOWSKA, W. A., PEREK-POLNIK, M., VASILJEVIC, A., FAURE-CONTER, C., JOUVET, A., GIANNINI, C., RAO, A. A. N., LI, K. K. W., NG, H. K., EBERHART, C. G., POLLACK, I. F., HAMILTON, R. L., GILLESPIE, G. Y., OLSON, J. M., LEARY, S., WEISS, W. A., LACH, B., CHAMBLESS, L. B., THOMPSON, R. C., COOPER, M. K., VIBHAKAR, R., HAUSER, P., VAN VEELEN, M. L. C., KROS, J. M., FRENCH, P. J., RA, Y. S., KUMABE, T., LóPEZ-AGUILAR, E., ZITTERBART, K., STERBA, J., FINOCCHIARO, G., MASSIMINO, M., VAN MEIR, E. G., OSUKA, S., SHOFUDA, T., KLEKNER, A., ZOLLO, M., LEONARD, J. R., RUBIN, J. B., JABADO, N., ALBRECHT, S., MORA, J., VAN METER, T. E., JUNG, S., MOORE, A. S., HALLAHAN, A. R., CHAN, J. A., TIRAPELLI, D. P. C., CARLOTTI, C. G., FOULADI, M., PIMENTEL, J., FARIA, C. C., SAAD, A. G., MASSIMI, L., LIAU, L. M., WHEELER, H., NAKAMURA, H., ELBABAA, S. K., PEREZPENA-DIAZCONTI, M., DE LEON, F. C. P., ROBINSON, S., ZAPOTOCKY, M., LASSALETTA, A., HUANG, A., HAWKINS, C. E., TABORI, U., BOUFFET, E., BARTELS, U., DIRKS, P. B., RUTKA, J. T., BADER, G. D., REIMAND, J., GOLDENBERG, A., RAMASWAMY, V. & TAYLOR, M. D. 2017. Intertumoral Heterogeneity within Medulloblastoma Subgroups. *Cancer Cell,* 31**,** 737-+.

CHEN, J. K., TAIPALE, J., COOPER, M. K. & BEACHY, P. A. 2002. Inhibition of Hedgehog signaling by direct binding of cyclopamine to Smoothened. *Genes & Development,* 16**,** 2743-2748.

CHEN, Q., ESPEY, M. G., KRISHNA, M. C., MITCHELL, J. B., CORPE, C. P., BUETTNER, G. R., SHACTER, E. & LEVINE, M. 2005. Pharmacologic ascorbic acid concentrations selectively kill cancer cells: Action as a pro-drug to deliver hydrogen peroxide to tissues. *Proceedings of the National Academy of Sciences of the United States of America,* 102**,** 13604-13609.

CHEN, Q., ESPEY, M. G., SUN, A. Y., POOPUT, C., KIRK, K. L., KRISHNA, M. C., KHOSH, D. S., DRISKO, J. & LEVINE, M. 2008. Pharmacologic doses of ascorbate act as a prooxidant and decrease growth of aggressive tumor xenografts in mice.

Proceedings of the National Academy of Sciences of the United States of America, 105**,** 11105-11109.

CHO, Y. J., TSHERNIAK, A., TAMAYO, P., SANTAGATA, S., LIGON, A., GREULICH, H., BERHOUKIM, R., AMANI, V., GOUMNEROVA, L., EBERHART, C. G., LAU, C. C., OLSON, J. M., GILBERTSON, R. J., GAJJAR, A., DELATTRE, O., KOOL, M., LIGON, K., MEYERSON, M., MESIROV, J. P. & POMEROY, S. L. 2011. Integrative Genomic Analysis of Medulloblastoma Identifies a Molecular Subgroup That Drives Poor Clinical Outcome. *Journal of Clinical Oncology,* 29**,** 1424-1430.

CIUCCI, A., MECO, D., DE STEFANO, I., TRAVAGLIA, D., ZANNONI, G. F., SCAMBIA, G., RICCARDI, R., SARAN, A., MANCUSO, M. & GALLO, D. 2014. Gender Effect in Experimental Models of Human Medulloblastoma: Does the Estrogen Receptor β Signaling Play a Role? *Plos One,* 9**,** 12.

CORTI, A., CASINI, A. F. & POMPELLA, A. 2010. Cellular pathways for transport and efflux of ascorbate and dehydroascorbate. *Archives of Biochemistry and Biophysics,* 500**,** 107-115.

CREAGAN, E. T., MOERTEL, C. G., OFALLON, J. R., SCHUTT, A. J., OCONNELL, M. J., RUBIN, J. & FRYTAK, S. 1979. FAILURE OF HIGH-DOSE VITAMIN-C (ASCORBIC-ACID) THERAPY TO BENEFIT PATIENTS WITH ADVANCED CANCER - CONTROLLED TRIAL. *New England Journal of Medicine,* 301**,** 687-690.

CRUCIAT, C. M. & NIEHRS, C. 2013. Secreted and transmembrane wnt inhibitors and activators. *Cold Spring Harb Perspect Biol,* 5**,** a015081.

DANGOULOFF-ROS, V., VARLET, P., LEVY, R., BECCARIA, K., PUGET, S., DUFOUR, C. & BODDAERT, N. 2021. Imaging features of medulloblastoma: Conventional imaging, diffusion-weighted imaging, perfusion-weighted imaging, and spectroscopy: From general features to subtypes and characteristics. *Neurochirurgie,* 67**,** 6-13.

DäSTER, S., AMATRUDA, N., CALABRESE, D., IVANEK, R., TURRINI, E., DROESER, R. A., ZAJAC, P., FIMOGNARI, C., SPAGNOLI, G. C., IEZZI, G., MELE, V. & MURARO, M. G. 2017. Induction of hypoxia and necrosis in multicellular tumor spheroids is associated with resistance to chemotherapy treatment. *Oncotarget,* 8**,** 1725-1736.

DOMOGATSKAYA, A., RODIN, S. & TRYGGVASON, K. 2012a. Functional diversity of laminins. *Annu Rev Cell Dev Biol,* 28**,** 523-53.

DOMOGATSKAYA, A., RODIN, S. & TRYGGVASON, K. 2012b. Functional Diversity of Laminins. *In:* SCHEKMAN, R. (ed.) *Annual Review of Cell and Developmental Biology, Vol 28*. Palo Alto: Annual Reviews.

DRISKO, J. A., CHAPMAN, J. & HUNTER, V. J. 2003. The use of antioxidants with first-line chemotherapy in two cases of ovarian cancer. *Journal of the American College of Nutrition,* 22**,** 118-123.

DU, J., CULLEN, J. J. & BUETTNER, G. R. 2012a. Ascorbic acid: Chemistry, biology and the treatment of cancer. *Biochimica Et Biophysica Acta-Reviews on Cancer,* 1826**,** 443-457.

DU, J., CULLEN, J. J. & BUETTNER, G. R. 2012b. Ascorbic acid: chemistry, biology and the treatment of cancer. *Biochim Biophys Acta,* 1826**,** 443-57.

DUFFNER, P. K., COHEN, M. E., MYERS, M. H. & HEISE, H. W. 1986. SURVIVAL OF CHILDREN WITH BRAIN-TUMORS - SEER PROGRAM, 1973-1980. *Neurology,* 36**,** 597-601.

DUSTIN, M. L. & DE FOUGEROLLES, A. R. 2001. Reprograming T cells: the role of extracellular matrix in coordination of T cell activation and migration. *Current Opinion in Immunology,* 13**,** 286-290.

EGEBLAD, M., RASCH, M. G. & WEAVER, V. M. 2010. Dynamic interplay between the collagen scaffold and tumor evolution. *Current Opinion in Cell Biology,* 22**,** 697-706.

ELLISON, D. W., ONILUDE, O. E., LINDSEY, J. C., LUSHER, M. E., WESTON, C. L., TAYLOR, R. E., PEARSON, A. D. & CLIFFORD, S. C. 2005. β-catenin status predicts a favorable outcome in childhood medulloblastoma: The United Kingdom Children's Cancer Study Group Brain Tumour Committee. *Journal of Clinical Oncology,* 23**,** 7951-7957.

ESPEY, M. G., CHEN, P., CHALMERS, B., DRISKO, J., SUN, A. Y., LEVINE, M. & CHEN, Q. 2011. Pharmacologic ascorbate synergizes with gemcitabine in preclinical models of pancreatic cancer. *Free Radic Biol Med,* 50**,** 1610-9.

FLOREA, A. M. & BüSSELBERG, D. 2011. Cisplatin as an anti-tumor drug: cellular mechanisms of activity, drug resistance and induced side effects. *Cancers (Basel),* 3**,** 1351-71.

FORASTIERE, A. A. 1994. Overview of platinum chemotherapy in head and neck cancer. *Semin Oncol,* 21**,** 20-7.

FRANTZ, C., STEWART, K. M. & WEAVER, V. M. 2010a. The extracellular matrix at a glance. *J Cell Sci,* 123**,** 4195-200.

FRANTZ, C., STEWART, K. M. & WEAVER, V. M. 2010b. The extracellular matrix at a glance. *Journal of Cell Science,* 123**,** 4195-4200.

FRIEDRICH, J., SEIDEL, C., EBNER, R. & KUNZ-SCHUGHART, L. A. 2009. Spheroid-based drug screen: considerations and practical approach. *Nat Protoc,* 4**,** 309-24.

GAJJAR, A., CHINTAGUMPALA, M., ASHLEY, D., KELLIE, S., KUN, L. E., MERCHANT, T. E., WOO, S., WHEELER, G., AHERN, V., KRASIN, M. J., FOULADI, M., BRONISCER, A., KRANCE, R., HALE, G. A., STEWART, C. F., DAUSER, R., SANFORD, R. A., FULLER, C., LAU, C., BOYETT, J. M., WALLACE, D. & GILBERTSON, R. J. 2006a. Risk-adapted craniospinal radiotherapy followed by high-dose chemotherapy and stem-cell rescue in children with newly diagnosed medulloblastoma (St Jude Medulloblastoma-96): long-term results from a prospective, multicentre trial. *Lancet Oncology,* 7**,** 813-820.

GAJJAR, A., CHINTAGUMPALA, M., ASHLEY, D., KELLIE, S., KUN, L. E., MERCHANT, T. E., WOO, S., WHEELER, G., AHERN, V., KRASIN, M. J., FOULADI, M., BRONISCER, A., KRANCE, R., HALE, G. A., STEWART, C. F., DAUSER, R., SANFORD, R. A., FULLER, C., LAU, C., BOYETT, J. M., WALLACE, D. & GILBERTSON, R. J. 2006b. Risk-adapted craniospinal radiotherapy followed by high-dose chemotherapy and stem-cell rescue in children with newly diagnosed medulloblastoma (St Jude Medulloblastoma-96): long-term results from a prospective, multicentre trial. *Lancet Oncol,* 7**,** 813-20.

GAJJAR, A., PFISTER, S. M., TAYLOR, M. D. & GILBERTSON, R. J. 2014. Molecular Insights into Pediatric Brain Tumors Have the Potential to Transform Therapy. *Clinical Cancer Research,* 20**,** 5630-5640.

GAJJAR, A., ROBINSON, G. W., SMITH, K. S., LIN, T., MERCHANT, T. E., CHINTAGUMPALA, M., MAHAJAN, A., SU, J., BOUFFET, E., BARTELS, U., SCHECHTER, T., HASSALL, T., ROBERTSON, T., NICHOLLS, W., GURURANGAN,

S., SCHROEDER, K., SULLIVAN, M., WHEELER, G., HANSFORD, J. R., KELLIE, S. J., MCCOWAGE, G., COHN, R., FISHER, M. J., KRASIN, M. J., STEWART, C. F., BRONISCER, A., BUCHHALTER, I., TATEVOSSIAN, R. G., ORR, B. A., NEALE, G., KLIMO, P., JR., BOOP, F., SRINIVASAN, A., PFISTER, S. M., GILBERTSON, R. J., ONAR-THOMAS, A., ELLISON, D. W. & NORTHCOTT, P. A. 2021. Outcomes by Clinical and Molecular Features in Children With Medulloblastoma Treated With Risk-Adapted Therapy: Results of an International Phase III Trial (SJMB03). *J Clin Oncol,* 39**,** 822-835.

GELSE, K., PöSCHL, E. & AIGNER, T. 2003. Collagens -: structure, function, and biosynthesis. *Advanced Drug Delivery Reviews,* 55**,** 1531-1546.

GHAVAMI, G. & SARDARI, S. 2020. Synergistic Effect of Vitamin C with Cisplatin for Inhibiting Proliferation of Gastric Cancer Cells. *Iran Biomed J,* 24**,** 119-27.

GIBSON, P., TONG, Y. A., ROBINSON, G., THOMPSON, M. C., CURRLE, D. S., EDEN, C., KRANENBURG, T. A., HOGG, T., POPPLETON, H., MARTIN, J., FINKELSTEIN, D., POUNDS, S., WEISS, A., PATAY, Z., SCOGGINS, M., OGG, R., PEI, Y. X., YANG, Z. J., BRUN, S., LEE, Y., ZINDY, F., LINDSEY, J. C., TAKETO, M. M., BOOP, F. A., SANFORD, R. A., GAJJAR, A., CLIFFORD, S. C., ROUSSEL, M. F., MCKINNON, P. J., GUTMANN, D. H., ELLISON, D. W., WECHSLER-REYA, R. & GILBERTSON, R. J. 2010. Subtypes of medulloblastoma have distinct developmental origins. *Nature,* 468**,** 1095-1099.

GILBERTSON, R. J. 2004. Medulloblastoma: signalling a change in treatment. *Lancet Oncology,* 5**,** 209-218.

GILKES, D. M., SEMENZA, G. L. & WIRTZ, D. 2014. Hypoxia and the extracellular matrix: drivers of tumour metastasis. *Nature Reviews Cancer,* 14**,** 430-439.

GIRIGOSWAMI, K., SAINI, D. & GIRIGOSWAMI, A. 2021. Extracellular Matrix Remodeling and Development of Cancer. *Stem Cell Rev Rep,* 17**,** 739-747.

GODWIN, A. K., MEISTER, A., O'DWYER, P. J., HUANG, C. S., HAMILTON, T. C. & ANDERSON, M. E. 1992. High resistance to cisplatin in human ovarian cancer cell lines is associated with marked increase of glutathione synthesis. *Proc Natl Acad Sci U S A,* 89**,** 3070-4.

GORRES, K. L. & RAINES, R. T. 2010. Prolyl 4-hydroxylase. *Crit Rev Biochem Mol Biol,* 45**,** 106-24.

GRAUMLICH, J. F., LUDDEN, T. M., CONRYCANTILENA, C., CANTILENA, L. R., WANG, Y. H. & LEVINE, M. 1997. Pharmacokinetic model of ascorbic acid in healthy male volunteers during depletion and repletion. *Pharmaceutical Research,* 14**,** 1133-1139.

GUO, D., LIAO, Y., NA, J. T., WU, L. L., YIN, Y., MI, Z. C., FANG, S. X., LIU, X. Y. & HUANG, Y. 2024. The Involvement of Ascorbic Acid in Cancer Treatment. *Molecules,* 29**,** 20.

GURNEY, J. G. & KADAN-LOTTICK, N. 2001. Brain and other central nervous system tumors: rates, trends, and epidemiology. *Current Opinion in Oncology,* 13**,** 160-166.

HATTEN, M. E. & ROUSSEL, M. F. 2011. Development and cancer of the cerebellum. *Trends in Neurosciences,* 34**,** 134-142.

HENDRIKSE, L. D., HALDIPUR, P., SAULNIER, O., MILLMAN, J., SJOBOEN, A. H., ERICKSON, A. W., ONG, W., GORDON, V., COUDIèRE-MORRISON, L., MERCIER, A. L., SHOKOUHIAN, M., SUáREZ, R. A., LY, M., BORLASE, S., SCOTT, D. S., VLADOIU, M. C., FAROOQ, H., SIRBU, O., NAKASHIMA, T., NAMBU, S.,

FUNAKOSHI, Y., BAHCHELI, A., DIAZ-MEJIA, J. J., GOLSER, J., BACH, K., PHUONG-BAO, T., SKOWRON, P., WANG, E. Y., KUMAR, S. A., BALIN, P., VISVANATHAN, A., LEE, J. J. Y., AYOUB, R., CHEN, X., CHEN, X., MUNGALL, K. L., LUU, B., BéRUBé, P., WANG, Y. C., PFISTER, S. M., KIM, S.-K., DELATTRE, O., BOURDEAUT, F., DOZ, F., MASLIAH-PLANCHON, J., GRAJKOWSKA, W. A., LOUKIDES, J., DIRKS, P., FèVRE-MONTANGE, M., JOUVET, A., FRENCH, P. J., KROS, J. M., ZITTERBART, K., BAILEY, S. D., EBERHART, C. G., RAO, A. A. N., GIANNINI, C., OLSON, J. M., GARAMI, M., HAUSER, P., PHILLIPS, J. J., RA, Y. S., DE TORRES, C., MORA, J., LI, K. K. W., NG, H.-K., POON, W. S., POLLACK, I. F., LóPEZ-AGUILAR, E., GILLESPIE, G. Y., VAN METER, T. E., SHOFUDA, T., VIBHAKAR, R., THOMPSON, R. C., COOPER, M. K., RUBIN, J. B., KUMABE, T., JUNG, S., LACH, B., IOLASCON, A., FERRUCCI, V., DE ANTONELLIS, P., ZOLLO, M., CINALLI, G., ROBINSON, S., STEARNS, D. S., VAN MEIR, E. G., PORRATI, P., FINOCCHIARO, G., MASSIMINO, M., CARLOTTI, C. G., FARIA, C. C., ROUSSEL, M. F., BOOP, F., CHAN, J. A., ALDINGER, K. A., RAZAVI, F., SILVESTRI, E., MCLENDON, R. E., THOMPSON, E. M., et al. 2022. Failure of human rhombic lip differentiation underlies medulloblastoma formation. *Nature,* 609**,** 1021-1028.

HIRSCHHAEUSER, F., MENNE, H., DITTFELD, C., WEST, J., MUELLER-KLIESER, W. & KUNZ-SCHUGHART, L. A. 2010. Multicellular tumor spheroids: An underestimated tool is catching up again. *Journal of Biotechnology,* 148**,** 3-15.

HOLMAN, G. D. 2020. Structure, function and regulation of mammalian glucose transporters of the SLC2 family. *Pflugers Archiv-European Journal of Physiology,* 472**,** 1155-1175.

HOSOYA, K., MINAMIZONO, A., KATAYAMA, K., TERASAKI, T. & TOMI, M. 2004. Vitamin C transport in oxidized form across the rat blood-retinal barrier. *Investigative Ophthalmology & Visual Science,* 45**,** 1232-1239.

INGHAM, P. W. & MCMAHON, A. P. 2001. Hedgehog signaling in animal development: paradigms and principles. *Genes & Development,* 15**,** 3059-3087.

JACKSON, K. & PACKER, R. J. 2023. Recent Advances in Pediatric Medulloblastoma. *Current Neurology and Neuroscience Reports,* 23**,** 841-848.

JACOBSEN, P. F., JENKYN, D. J. & PAPADIMITRIOU, J. M. 1985. Establishment of a human medulloblastoma cell line and its heterotransplantation into nude mice. *J Neuropathol Exp Neurol,* 44**,** 472-85.

JAEGER, M. D., GHISLENI, E. C., CARDOSO, P. S., SINIGLAGLIA, M., FALCON, T., BRUNETTO, A. T., BRUNETTO, A. L., DE FARIAS, C. B., TAYLOR, M. D., NöR, C., RAMASWAMY, V. & ROESLER, R. 2020. HDAC and MAPK/ERK Inhibitors Cooperate To Reduce Viability and Stemness in Medulloblastoma. *Journal of Molecular Neuroscience,* 70**,** 981-992.

JIANG, J. & HUI, C. C. 2008. Hedgehog signaling in development and cancer. *Dev Cell,* 15**,** 801-12.

JOOST, H. G., BELL, G. I., BEST, J. D., BIRNBAUM, M. J., CHARRON, M. J., CHEN, Y. T., DOEGE, H., JAMES, D. E., LODISH, H. F., MOLEY, K. H., MOLEY, J. F., MUECKLER, M., ROGERS, S., SCHüRMANN, A., SEINO, S. & THORENS, B. 2002. Nomenclature of the GLUT/SLC2A family of sugar/polyol transport facilitators. *American Journal of Physiology-Endocrinology and Metabolism,* 282**,** E974-E976.

JURASCHKA, K. & TAYLOR, M. D. 2019. Medulloblastoma in the age of molecular subgroups: a review. *J Neurosurg Pediatr,* 24**,** 353-363.

KAATSCH, P., RICKERT, C. H., KüHL, L., SCHüZ, J. & MICHAELIS, J. 2001. Population-based epidemiologic data on brain tumors in German children. *Cancer,* 92**,** 3155-3164.

KAPOOR, K., FINER-MOORE, J. S., PEDERSEN, B. P., CABONI, L., WAIGHT, A., HILLIG, R. C., BRINGMANN, P., HEISLER, I., MüLLER, T., SIEBENEICHER, H. & STROUD, R. M. 2016. Mechanism of inhibition of human glucose transporter GLUT1 is conserved between cytochalasin B and phenylalanine amides. *Proc Natl Acad Sci U S A,* 113**,** 4711-6.

KAźMIERCZAK-BARAńSKA, J., BOGUSZEWSKA, K., ADAMUS-GRABICKA, A. & KARWOWSKI, B. T. 2020. Two Faces of Vitamin C-Antioxidative and Pro-Oxidative Agent. *Nutrients,* 12.

KEHRER, J. P. 2000. The Haber-Weiss reaction and mechanisms of toxicity. *Toxicology,* 149**,** 43-50.

KHAN, R. B., PATAY, Z., KLIMO, P., HUANG, J., KUMAR, R., BOOP, F. A., RACHES, D., CONKLIN, H. M., SHARMA, R., SIMMONS, A., SADIGHI, Z. S., ONAR-THOMAS, A., GAJJAR, A. & ROBINSON, G. W. 2021. Clinical features, neurologic recovery, and risk factors of postoperative posterior fossa syndrome and delayed recovery: a prospective study. *Neuro Oncol,* 23**,** 1586-1596.

KIM, J., LEE, S. D., CHANG, B., JIN, D. H., JUNG, S. I., PARK, M. Y., HAN, Y., YANG, Y., IL KIM, K., LIM, J. S., KANG, Y. S. & LEE, M. S. 2012. Enhanced antitumor activity of vitamin C via p53 in cancer cells. *Free Radic Biol Med,* 53**,** 1607-15.

KOO, K. Y., MOON, K., SONG, H. S. & LEE, M.-S. 2025. Metabolic regulation by p53: Implications for cancer therapy. *Molecules and Cells,* 48**,** 100198.

KOOL, M., KORSHUNOV, A., REMKE, M., JONES, D. T. W., SCHLANSTEIN, M., NORTHCOTT, P. A., CHO, Y. J., KOSTER, J., SCHOUTEN-VAN MEETEREN, A., VAN VUURDEN, D., CLIFFORD, S. C., PIETSCH, T., VON BUEREN, A. O., RUTKOWSKI, S., MCCABE, M., COLLINS, V. P., BäCKLUND, M. L., HABERLER, C., BOURDEAUT, F., DELATTRE, O., DOZ, F., ELLISON, D. W., GILBERTSON, R. J., POMEROY, S. L., TAYLOR, M. D., LICHTER, P. & PFISTER, S. M. 2012. Molecular subgroups of medulloblastoma: an international meta-analysis of transcriptome, genetic aberrations, and clinical data of WNT, SHH, Group 3, and Group 4 medulloblastomas. *Acta Neuropathologica,* 123**,** 473-484.

KWON, O., ECK, P., CHEN, S. L., CORPE, C. P., LEE, J. H., KRUHLAK, M. & LEVINE, M. 2007. Inhibition of the intestinal glucose transporter GLUT2 by flavonoids. *Faseb Journal,* 21**,** 366-377.

LAM, D., ENRIGHT, H. A., CADENA, J., PETERS, S. K. G., SALES, A. P., OSBURN, J. J., SOSCIA, D. A., KULP, K. S., WHEELER, E. K. & FISCHER, N. O. 2019. Tissue-specific extracellular matrix accelerates the formation of neural networks and communities in a neuron-glia co-culture on a multi-electrode array. *Scientific Reports,* 9**,** 15.

LARSEN, A. M. H., KUCZEK, D. E., KALVISA, A., SIERSBæK, M. S., THORSETH, M. L., JOHANSEN, A. Z., CARRETTA, M., GRNTVED, L., VANG, O. & MADSEN, D. H. 2020. Collagen Density Modulates the Immunosuppressive Functions of Macrophages. *Journal of Immunology,* 205**,** 1461-1472.

LAZOW, M. A., PALMER, J. D., FOULADI, M. & SALLOUM, R. 2022. Medulloblastoma in the Modern Era: Review of Contemporary Trials, Molecular Advances, and Updates in Management. *Neurotherapeutics,* 19**,** 1733-1751.

LEARY, S. E. S., PACKER, R. J., LI, Y., BILLUPS, C. A., SMITH, K. S., JAJU, A., HEIER, L., BURGER, P., WALSH, K., HAN, Y., EMBRY, L., HADLEY, J., KUMAR, R., MICHALSKI, J., HWANG, E., GAJJAR, A., POLLACK, I. F., FOULADI, M., NORTHCOTT, P. A. & OLSON, J. M. 2021. Efficacy of Carboplatin and Isotretinoin in Children With High-risk Medulloblastoma: A Randomized Clinical Trial From the Children's Oncology Group. *JAMA Oncol,* 7**,** 1313-1321.

LEE, S. J., JEONG, J. H., LEE, I. H., LEE, J., JUNG, J. H., PARK, H. Y., LEE, D. H. & CHAE, Y. S. 2019. Effect of High-dose Vitamin C Combined With Anti-cancer Treatment on Breast Cancer Cells. *Anticancer Research,* 39**,** 751-758.

LEE, Y.-C., HUANG, H.-Y., CHANG, C.-J., CHENG, C.-H. & CHEN, Y.-T. 2010. Mitochondrial GLUT10 facilitates dehydroascorbic acid import and protects cells against oxidative stress: mechanistic insight into arterial tortuosity syndrome. *Human Molecular Genetics,* 19**,** 3721-3733.

LEVENTAL, K. R., YU, H. M., KASS, L., LAKINS, J. N., EGEBLAD, M., ERLER, J. T., FONG, S. F. T., CSISZAR, K., GIACCIA, A., WENINGER, W., YAMAUCHI, M., GASSER, D. L. & WEAVER, V. M. 2009. Matrix Crosslinking Forces Tumor Progression by Enhancing Integrin Signaling. *Cell,* 139**,** 891-906.

LI, T., MAO, C., WANG, X., SHI, Y. & TAO, Y. 2020. Epigenetic crosstalk between hypoxia and tumor driven by HIF regulation. *J Exp Clin Cancer Res,* 39**,** 224.

LIANG, Y., DIEHN, M., BOLLEN, A. W., ISRAEL, M. A. & GUPTA, N. 2008. Type I collagen is overexpressed in medulloblastoma as a component of tumor microenvironment. *Journal of Neuro-Oncology,* 86**,** 133-141.

LIM, J. Y., KIM, D., KIM, B. R., JUN, J. S., YEOM, J. S., PARK, J. S., SEO, J. H., PARK, C. H., WOO, H. O., YOUN, H. S., BAIK, S. C., LEE, W. K., CHO, M. J. & RHEE, K. H. 2016. Vitamin C induces apoptosis in AGS cells via production of ROS of mitochondria. *Oncology Letters,* 12**,** 4270-4276.

LIN, C. Y., ERKEK, S., TONG, Y. A., YIN, L. L., FEDERATION, A. J., ZAPATKA, M., HALDIPUR, P., KAWAUCHI, D., RISCH, T., WARNATZ, H. J., WORST, B. C., JU, B. S., ORR, B. A., ZEID, R., POLASKI, D. R., SEGURA-WANG, M., WASZAK, S. M., JONES, D. T. W., KOOL, M., HOVESTADT, V., BUCHHALTER, I., SIEBER, L., JOHANN, P., CHAVEZ, L., GRöSCHEL, S., RYZHOVA, M., KORSHUNOV, A., CHEN, W. B., CHIZHIKOV, V. V., MILLEN, K. J., AMSTISLAVSKIY, V., LEHRACH, H., YASPO, M. L., EILS, R., LICHTER, P., KORBEL, J. O., PFISTER, S. M., BRADNER, J. E. & NORTHCOTT, P. A. 2016. Active medulloblastoma enhancers reveal subgroup-specific cellular origins. *Nature,* 530**,** 57-+.

LINKE, F., JOHNSON, J. E. C., KERN, S., BENNETT, C. D., LOURDUSAMY, A., LEA, D., CLIFFORD, S. C., MERRY, C. L. R., STOLNIK, S., ALEXANDER, M. R., PEET, A. C., SCURR, D. J., GRIFFITHS, R. L., GRABOWSKA, A. M., KERR, I. D. & COYLE, B. 2023. Identifying new biomarkers of aggressive Group 3 and SHH medulloblastoma using 3D hydrogel models, single cell RNA sequencing and 3D OrbiSIMS imaging. *Acta Neuropathologica Communications,* 11**,** 18.

LINSTER, C. L. & VAN SCHAFTINGEN, E. 2007. Vitamin C - Biosynthesis, recycling and degradation in mammals. *Febs Journal,* 274**,** 1-22.

LIU, J., XIAO, Q., XIAO, J., NIU, C., LI, Y., ZHANG, X., ZHOU, Z., SHU, G. & YIN, G. 2022. Wnt/β-catenin signalling: function, biological mechanisms, and therapeutic opportunities. *Signal Transduction and Targeted Therapy,* 7**,** 3.

LIU, J. R., HINKHOUSE, M. M., SUN, W. Q., WEYDERT, C. J., RITCHIE, J. M., OBERLEY, L. W. & CULLEN, J. J. 2004. Redox regulation of pancreatic cancer cell growth: Role of glutathione peroxidase in the suppression of the malignant phenotype. *Human Gene Therapy,* 15**,** 239-250.

LIVAK, K. J. & SCHMITTGEN, T. D. 2001. Analysis of relative gene expression data using real-time quantitative PCR and the 2(-Delta Delta C(T)) Method. *Methods,* 25**,** 402-8.

LONGCHAR, A. & PRASAD, S. B. 2015. Biochemical changes associated with ascorbic acid-cisplatin combination therapeutic efficacy and protective effect on cisplatin-induced toxicity in tumor-bearing mice. *Toxicol Rep,* 2**,** 489-503.

LOUIS, D. N., PERRY, A., REIFENBERGER, G., VON DEIMLING, A., FIGARELLA-BRANGER, D., CAVENEE, W. K., OHGAKI, H., WIESTLER, O. D., KLEIHUES, P. & ELLISON, D. W. 2016. The 2016 World Health Organization Classification of Tumors of the Central Nervous System: a summary. *Acta Neuropathologica,* 131**,** 803-820.

LOUIS, D. N., PERRY, A., WESSELING, P., BRAT, D. J., CREE, I. A., FIGARELLA-BRANGER, D., HAWKINS, C., NG, H. K., PFISTER, S. M., REIFENBERGER, G., SOFFIETTI, R., VON DEIMLING, A. & ELLISON, D. W. 2021. The 2021 WHO Classification of Tumors of the Central Nervous System: a summary. *Neuro-Oncology,* 23**,** 1231-1251.

LU, P., TAKAI, K., WEAVER, V. M. & WERB, Z. 2011. Extracellular matrix degradation and remodeling in development and disease. *Cold Spring Harb Perspect Biol,* 3.

LU, P. F., WEAVER, V. M. & WERB, Z. 2012. The extracellular matrix: A dynamic niche in cancer progression. *Journal of Cell Biology,* 196**,** 395-406.

MAEKAWA, T., MIYAKE, T., TANI, M. & UEMOTO, S. 2022. Diverse antitumor effects of ascorbic acid on cancer cells and the tumor microenvironment. *Front Oncol,* 12**,** 981547.

MANDL, J., SZARKA, A. & BáNHEGYI, G. 2009. Vitamin C: update on physiology and pharmacology. *Br J Pharmacol,* 157**,** 1097-110.

MASSIMINO, M., BIASSONI, V., GANDOLA, L., GARRè, M. L., GATTA, G., GIANGASPERO, F., POGGI, G. & RUTKOWSKI, S. 2016. Childhood medulloblastoma. *Critical Reviews in Oncology Hematology,* 105**,** 35-51.

MAY, J. M., MENDIRATTA, S., QU, Z. C. & LOGGINS, E. 1999. Vitamin C recycling and function in human monocytic U-937 cells. *Free Radical Biology and Medicine,* 26**,** 1513-1523.

MEDINA, R. A. & OWEN, G. I. 2002. Glucose transporters: expression, regulation and cancer. *Biological Research,* 35**,** 9-26.

MILLARD, N. E. & DE BRAGANCA, K. C. 2016. Medulloblastoma. *Journal of Child Neurology,* 31**,** 1341-1353.

MOERTEL, C. G., FLEMING, T. R., CREAGAN, E. T., RUBIN, J., OCONNELL, M. J. & AMES, M. M. 1985. HIGH-DOSE VITAMIN-C VERSUS PLACEBO IN THE TREATMENT OF PATIENTS WITH ADVANCED CANCER WHO HAVE HAD NO PRIOR CHEMOTHERAPY - A RANDOMIZED DOUBLE-BLIND COMPARISON. *New England Journal of Medicine,* 312**,** 137-141.

NJUS, D., KELLEY, P. M., TU, Y. J. & SCHLEGEL, H. B. 2020. Ascorbic acid: The chemistry underlying its antioxidant properties. *Free Radical Biology and Medicine,* 159**,** 37-43.

NORTHCOTT, P. A., BUCHHALTER, I., MORRISSY, A. S., HOVESTADT, V., WEISCHENFELDT, J., EHRENBERGER, T., GRöBNER, S., SEGURA-WANG, M., ZICHNER, T., RUDNEVA, V. A., WARNATZ, H. J., SIDIROPOULOS, N., PHILLIPS, A. H., SCHUMACHER, S., KLEINHEINZ, K., WASZAK, S. M., ERKEK, S., JONES, D. T. W., WORST, B. C., KOOL, M., ZAPATKA, M., JäGER, N., CHAVEZ, L., HUTTER, B., BIEG, M., PARAMASIVAM, N., HEINOLD, M., GU, Z. G., ISHAQUE, N., JäGER-SCHMIDT, C., IMBUSCH, C. D., JUGOLD, A., HüBSCHMANN, D., RISCH, T., AMSTISLAVSKIY, V., GONZALEZ, F. G. R., WEBER, U. D., WOLF, S., ROBINSON, G. W., ZHOU, X., WU, G., FINKELSTEIN, D., LIU, Y. L., CAVALLI, F. M. G., LUU, B., RAMASWAMY, V., WU, X. C., KOSTER, J., RYZHOVA, M., CHO, Y. J., POMEROY, S. L., HEROLD-MENDE, C., SCHUHMANN, M., EBINGER, M., LIAU, L. M., MORA, J., MCLENDON, E., JABADO, N., KUMABE, T., CHUAH, E., MA, Y., MOORE, R. A., MUNGALL, A. J., MUNGALL, K. L., THIESSEN, N., TSE, K., WONG, T., JONES, S. J. M., WITT, O., MILDE, T., VON DEIMLING, A., CAPPER, D., KORSHUNOV, A., YASPO, M. L., KRIWACKI, R., GAJJAR, A., ZHANG, J. H., BEROUKHIM, R., FRAENKEL, E., KORBEL, J. O., BRORS, B., SCHLESNER, M., EILS, R., MARRA, M. A., PFISTER, S. M., TAYLOR, M. D. & LICHTER, P. 2017. The whole-genome landscape of medulloblastoma subtypes. *Nature,* 547**,** 311-+.

NORTHCOTT, P. A., HIELSCHER, T., DUBUC, A., MACK, S., SHIH, D., REMKE, M., AL-HALABI, H., ALBRECHT, S., JABADO, N., EBERHART, C. G., GRAJKOWSKA, W., WEISS, W. A., CLIFFORD, S. C., BOUFFET, E., RUTKA, J. T., KORSHUNOV, A., PFISTER, S. & TAYLOR, M. D. 2011a. Pediatric and adult sonic hedgehog medulloblastomas are clinically and molecularly distinct. *Acta Neuropathologica,* 122**,** 231-240.

NORTHCOTT, P. A., KORSHUNOV, A., WITT, H., HIELSCHER, T., EBERHART, C. G., MACK, S., BOUFFET, E., CLIFFORD, S. C., HAWKINS, C. E., FRENCH, P., RUTKA, J. T., PFISTER, S. & TAYLOR, M. D. 2011b. Medulloblastoma Comprises Four Distinct Molecular Variants. *Journal of Clinical Oncology,* 29**,** 1408-1414.

NORTHCOTT, P. A., NAKAHARA, Y., WU, X. C., FEUK, L., ELLISON, D. W., CROUL, S., MACK, S., KONGKHAM, P. N., PEACOCK, J., DUBUC, A., RA, Y. S., ZILBERBERG, K., MCLEOD, J., SCHERER, S. W., RAO, J. S., EBERHART, C. G., GRAJKOWSKA, W., GILLESPIE, Y., LACH, B., GRUNDY, R., POLLACK, I. F., HAMILTON, R. L., VAN METER, T., CARLOTTI, C. G., BOOP, F., BIGNER, D., GILBERTSON, R. J., RUTKA, J. T. & TAYLOR, M. D. 2009. Multiple recurrent genetic events converge on control of histone lysine methylation in medulloblastoma. *Nature Genetics,* 41**,** 465-472.

NORTHCOTT, P. A., SHIH, D. J. H., PEACOCK, J., GARZIA, L., MORRISSY, A. S., ZICHNER, T., STüTZ, A. M., KORSHUNOV, A., REIMAND, J., SCHUMACHER, S. E., BEROUKHIM, R., ELLISON, D. W., MARSHALL, C. R., LIONEL, A. C., MACK, S., DUBUC, A., YAO, Y., RAMASWAMY, V., LUU, B., ROLIDER, A., CAVALLI, F. M. G., WANG, X., REMKE, M., WU, X. C., CHIU, R. Y. B., CHU, A., CHUAH, E., CORBETT, R. D., HOAD, G. R., JACKMAN, S. D., LI, Y. S., LO, A., MUNGALL, K. L., NIP, K. M., QIAN, J. Q., RAYMOND, A. G. J., THIESSEN, N., VARHOL, R. J., BIROL, I., MOORE, R. A., MUNGALL, A. J., HOLT, R., KAWAUCHI, D., ROUSSEL, M. F., KOOL, M., JONES, D. T. W., WITT, H., FERNANDEZ-L, A., KENNEY, A. M., WECHSLER-REYA, R. J., DIRKS, P., AVIV, T., GRAJKOWSKA, W. A., PEREK-POLNIK, M., HABERLER, C. C., DELATTRE, O., REYNAUD, S. S., DOZ, F. F., PERNET-FATTET, S. S., CHO, B. K., KIM, S. K., WANG, K. C., SCHEURLEN, W., EBERHART, C. G., FèVRE-MONTANGE,

M., JOUVET, A., POLLACK, I. F., FAN, X., MURASZKO, K. M., GILLESPIE, G. Y., DI ROCCO, C., MASSIMI, L., MICHIELS, E. M. C., KLOOSTERHOF, N. K., FRENCH, P. J., KROS, J. M., OLSON, J. M., ELLENBOGEN, R. G., ZITTERBART, K., KREN, L., THOMPSON, R. C., COOPER, M. K., LACH, B., MCLENDON, R. E., BIGNER, D. D., FONTEBASSO, A., ALBRECHT, S., JABADO, N., LINDSEY, J. C., BAILEY, S., GUPTA, N., WEISS, W. A., BOGNáR, L., KLEKNER, A., VAN METER, T. E., KUMABE, T., TOMINAGA, T., ELBABAA, S. K., LEONARD, J. R., RUBIN, J. B., et al. 2012. Subgroup-specific structural variation across 1,000 medulloblastoma genomes. *Nature,* 488**,** 49-56.

NUNES, A. S., BARROS, A. S., COSTA, E. C., MOREIRA, A. F. & CORREIA, I. J. 2019. 3D tumor spheroids as in vitro models to mimic in vivo human solid tumors resistance to therapeutic drugs. *Biotechnology and Bioengineering,* 116**,** 206-226.

ORR, B. A. 2020. Pathology, diagnostics, and classification of medulloblastoma. *Brain Pathology,* 30**,** 664-678.

PADAYATTY, S. J., KATZ, A., WANG, Y. H., ECK, P., KWON, O., LEE, J. H., CHEN, S. L., CORPE, C., DUTTA, A., DUTTA, S. K. & LEVINE, M. 2003. Vitamin C as an antioxidant: Evaluation of its role in disease prevention. *Journal of the American College of Nutrition,* 22**,** 18-35.

PADAYATTY, S. J., SUN, H., WANG, Y. H., RIORDAN, H. D., HEWITT, S. M., KATZ, A., WESLEY, R. A. & LEVINE, M. 2004. Vitamin C pharmacokinetics: Implications for oral and intravenous use. *Annals of Internal Medicine,* 140**,** 533-537.

PADOVANI, L., HORAN, G. & AJITHKUMAR, T. 2019. Radiotherapy Advances in Paediatric Medulloblastoma Treatment. *Clinical Oncology,* 31**,** 171-181.

PASZEK, M. J. & WEAVER, V. M. 2004. The tension mounts: Mechanics meets morphogenesis and malignancy. *Journal of Mammary Gland Biology and Neoplasia,* 9**,** 325-342.

PATAPOUTIAN, A. & REICHARDT, L. F. 2000. Roles of Wnt proteins in neural development and maintenance. *Current Opinion in Neurobiology,* 10**,** 392-399.

PERUS, L. J. M. & WALSH, L. A. 2019. Microenvironmental Heterogeneity in Brain Malignancies. *Frontiers in Immunology,* 10**,** 15.

PETERKOFSKY, B. 1991a. ASCORBATE REQUIREMENT FOR HYDROXYLATION AND SECRETION OF PROCOLLAGEN - RELATIONSHIP TO INHIBITION OF COLLAGEN-SYNTHESIS IN SCURVY. *American Journal of Clinical Nutrition,* 54**,** S1135-S1140.

PETERKOFSKY, B. 1991b. Ascorbate requirement for hydroxylation and secretion of procollagen: relationship to inhibition of collagen synthesis in scurvy. *Am J Clin Nutr,* 54**,** 1135s-1140s.

PICKLES, J. C., HAWKINS, C., PIETSCH, T. & JACQUES, T. S. 2018. CNS embryonal tumours: WHO 2016 and beyond. *Neuropathology and Applied Neurobiology,* 44**,** 151-162.

PINNELL, S. R. 1982. REGULATION OF COLLAGEN-SYNTHESIS. *Journal of Investigative Dermatology,* 79**,** S73-S76.

PINNELL, S. R. 1985. REGULATION OF COLLAGEN BIOSYNTHESIS BY ASCORBIC-ACID - A REVIEW. *Yale Journal of Biology and Medicine,* 58**,** 553-559.

PIZER, B. L. & CLIFFORD, S. C. 2009. The potential impact of tumour biology on improved clinical practice for medulloblastoma: progress towards biologically driven clinical trials. *British Journal of Neurosurgery,* 23**,** 364-375.

POGGI, A., REGGIANI, F., AZEVEDO, H. S., RAFFAGHELLO, L. & PEREIRA, R. C. 2025. Medulloblastoma: biology and immunotherapy. *Frontiers in Immunology,* 16**,** 28.

PORTUGAL, C. C. 2024. Ascorbate and its transporter SVCT2: The dynamic duo's integrated roles in CNS neurobiology and pathophysiology. *Free Radical Biology and Medicine,* 212**,** 448-462.

POUSSAINT, T. Y., PANIGRAHY, A. & HUISMAN, T. 2015. Pediatric brain tumors. *Pediatric Radiology,* 45**,** 443-453.

POZZER, D., INVENIZZI, R. W., BLAAUW, B., CANTONI, O. & ZITO, E. 2021. Ascorbic Acid Route to the Endoplasmic Reticulum: Function and Role in Disease. *Antioxidants & Redox Signaling,* 34**,** 845-855.

QUAIL, D. F. & JOYCE, J. A. 2017. The Microenvironmental Landscape of Brain Tumors. *Cancer Cell,* 31**,** 326-341.

RAFFEL, C. 2004. Medulloblastoma: Molecular genetics and animal models. *Neoplasia,* 6**,** 310-322.

RAMASWAMY, S., TAMAYO, P., RIFKIN, R., MUKHERJEE, S., YEANG, C. H., ANGELO, M., LADD, C., REICH, M., LATULIPPE, E., MESIROV, J. P., POGGIO, T., GERALD, W., LODA, M., LANDER, E. S. & GOLUB, T. R. 2001. Multiclass cancer diagnosis using tumor gene expression signatures. *Proceedings of the National Academy of Sciences of the United States of America,* 98**,** 15149-15154.

RAN, F. A., HSU, P. D., WRIGHT, J., AGARWALA, V., SCOTT, D. A. & ZHANG, F. 2013. Genome engineering using the CRISPR-Cas9 system. *Nature Protocols,* 8**,** 2281-2308.

ROPER, S. J. & COYLE, B. 2022. Establishing an In Vitro 3D Spheroid Model to Study Medulloblastoma Drug Response and Tumor Dissemination. *Current Protocols,* 2.

ROPER, S. J., LINKE, F., SCOTTING, P. J. & COYLE, B. 2021. 3D spheroid models of paediatric SHH medulloblastoma mimic tumour biology, drug response and metastatic dissemination. *Sci Rep,* 11**,** 4259.

ROSSI, M., STEKLOV, M., HUBERTY, F., NGUYEN, T., MARIJSSE, J., JACQUES-HESPEL, C., NAJM, P., LONEZ, C. & BREMAN, E. 2023. Efficient shRNA-based knockdown of multiple target genes for cell therapy using a chimeric miRNA cluster platform. *Mol Ther Nucleic Acids,* 34**,** 102038.

ROZARIO, T. & DESIMONE, D. W. 2010. The extracellular matrix in development and morphogenesis: a dynamic view. *Dev Biol,* 341**,** 126-40.

RUMSEY, S. C., KWON, O., XU, G. W., BURANT, C. F., SIMPSON, I. & LEVINE, M. 1997. Glucose transporter isoforms GLUT1 and GLUT3 transport dehydroascorbic acid. *Journal of Biological Chemistry,* 272**,** 18982-18989.

SABLINA, A. A., BUDANOV, A. V., ILYINSKAYA, G. V., AGAPOVA, L. S., KRAVCHENKO, J. E. & CHUMAKOV, P. M. 2005. The antioxidant function of the p53 tumor suppressor. *Nat Med,* 11**,** 1306-13.

SAVINI, I., ROSSI, A., PIERRO, C., AVIGLIANO, L. & CATANI, M. V. 2008. SVCT1 and SVCT2: key proteins for vitamin C uptake. *Amino Acids,* 34**,** 347-355.

SCHINDELIN, J., ARGANDA-CARRERAS, I., FRISE, E., KAYNIG, V., LONGAIR, M., PIETZSCH, T., PREIBISCH, S., RUEDEN, C., SAALFELD, S., SCHMID, B., TINEVEZ, J. Y., WHITE, D. J., HARTENSTEIN, V., ELICEIRI, K., TOMANCAK, P. & CARDONA, A. 2012. Fiji: an open-source platform for biological-image analysis. *Nature Methods,* 9**,** 676-682.

SHOULDERS, M. D. & RAINES, R. T. 2009. Collagen Structure and Stability. *Annual Review of Biochemistry,* 78**,** 929-958.

SIES, H. & JONES, D. P. 2020. Reactive oxygen species (ROS) as pleiotropic physiological signalling agents. *Nature Reviews Molecular Cell Biology,* 21**,** 363-383.

SKOWRON, P., FAROOQ, H., CAVALLI, F. M. G., MORRISSY, A. S., LY, M., HENDRIKSE, L. D., WANG, E. Y., DJAMBAZIAN, H., ZHU, H., MUNGALL, K. L., TRINH, Q. M., ZHENG, T. N., DAI, S. Z., STUCKLIN, A. S. G., VLADOIU, M. C., FONG, V., HOLGADO, B. L., NOR, C., WU, X. C., ABD-RABBO, D., BéRUBé, P., WANG, Y. C., LUU, B., SUAREZ, R. A., RASTAN, A., GILLMOR, A. H., LEE, J. J. Y., ZHANG, X. Y., DANIELS, C., DIRKS, P., MALKIN, D., BOUFFET, E., TABORI, U., LOUKIDES, J., DOZ, F. P., BOURDEAUT, F., DELATTRE, O. O., MASLIAH-PLANCHON, J., AYRAULT, O., KIM, S. K., MEYRONET, D., GRAJKOWSKA, W. A., CARLOTTI, C. G., DE TORRES, C., MORA, J., EBERHART, C. G., VAN MEIR, E. G., KUMABE, T., FRENCH, P. J., KROS, J. M., JABADO, N., LACH, B., POLLACK, I. F., HAMILTON, R. L., RAO, A. A. N., GIANNINI, C., OLSON, J. M., BOGNáR, L., KLEKNER, A., ZITTERBART, K., PHILLIPS, J. J., THOMPSON, R. C., COOPER, M. K., RUBIN, J. B., LIAU, L. M., GARAMI, M., HAUSER, P., LI, K. K. W., NG, H. K., POON, W. S., GILLESPIE, G. Y., CHAN, J. A., JUNG, S., MCLENDON, R. E., THOMPSON, E. M., ZAGZAG, D., VIBHAKAR, R., RA, Y. S., GARRE, M. L., SCHüLLER, U., SHOFUDA, T., FARIA, C. C., LóPEZ-AGUILAR, E., ZADEH, G., HUI, C. C., RAMASWAMY, V., BAILEY, S. D., JONES, S. J., MUNGALL, A. J., MOORE, R. A., CALARCO, J. A., STEIN, L. D., BADER, G. D., REIMAND, J., RAGOUSSIS, J., WEISS, W. A., MARRA, M. A., SUZUKI, H. & TAYLOR, M. D. 2021. The transcriptional landscape of Shh medulloblastoma. *Nature Communications,* 12**,** 17.

SKOWRON, P., RAMASWAMY, V. & TAYLOR, M. D. 2015. Genetic and molecular alterations across medulloblastoma subgroups. *Journal of Molecular Medicine-Jmm,* 93**,** 1075-1084.

SMIT, M. J., MARTINI, T. E. I., ARMANDARI, I., BOčKAJ, I., ZOMERMAN, W. W., DE CAMARGO MAGALHãES, E. S., SIRAGNA, Z., MEEUWSEN, T. G. J., SCHERPEN, F. J. G., SCHOOTS, M. H., RITSEMA, M., DEN DUNNEN, W. F. A., HOVING, E. W., PARIDAEN, J., DE HAAN, G., GURYEV, V. & BRUGGEMAN, S. W. M. 2022. The developmental stage of the medulloblastoma cell-of-origin restricts Sonic hedgehog pathway usage and drug sensitivity. *J Cell Sci,* 135.

SMITH, K. S., BIHANNIC, L., GUDENAS, B. L., HALDIPUR, P., TAO, R., GAO, Q., LI, Y., ALDINGER, K. A., ISKUSNYKH, I. Y., CHIZHIKOV, V. V., SCOGGINS, M., ZHANG, S., EDWARDS, A., DENG, M., GLASS, I. A., OVERMAN, L. M., MILLMAN, J., SJOBOEN, A. H., HADLEY, J., GOLSER, J., MANKAD, K., SHEPPARD, H., ONAR-THOMAS, A., GAJJAR, A., ROBINSON, G. W., HOVESTADT, V., ORR, B. A., PATAY, Z., MILLEN, K. J. & NORTHCOTT, P. A. 2022. Unified rhombic lip origins of group 3 and group 4 medulloblastoma. *Nature,* 609**,** 1012-1020.

SMOLL, N. R. & DRUMMOND, K. J. 2012. The incidence of medulloblastomas and primitive neurectodermal tumours in adults and children. *Journal of Clinical Neuroscience,* 19**,** 1541-1544.

SOBCZAK-KUPIEC, A., DRABCZYK, A., FLORKIEWICZ, W., GłąB, M., KUDłACIK-KRAMARCZYK, S., SłOTA, D., TOMALA, A. & TYLISZCZAK, B. 2021. Review of the

Applications of Biomedical Compositions Containing Hydroxyapatite and Collagen Modified by Bioactive Components. *Materials (Basel),* 14.

SPITZ, D. R., PHILLIPS, J. W., ADAMS, D. T., SHERMAN, C. M., DEEN, D. F. & LI, G. C. 1993. Cellular resistance to oxidative stress is accompanied by resistance to cisplatin: the significance of increased catalase activity and total glutathione in hydrogen peroxide-resistant fibroblasts. *J Cell Physiol,* 156**,** 72-9.

STEPHENSON, C., LEVIN, R., SPECTOR, T. & LIS, C. 2013. Phase I clinical trial to evaluate the safety, tolerability, and pharmacokinetics of high-dose intravenous ascorbic acid in patients with advanced cancer. *Cancer chemotherapy and pharmacology,* 72.

SUN, L., MORITAKE, T., ZHENG, Y.-W., SUZUKI, K., GERELCHULUUN, A., HONG, Z., ZENKOH, J., TANIGUCHI, H. & TSUBOI, K. 2012. In vitro stemness characterization of radio-resistant clones isolated from a medulloblastoma cell line ONS-76. *Journal of Radiation Research,* 54**,** 61-69.

TAKANAGA, H., MACKENZIE, B. & HEDIGER, M. A. 2004. Sodium-dependent ascorbic acid transporter family SLC23. *Pflugers Archiv-European Journal of Physiology,* 447**,** 677-682.

TAYLOR, M. D., MAINPRIZE, T. G. & RUTKA, J. T. 2000. Molecular insight into medulloblastoma and central nervous system primitive neuroectodermal tumor biology from hereditary syndromes: A review. *Neurosurgery,* 47**,** 888-901.

TAYLOR, M. D., NORTHCOTT, P. A., KORSHUNOV, A., REMKE, M., CHO, Y. J., CLIFFORD, S. C., EBERHART, C. G., PARSONS, D. W., RUTKOWSKI, S., GAJJAR, A., ELLISON, D. W., LICHTER, P., GILBERTSON, R. J., POMEROY, S. L., KOOL, M. & PFISTER, S. M. 2012. Molecular subgroups of medulloblastoma: the current consensus. *Acta Neuropathologica,* 123**,** 465-472.

THOMPSON, E. M., HIELSCHER, T., BOUFFET, E., REMKE, M., LUU, B., GURURANGAN, S., MCLENDON, R. E., BIGNER, D. D., LIPP, E. S., PERREAULT, S., CHO, Y. J., GRANT, G., KIM, S. K., LEE, J. Y., RAO, A. A. N., GIANNINI, C., LI, K. K. W., NG, H. K., YAO, Y., KUMABE, T., TOMINAGA, T., GRAJKOWSKA, W. A., PEREK-POLNIK, M., LOW, D. C. Y., SEOW, W. T., CHANG, K. T. E., MORA, J., POLLACK, I. F., HAMILTON, R. L., LEARY, S., MOORE, A. S., INGRAM, W. J., HALLAHAN, A. R., JOUVET, A., FèVRE-MONTANGE, M., VASILJEVIC, A., FAURE-CONTER, C., SHOFUDA, T., KAGAWA, N., HASHIMOTO, N., JABADO, N., WEIL, A. G., GAYDEN, T., WATAYA, T., SHALABY, T., GROTZER, M., ZITTERBART, K., STERBA, J., KREN, L., HORTOBáGYI, T., KLEKNER, A., LáSZLó, B., POCZA, T., HAUSER, P., SCHüLLER, U., JUNG, S., JANG, W. Y., FRENCH, P. J., KROS, J. M., VAN VEELEN, M. L. C., MASSIMI, L., LEONARD, J. R., RUBIN, J. B., VIBHAKAR, R., CHAMBLESS, L. B., COOPER, M. K., THOMPSON, R. C., FARIA, C. C., CARVALHO, A., NUNES, S., PIMENTEL, J., FAN, X., MURASZKO, K. M., LóPEZ-AGUILAR, E., LYDEN, D., GARZIA, L., SHIH, D. J. H., KIJIMA, N., SCHNEIDER, C., ADAMSKI, J., NORTHCOTT, P. A., KOOL, M., JONES, D. T. W., CHAN, J. A., NIKOLIC, A., GARRE, M. L., VAN MEIR, E. G., OSUKA, S., OLSON, J. J., JAHANGIRI, A., CASTRO, B. A., GUPTA, N., WEISS, W. A., MOXON-EMRE, I., MABBOTT, D. J., LASSALETTA, A., HAWKINS, C. E., TABORI, U., DRAKE, J., KULKARNI, A., et al. 2016. Prognostic value of medulloblastoma extent of resection after accounting for molecular subgroup: a retrospective integrated clinical and molecular analysis. *Lancet Oncology,* 17**,** 484-495.

TRACHOOTHAM, D., ALEXANDRE, J. & HUANG, P. 2009. Targeting cancer cells by ROS-mediated mechanisms: a radical therapeutic approach? *Nat Rev Drug Discov,* 8**,** 579-91.

TRAVERSO, N., RICCIARELLI, R., NITTI, M., MARENGO, B., FURFARO, A. L., PRONZATO, M. A., MARINARI, U. M. & DOMENICOTTI, C. 2013. Role of glutathione in cancer progression and chemoresistance. *Oxid Med Cell Longev,* 2013**,** 972913.

TROMBETTA-LIMA, M., ROSA-FERNANDES, L., ANGELI, C. B., MORETTI, I. F., FRANCO, Y. M., MOUSESSIAN, A. S., WAKAMATSU, A., LERARIO, A. M., OBA-SHINJO, S. M., PASQUALUCCI, C. A., MARIE, S. K. N. & PALMISANO, G. 2021. Extracellular Matrix Proteome Remodeling in Human Glioblastoma and Medulloblastoma. *Journal of Proteome Research,* 20**,** 4693-4707.

TSUKAGUCHI, H., TOKUI, T., MACKENZIE, B., BERGER, U. V., CHEN, X. Z., WANG, Y. X., BRUBAKER, R. F. & HEDIGER, M. A. 1999. A family of mammalian Na+-dependent L-ascorbic acid transporters. *Nature,* 399**,** 70-75.

VAN BREE, N. & WILHELM, M. 2022. The Tumor Microenvironment of Medulloblastoma: An Intricate Multicellular Network with Therapeutic Potential. *Cancers,* 14**,** 24.

VISLISEL, J. M., SCHAFER, F. Q. & BUETTNER, G. R. 2007. A simple and sensitive assay for ascorbate using a plate reader. *Analytical Biochemistry,* 365**,** 31-39.

VLADOIU, M. C., EL-HAMAMY, I., DONOVAN, L. K., FAROOQ, H., HOLGADO, B. L., SUNDARAVADANAM, Y., RAMASWAMY, V., HENDRIKSE, L. D., KUMAR, S., MACK, S. C., LEE, J. J. Y., FONG, V., JURASCHKA, K., PRZELICKI, D., MICHEALRAJ, A., SKOWRON, P., LUU, B., SUZUKI, H., MORRISSY, A. S., CAVALLI, F. M. G., GARZIA, L., DANIELS, C., WU, X. C., QAZI, M. A., SINGH, S. K., CHAN, J. A., MARRA, M. A., MALKIN, D., DIRKS, P., HEISLER, L., PUGH, T., NG, K., NOTTA, F., THOMPSON, E. M., KLEINMAN, C. L., JOYNER, A. L., JABADO, N., STEIN, L. & TAYLOR, M. D. 2019. Childhood cerebellar tumours mirror conserved fetal transcriptional programs. *Nature,* 572**,** 67-+.

VON BUEREN, A. O., KORTMANN, R. D., VON HOFF, K., FRIEDRICH, C., MYNAREK, M., MüLLER, K., GOSCHZIK, T., ZUR MüHLEN, A., GERBER, N., WARMUTH-METZ, M., SOERENSEN, N., DEINLEIN, F., BENESCH, M., ZWIENER, I., KWIECIEN, R., FALDUM, A., BODE, U., FLEISCHHACK, G., HOVESTADT, V., KOOL, M., JONES, D., NORTHCOTT, P., KUEHL, J., PFISTER, S., PIETSCH, T. & RUTKOWSKI, S. 2016. Treatment of Children and Adolescents With Metastatic Medulloblastoma and Prognostic Relevance of Clinical and Biologic Parameters. *J Clin Oncol,* 34**,** 4151-4160.

VOUSDEN, K. H. & PRIVES, C. 2009. Blinded by the Light: The Growing Complexity of p53. *Cell,* 137**,** 413-431.

WECHSLER-REYA, R. J. & SCOTT, M. P. 1999. Control of neuronal precursor proliferation in the cerebellum by sonic hedgehog. *Neuron,* 22**,** 103-114.

WELCH, R. W., WANG, Y. H., CROSSMAN, A., PARK, J. B., KIRK, K. L. & LEVINE, M. 1995. ACCUMULATION OF VITAMIN-C (ASCORBATE) AND ITS OXIDIZED METABOLITE DEHYDROASCORBIC ACID OCCURS BY SEPARATE MECHANISMS. *Journal of Biological Chemistry,* 270**,** 12584-12592.

WELLS, W. W., XU, D. P., YANG, Y. F. & ROCQUE, P. A. 1990. MAMMALIAN THIOLTRANSFERASE (GLUTAREDOXIN) AND PROTEIN DISULFIDE ISOMERASE HAVE DEHYDROASCORBATE REDUCTASE-ACTIVITY. *Journal of Biological Chemistry,* 265**,** 15361-15364.

WHITE, D. J., PURANEN, S., JOHNSON, M. S. & HEINO, J. 2004. The collagen receptor subfamily of the integrins. *International Journal of Biochemistry & Cell Biology,* 36**,** 1405-1410.

WILSON, J. X. 2005. Regulation of vitamin C transport. *Annual Review of Nutrition,* 25**,** 105-125.

WILSON, M. K., BAGULEY, B. C., WALL, C., JAMESON, M. B. & FINDLAY, M. P. 2014. Review of high-dose intravenous vitamin C as an anticancer agent. *Asia Pac J Clin Oncol,* 10**,** 22-37.

WINKLER, J., ABISOYE-OGUNNIYAN, A., METCALF, K. J. & WERB, Z. 2020. Concepts of extracellular matrix remodelling in tumour progression and metastasis. *Nature Communications,* 11**,** 19.

WOHLRAB, H., SIGNORETTI, S., RAMEH, L. E., DECONTI, D. K. & HANSEN, S. H. 2022. Mitochondrial transporter expression patterns distinguish tumor from normal tissue and identify cancer subtypes with different survival and metabolism. *Scientific Reports,* 12**,** 17035.

WYBRANSKA, I., POLUS, A., MIKOLAJCZYK, M., KNAPP, A., SLIWA, A., ZAPALA, B., STASZEL, T. & DEMBINSKA-KIEC, A. 2013. Apoptosis-related gene expression in glioblastoma (LN-18) and medulloblastoma (Daoy) cell lines. *Hum Cell,* 26**,** 137-48.

WYCKOFF, J. B., WANG, Y., LIN, E. Y., LI, J. F., GOSWAMI, S., STANLEY, E. R., SEGALL, J. E., POLLARD, J. W. & CONDEELIS, J. 2007. Direct visualization of macrophage-assisted tumor cell intravasation in mammary tumors. *Cancer Research,* 67**,** 2649-2656.

XUAN, W. J., XIA, Y. H., LI, T., WANG, L. L., LIU, Y. L. & TAN, W. H. 2020. Molecular Self-Assembly of Bioorthogonal Aptamer-Prodrug Conjugate Micelles for Hydrogen Peroxide and pH-Independent Cancer Chemodynamic Therapy. *Journal of the American Chemical Society,* 142**,** 937-944.

YAMADA, M., SHIMIZU, K., TAMURA, K., OKAMOTO, Y., MATSUI, Y., MORIUCHI, S., PARK, K., MABUCHI, E., YAMAMOTO, K., HAYAKAWA, T. & ET AL. 1989. [Establishment and biological characterization of human medulloblastoma cell lines]. *No To Shinkei,* 41**,** 695-702.

YANG, H. J., LI, M., DENG, Y. H., WEN, H. T., LUO, M. J. & ZHANG, W. M. 2024. Roles and interactions of tumor microenvironment components in medulloblastoma with implications for novel therapeutics. *Genes Chromosomes & Cancer,* 63**,** 13.

YURCHENCO, P. D. 2011. Basement Membranes: Cell Scaffoldings and Signaling Platforms. *Cold Spring Harbor Perspectives in Biology,* 3**,** 27.

ZELTZER, P. M., BOYETT, J. M., FINLAY, J. L., ALBRIGHT, A. L., RORKE, L. B., MILSTEIN, J. M., ALLEN, J. C., STEVENS, K. R., STANLEY, P., LI, H., WISOFF, J. H., GEYER, J. R., MCGUIRE-CULLEN, P., STEHBENS, J. A., SHURIN, S. B. & PACKER, R. J. 1999. Metastasis stage, adjuvant treatment, and residual tumor are prognostic factors for medulloblastoma in children: Conclusions from the Children's Cancer Group 921 randomized phase III study. *Journal of Clinical Oncology,* 17**,** 832-845.

ZHU, G. G., RISTELI, L., MAKINEN, M., RISTELI, J., KAUPPILA, A. & STENBACK, F. 1995. IMMUNOHISTOCHEMICAL STUDY OF TYPE-I COLLAGEN AND TYPE-I PN-COLLAGEN IN BENIGN AND MALIGNANT OVARIAN NEOPLASMS. *Cancer,* 75**,** 1010-1017.

ZHUKOVA, N., RAMASWAMY, V., REMKE, M., PFAFF, E., SHIH, D. J. H., MARTIN, D. C., CASTELO-BRANCO, P., BASKIN, B., RAY, P. N., BOUFFET, E., VON BUEREN, A. O., JONES, D. T. W., NORTHCOTT, P. A., KOOL, M., STURM, D., PUGH, T. J., POMEROY, S. L., CHO, Y. J., PIETSCH, T., GESSI, M., RUTKOWSKI, S., BOGNAR, L., KLEKNER, A., CHO, B. K., KIM, S. K., WANG, K. C., EBERHART, C. G., FEVRE-MONTANGE, M., FOULADI, M., FRENCH, P. J., KROS, M., GRAJKOWSKA, W. A., GUPTA, N., WEISS, W. A., HAUSER, P., JABADO, N., JOUVET, A., JUNG, S., KUMABE, T., LACH, B., LEONARD, J. R., RUBIN, J. B., LIAU, L. M., MASSIMI, L., POLLACK, I. F., RA, Y. S., VAN MEIR, E. G., ZITTERBART, K., SCHUELLER, U., HILL, R. M., LINDSEY, J. C., SCHWALBE, E. C., BAILEY, S., ELLISON, D. W., HAWKINS, C., MALKIN, D., CLIFFORD, S. C., KORSHUNOV, A., PFISTER, S., TAYLOR, M. D. & TABORI, U. 2013. Subgroup-Specific Prognostic Implications of TP53 Mutation in Medulloblastoma. *Journal of Clinical Oncology,* 31**,** 2927-+.

ZWERGEL, C., ROMANELLI, A., STAZI, G., BESHARAT, Z. M., CATANZARO, G., TAFANI, M., VALENTE, S. & MAI, A. 2018. Application of Small Epigenetic Modulators in Pediatric Medulloblastoma. *Frontiers in Pediatrics,* 6**,** 10.

Appendices

Appendix A – Designing Primers

SVCT2 primer designing

Primer pair 1 (Primer3)

FWD = **5' TAGCCCCGTGGTTTAAGGTT 3'** (exon 12)
REV = **5' CACAGGCGTAGTAGTCACCA 3'** (exon 13)

Primer size = 20bp (all annealed)
Product length = 132 bp
GC% content = 50% (fwd) + 55% (rev)

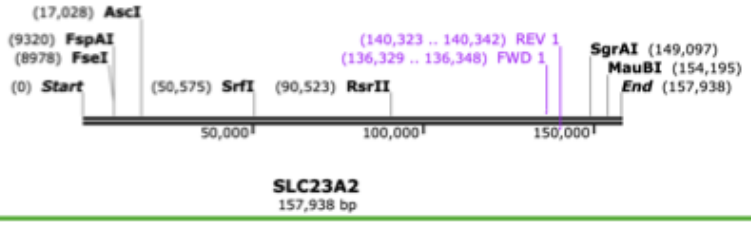

Primer pair 2 (Primer3)

FWD = **5' ACGTCCTTCTCACAACTGCT 3'** (exon 17)
REV = **5' CTTTGCCCACACCCTTCTTC 3'** (exon 18)

Primer size = 20bp (all annealed)
Product length = 120 bp
GC% content = 50% (fwd) + 55% (rev)

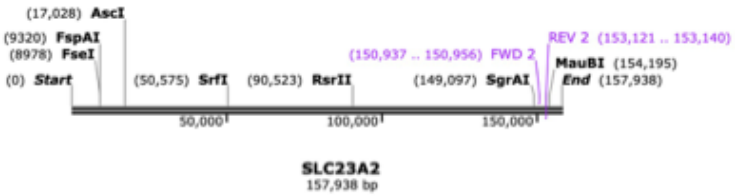

Primer pair 3 (NCBI primer BLAST)

FWD = **5' CATTTTGCAGGCGGCTGTCG 3'** (exon 2)
REV = **5' AGCCGTATGAGAAGTCCCCG 3'** (exon 3)

Primer size = 20bp (all annealed)
Product length = 143 bp
GC% content = 60% (fwd) + 60% (rev)

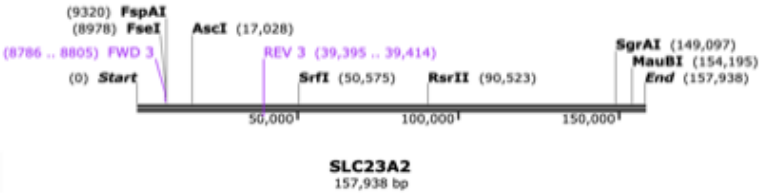

Primer pair 4 (NCBI primer BLAST)

FWD = **5' GCCAGCTAGGTCTTGACTCC 3'** (exon 3)
REV = **5' GATGTGGCGTAGACCTGTCC 3'** (exon 3)

Primer size = 20bp (19bp annealed) (FWD) + 20bp (all annealed) (REV)
Product length = 125bp
GC% content = 57.89% (fwd) + 60% (rev)

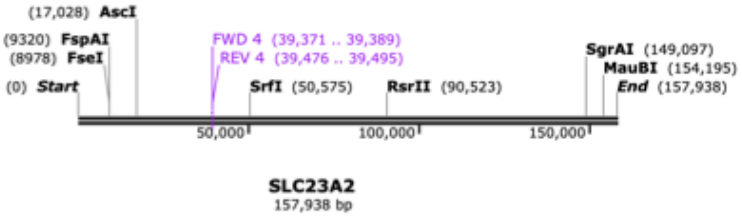

Figure A1. Shows information about the four SVCT2 primer pairs designed. Four primer pairs were designed for target gene SVCT2. Primer pairs 1 and 2 were designed using the Primer3 software whereas primer pairs 3 and 4 were designed using the NCBI primer BLAST tool. On the left-hand side of the figure shows the forward (FWD) and reverse (REV) primer sequences along with primer size, product length and the GC% content for both fwd and rev primers. On the right-hand side shows the map of the fwd and rev primers (in purple) located on the SLC23A2 (SVCT2) gene using the SnapGene® software (from Dotmatics; available at snapgene.com). Upon primer optimisation (**section 2.4.4**. and **Appendix B**) primer pair 1 (highlighted by green box) was chosen to be used for downstream experiments.

GLUT10 primer designing

Primer pair 1 (Primer3)

FWD = **5' CTTCTCCTTTGGGTTTGGGC 3'** (exon 4)
REV = **5' GAGATCGAGGAAGGAGAGGC 3'** (exon 5)

Primer size = 20bp (all annealed)
Product length = 142bp
GC% content = 55% (fwd) + 60% (rev)

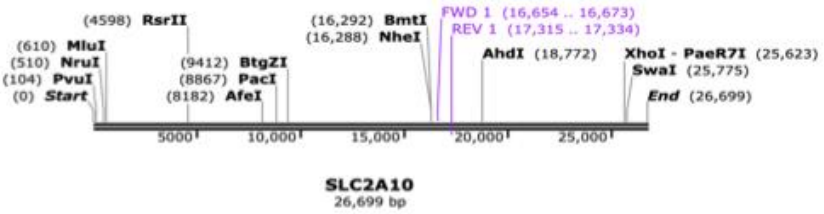

Primer pair 2 (Primer3)

FWD = **5' GCCTCTCCTTCCTCGATCTC 3'** (exon 5)
REV = **5' CTGCTGGTCTATCTCTGCCA 3'** (exon 6)

Primer size = 20bp (all annealed)
Product length = 146bp
GC% content = 60% (fwd) + 50% (rev)

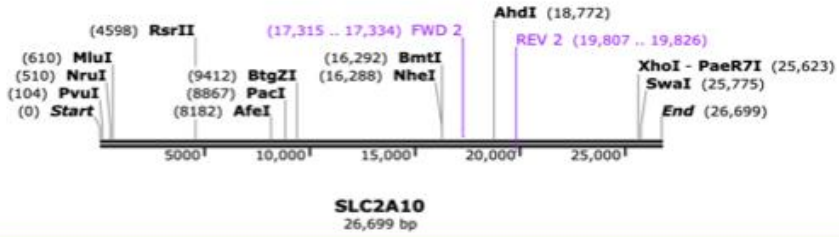

Primer pair 3 (NCBI primer BLAST)

FWD = **5' TGGTCTTTGTCAGTGCCTTC 3'** (exon 4)
REV = **5' GCTCTTCCTCGTATCTCCAC 3'** (exon 5)

Primer size = 20bp (all annealed)
Product length = 91bp
GC% content = 50% (fwd) + 55% (rev)

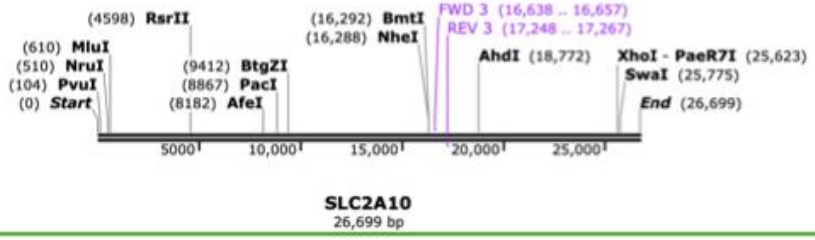

Figure A2. Shows information about the four GLUT10 primer pairs designed. Three primer pairs were designed for target gene GLUT10. Primer pairs 1 and 2 were designed using the Primer3 software whereas primer pair 3 was designed using the NCBI primer BLAST tool. On the left-hand side of the figure shows the forward (FWD) and reverse (REV) primer sequences along with primer size, product length and the GC% content for both fwd and rev primers. On the right-hand side shows the map of the fwd and rev primers (in purple) located on the SLC2A10 (GLUT10) gene using SnapGene® software (from Dotmatics; available at snapgene.com). Upon primer optimisation (**section 2.4.4**. and **Appendix B**) primer pair 3 (highlighted by green box) was chosen to be used for downstream experiments.

Appendix B – Primer Optimisation Data

Optimising Annealing Temperatures

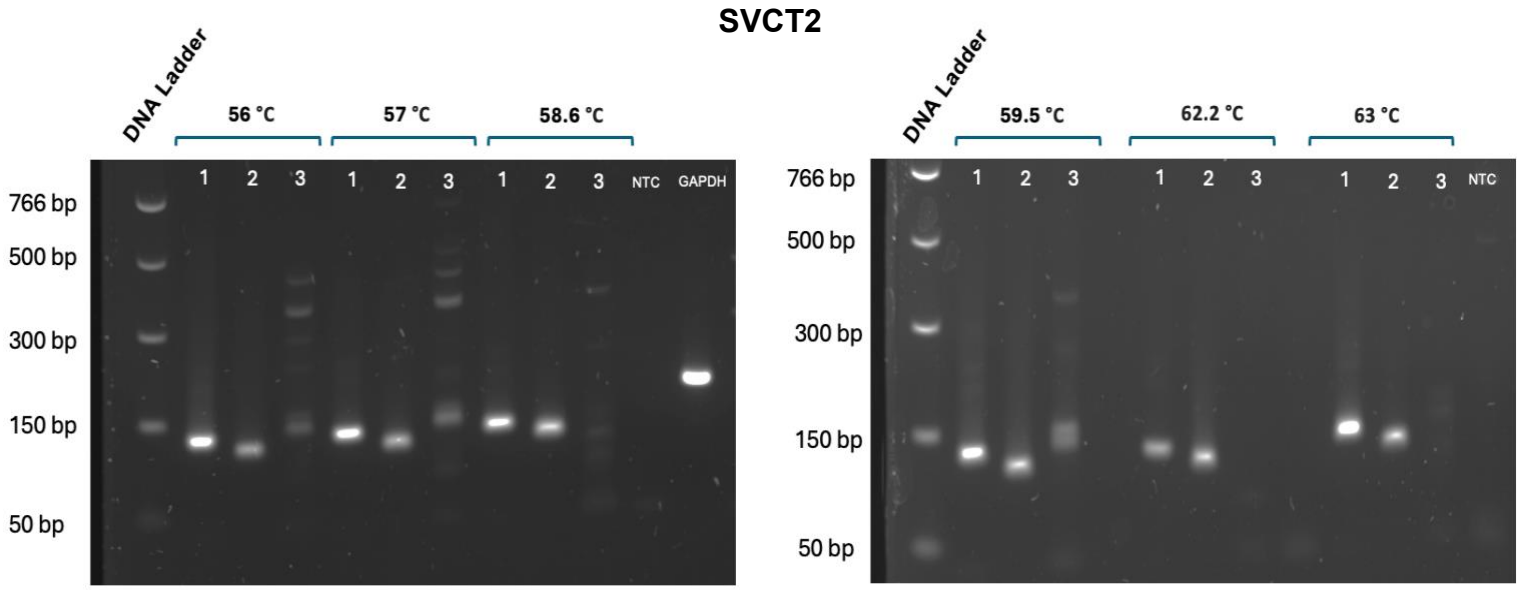

Figure B1. Gradient PCR analysis for optimising annealing temperatures for SVCT2 primers. Images from gel electrophoresis of initial gradient PCR products to detect optimal annealing temperatures for SVCT2 primer pairs, ran against a DNA ladder. Four primer pairs were originally designed for target gene SVCT2 (**Appendix A**) but only three pairs were used for gradient PCR which are labelled in image as 1, 2 and 3, which refers to primer pair 1, primer pair 2 and primer pair 3 respectively. Six different annealing temperatures were tested ranging from 56 °C to 63 °C. After initial gradient PCR, three temperatures were chosen to perform another set of gradient PCRs, narrowing down the temperatures to 58°C, 60.2°C and 62°C (shown in **figure 2.1.**). In this initial gel no template control (NTC) was ran to eliminate any reagent contamination, non-specific binding or primer dimer formation. GAPDH was ran as a positive control. Product sizes and primer sequences for each primer pair shown in **Appendix A**. GAPDH product size at 173 bp. Upon running initial gradient PCR, primer pair 1 was selected to be used for future experimentation (**section 2.4.6.**).

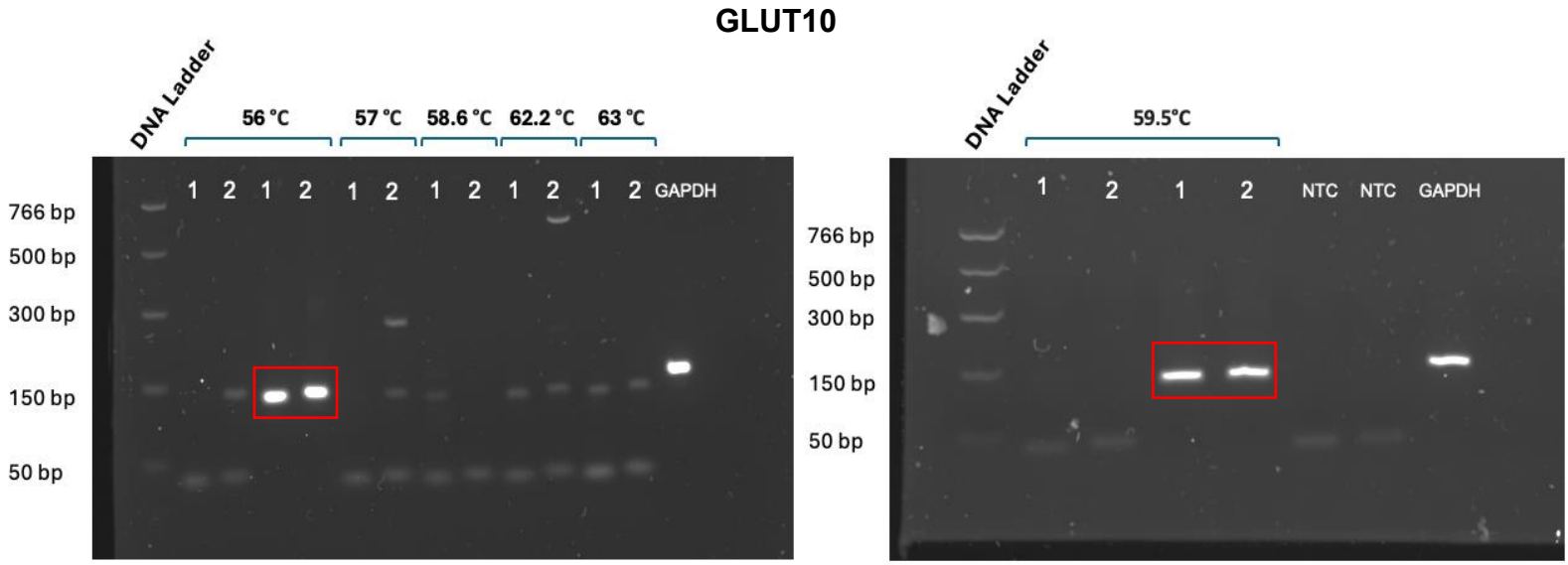

Figure B2. Gradient PCR analysis for optimising annealing temperatures for GLUT10 primers. Images from gel electrophoresis of initial gradient PCR products to detect optimal annealing temperatures for GLUT10 primer pairs, ran against a DNA ladder. Three primer pairs were originally designed for target gene GLUT10 (**Appendix A**) but only two pairs were used for gradient PCR which are labelled in image as 1 and 2, which refers to primer pair 1 and primer pair 2, respectively. Six different annealing temperatures were tested ranging from 56°C to 63°C. After initial gradient PCR, three temperatures were chosen to perform another set of gradient PCRs, narrowing down the temperatures to 58°C, 60.2°C and 62°C (shown in **figure 2.1.**). GLUT10 plasmid was used as a positive control to confirm amplification of target sequence by primers and shown in bright bands boxed in red. In this initial gel no template control (NTC) was ran to eliminate any reagent contamination, non-specific binding or primer dimer formation. However faint bands of low molecular weight were detected across all annealing temperatures and in NTC, suggesting presence of primer-dimers. Thus, third primer pair designed for GLUT10 was tested (**figure 2.1**). GAPDH was ran as a positive control. Product sizes and primer sequences for each primer pair shown in **Appendix A**. GAPDH product size at 173 bp. Upon running initial gradient PCR, primer pair 3 was selected to be used for future experimentation (**section 2.4.6.**).

Primer Efficiencies

Primer efficiencies of the designed SVCT2 and GLUT10 primer pairs were obtained via standard curve generated by a 5-fold serial dilution of cDNA template. The serial dilution of cDNA was prepared and amplified via reverse transcription quantitative PCR (RT-qPCR) (**table B1**) (**table B2**). To create the standard curve the Ct (cycle threshold) values obtained from the RT-qPCR were plotted against the logarithm of template concentration. Based upon the slope of the standard curve the following formula was used to determine primer efficiency:

$$Efficiency\ (\%) = \left(10^{\frac{-1}{Slope}} - 1\right) \times 100$$

Table B1: Reagents used for RT-qPCR.

Reagents	x1 reaction (µl)
SYBR Green (Bio-Rad, Cat **#1708880)**	10
10uM stock FWD primer (**final concentration 250nM**)	0.5
10uM stock REV primer (**final concentration 250nM**)	0.5
ddH_2O	8
cDNA (10ng/µl) / NRT / ddH_2O (NTC)	1
Total	20

Table B2: RT-qPCR thermocycler settings to generate melt curve.

Steps (with No. of cycles)		Time period	Temperature (°C)
Initial denaturation		2 minutes	95
x40	Denaturation	15 seconds	95
	Annealing	30 seconds	60
	Extension	30 seconds	72
Melt curve		Sections of 0.5°C increasing every 5 seconds	65-95

Primer efficiencies ranging from 90% to 110% were considered within range and are comparable**. Figure B3** shows primer efficiencies for SVCT2, GLUT10 and GAPDH and calnexin controls. Melt curve was generated to determine the accurate amplification of target gene, which assessed primer specificity (**figure B4**).

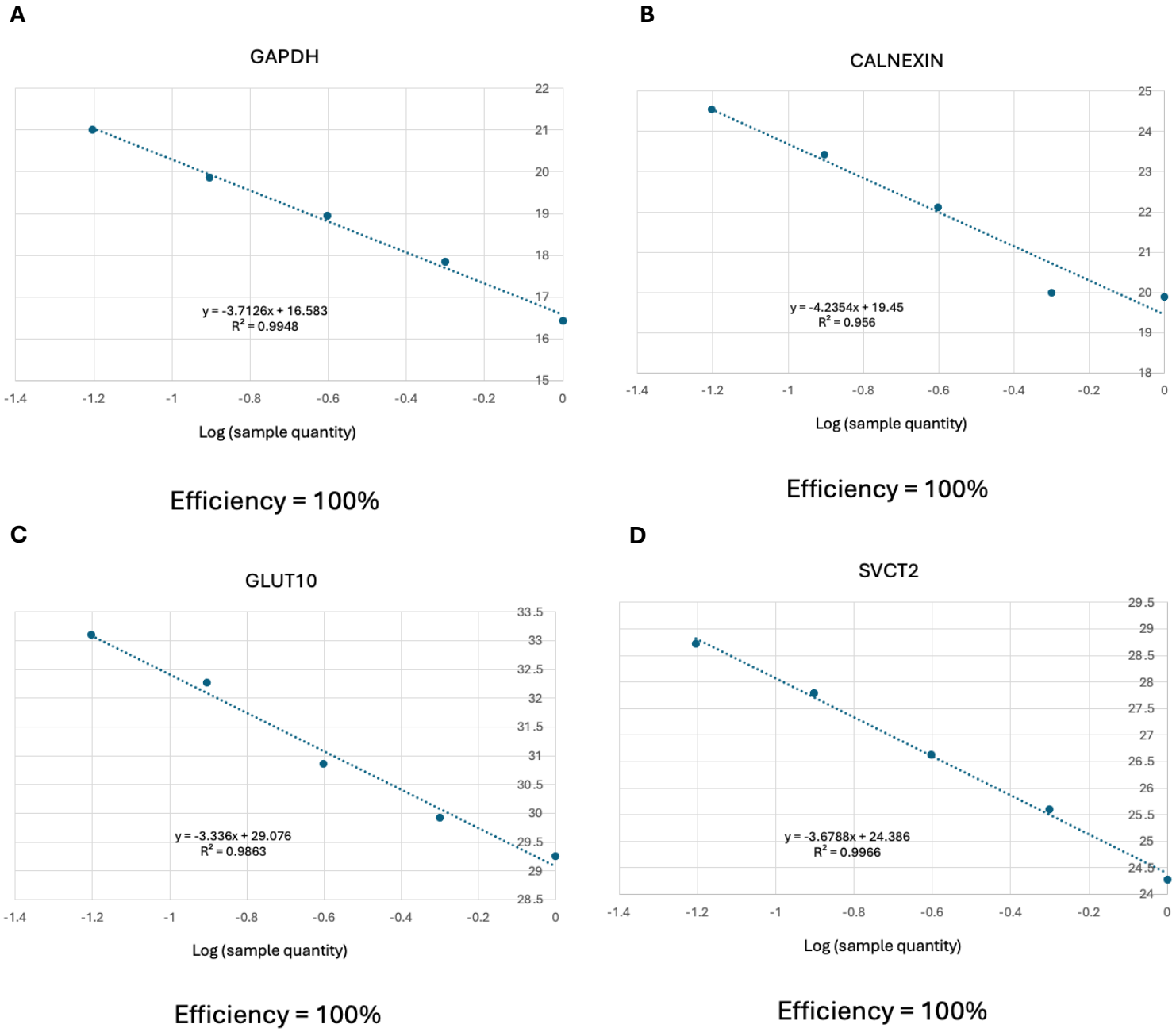

Figure B3. **Standard curves showing primer efficiencies for GAPDH, CALNEXIN, GLUT10 and SVCT2 primers.** Standard curves generated using serial dilution of cDNA template. Standard curved showing Ct values plotted against the log of sample quantity. Slope was determined via linear regression analysis, and the correlation coefficient (R^2) was calculated for each primer pair: GAPDH (**A**), CALNEXIN (**B**), GLU10 (**C**) and SVCT2 (**D**). Primer efficiencies were calculated using the slope and the above-mentioned equation. Efficiencies for all primers were obtained at 100% and strong linearity seen along the dilutions of cDNA template indicating good amplification and suitability of primer use for downstream gene expression experiments.

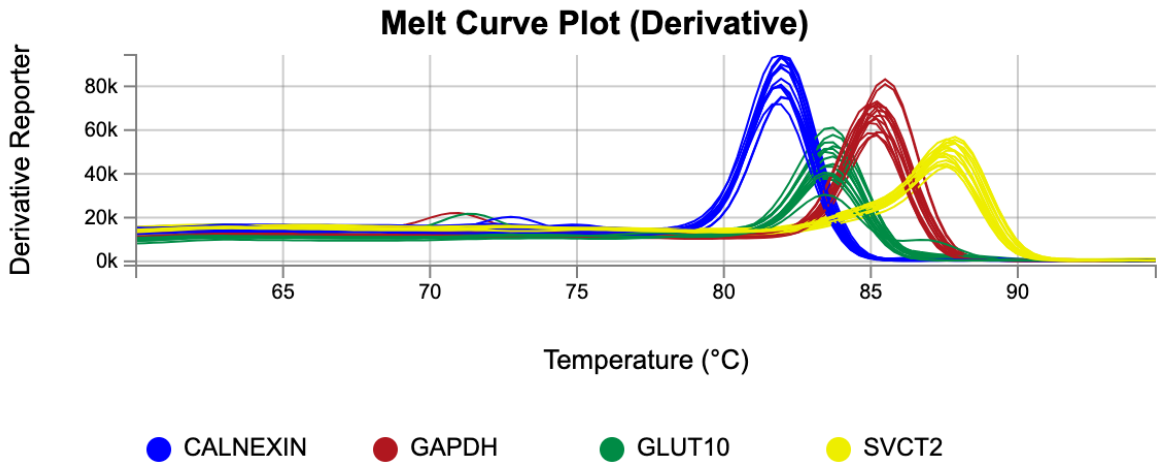

Figure B4. Melt curve analysis of CALNEXIN, GAPDH, GLUT10 and SVCT2. Melt curve was generated for all four primers to determine their specificity. All four primers generated distinct single peaks suggesting specific amplification of target genes CALNEXIN (blue), GAPDH (red), GLU10 (green) and SVCT (yellow) with minimum non-specific amplification. This melt curve confirmed the correct optimization of primers designed and the suitability of use for future RT-qPCR experiments. Melt curves representative of induvial experimental repeats.

Appendix C – Changes in Spheroid Size with AA and Cisplatin Co-Treatment

A

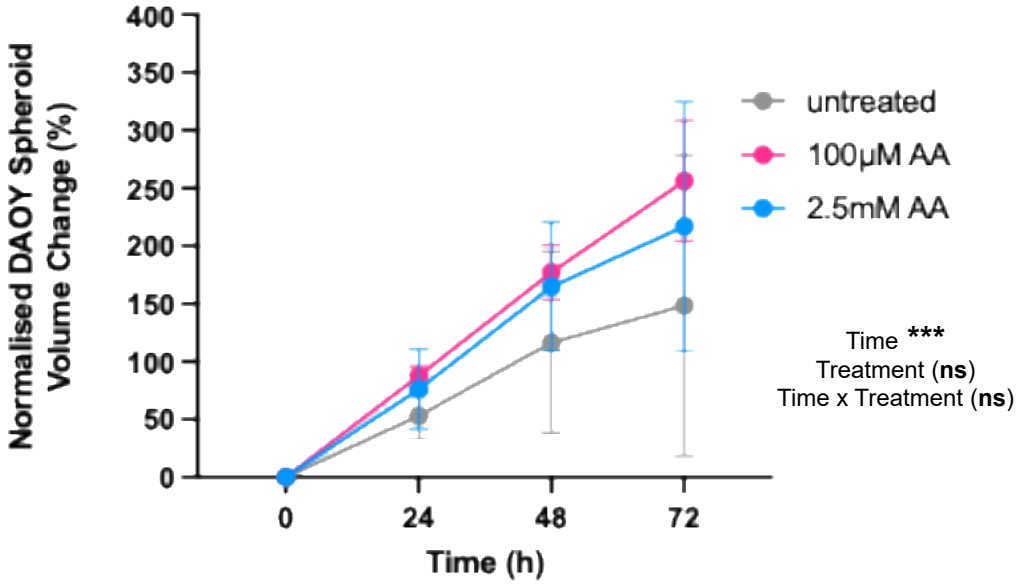

B

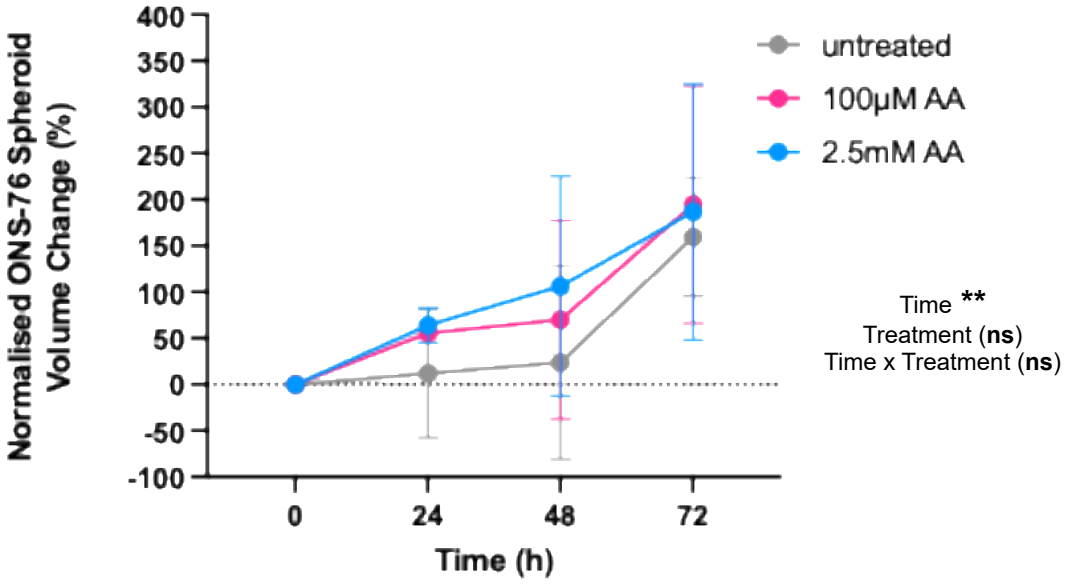

Figure C1. DAOY and ONS-76 spheroid estimated volume post treatment of physiological (100μM) AA and supraphysiological (2.5mM) AA. Figure shows the percentage change in estimated volume for DAOY spheroids (**A**), and ONS-76 spheroids (**B**) treated with 100μM and 2.5mM doses of AA over a time course (0, 24, 48 and 72 h). Spheroid volumes were normalised to that of pre-treatment (0 h). Data represents the mean ± SD (error bars); n=3 with 3 internal replicates per experiment. Untreated control - grey; 100μM AA - pink; 2.5mM AA - blue. A mixed-effects model with treatment and time as fixed effects and Geisser-Greenhouse correction (DAOY epsilon = 0.48; ONS-76 epsilon = 0.42) for sphericity variation and Tukey's multiple comparison test was used for statistical analysis. For DAOY spheroids (**A**) there was no statistically significant treatment effect (*p>0.05, p=0.38 (ns)*) or time and treatment interaction (*p>0.05, p=0.70 (ns)*). Time alone was found to have a substantial influence (*p<0.05, p=0.0002 (****)) on spheroid growth. For ONS-76

spheroids (**B**) there was no statistically significant treatment effect (*p>0.05, p=0.71 (ns)*) or time and treatment interaction (*p>0.05, p=0.95 (ns)*). Time alone was found to have a significant influence (*p<0.05, p=0.0059 (***)*) on spheroid growth. Any non-significant pairwise comparisons not shown.

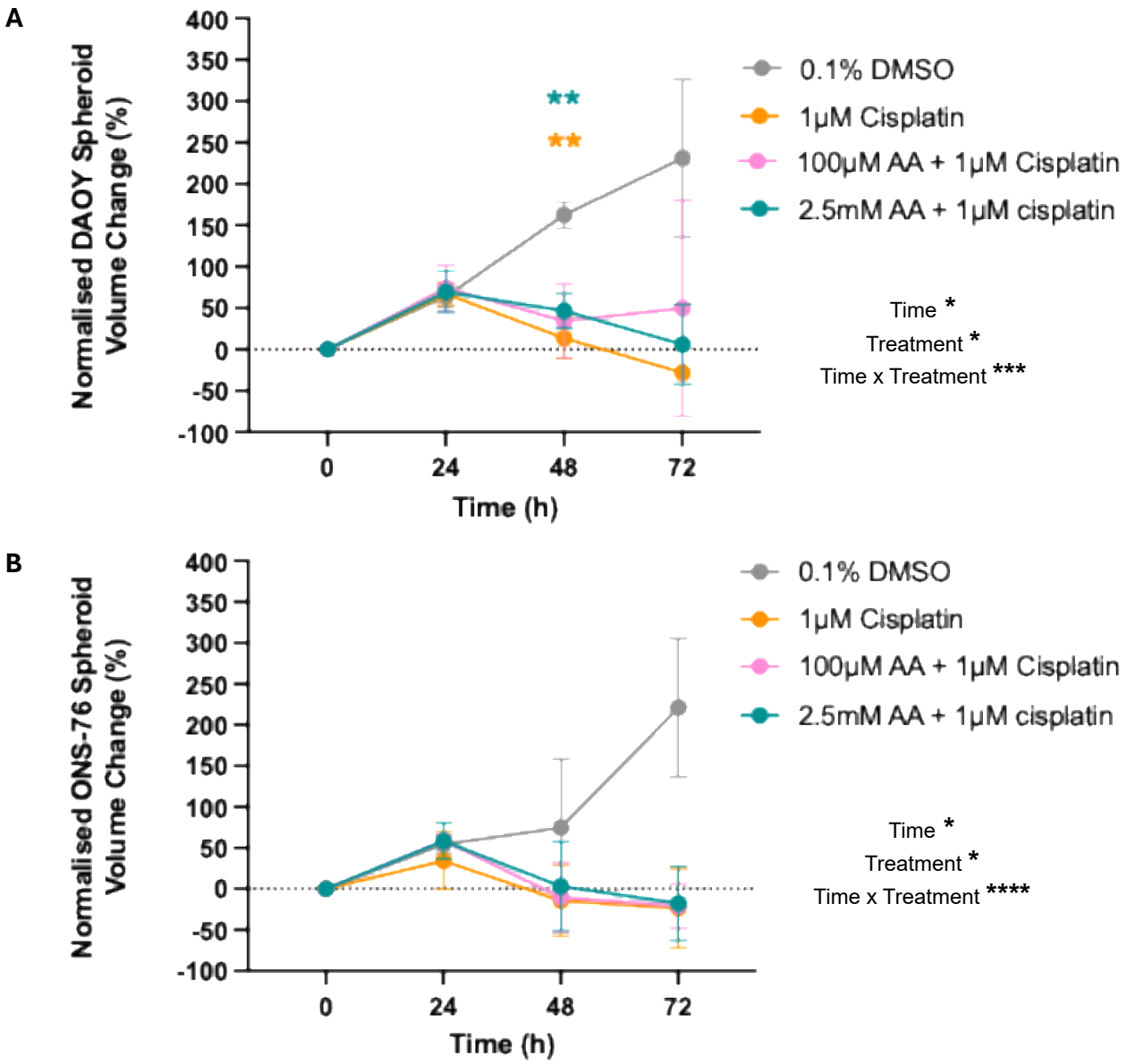

Figure C2. DAOY and ONS-76 spheroid estimated volume post treatment with cisplatin alone and in combination with physiological (100μM) AA and supraphysiological (2.5mM) AA. Figure shows the percentage change in estimated volume for DAOY spheroids (**A**), and ONS-76 spheroids (**B**) treated with 1μM cisplatin alone or as co-treatment with 100μM AA and 2.5mM AA over a time course (0, 24, 48 and 72 h). Spheroid volumes were normalised to that of pre-treatment (0 h). Data represents the mean ± SD (error bars); n=3 with 3 internal replicates per experiment. 0.1% DMSO control - grey; 1μM cisplatin – orange; 100μM AA + 1μM cisplatin - pink; 2.5mM AA + 1μM cisplatin - teal. A mixed-effects model with treatment and time as fixed effects and Geisser-Greenhouse correction (DAOY epsilon = 0.38; ONS-76 epsilon = 0.52) for sphericity variation and Tukey's multiple

comparison test was used for statistical analysis. For DAOY spheroids (**A**) time alone was found to have a significant effect on spheroid growth (*p<0.05, p=0.016 (**)*). Treatment alone (*p<0.05, p=0.015 (**)*) had a significant effect on spheroid growth. There was a substantial significant effect of time and treatment interaction on spheroid growth (*p<0.05, p=0.0002 (***)*). For ONS-76 spheroids (**B**) time alone also had a significant effect on volume (*p<0.05, p=0.017 (**)*). Treatment alone also had effect on ONS-76 spheroid volume (*p<0.05, p=0.024 (**)*). The interaction between time and treatment on ONS-76 spheroid volume was also significant (*p<0.05, p<0.0001 (****)*). Tukey's multiple comparison test revealed significant difference in DAOY spheroid volume between control group (0.1% DMSO) and 1μM cisplatin treatment groups at 48 h timepoint (shown by orange asterisks, *p<0.05, p=0.007*) and between control group and 2.5mM AA + 1μM cisplatin treatment group at 48h timepoint (shown by teal asterisks, *p<0.05, p=0.007*) (**A**). Tukey's multiple comparison test ran on ONS-76 spheroid area revealed significant no difference in spheroid volumes between all different treatment groups at any timepoint. Any non-significant pairwise comparisons not shown.

Appendix D - Inhibiting AA/DHA Uptake in Treated Spheroids

Spheroids were treated with a triple treatment of AA, cisplatin and either a SVCT2 specific inhibitor (sulfinpyrazone) or a panGLUT inhibitor (cytochalasin B) (**table D1**).

Optimising AA/DHA Inhibitor Concentration

To assess the cytotoxic effects and to determine the non-toxic concentrations of sulfinpyrazone and cytochalasin B on DAOY and ONS-76 spheroids, spheroids were incubated with varying inhibitor doses for 24-, 48- and 72-hour timepoints.
The concentrations of sulfinpyrazone used were 0mM, 10μM, 30μM, 100μM, 300μM, 1mM, and 3mM. The concentrations of cytochalasin B used were 0μM, 0.05μM, 0.5μM, 1μM, 5μM, 10μM, and 50μM; these concentration ranges were established using data from existing literature. Toxicity of inhibitors was validated using a live/dead staining (CAM/PI) (**section 2.6**). Based on these findings, sulfinpyrazone and cytochalasin B concentrations that did not substantially impair spheroid viability were chosen for ascorbic acid and cisplatin combination treatment.

AA/DHA Inhibitor, AA and Cisplatin Combination Treatment

Following the inhibitor dose-dependent toxicity test, the non-toxic concentration of sulfinpyrazone and cytochalasin B were used at 30μM and 5μM, respectively. DAOY and ONS-76 spheroids were generated to day 4 as per methods stated in **section 2.2.2**. All treatment solutions were made in microcentrifuge tubes using neurosphere medium at a 2× concentration and administered to spheroids as mentioned in **section 2.5**. Untreated and 0.1% DMSO were used as controls and following were used as treatment groups:

Combination Treatment Groups
Untreated (media only)
0.1% DMSO
100μM AA + 30μM sulfinpyrazone
2.5mM AA + 30μM sulfinpyrazone
100μM AA + 30μM sulfinpyrazone + 1μM cisplatin
2.5mM AA + 30μM sulfinpyrazone + 1μM cisplatin
100μM AA + 5μM cytochalasin B
2.5mM AA + 5μM cytochalasin B
100μM AA + 5μM cytochalasin B + 1μM cisplatin
2.5mM AA + 5μM cytochalasin B + 1μM cisplatin

Treated spheroids were incubated in a humidified environment with 5% CO_2 at 37°C. Spheroid morphology and size were obtained and analysed using ZOE Fluorescent Cell Imager at 0 (pre-treatment), 24, 48, and 72 h post treatment (**section 2.5.1**). Effect of the combination therapy on spheroid viability was measured with live dead staining of treated spheroids **(section 2.6**).

Table D1. Details of sulfinpyrazone and cytochalasin B used in this experiment.

Compound	Stock	Vehicle	Storage	Product Details
Sulfinpyrazone	5g	DMSO	Powder = room temperature, protected from light Stock solution = -20℃ freezer	Sigma-Aldrich, S9509
Cytochalasin B	10mg/mL	DMSO	Stock solution = -20℃ freezer	Sigma-Aldrich, C2743

Investigating AA Transporter Modulation in Cisplatin Cytotoxicity

When combined with cisplatin, SHH spheroids responded differently to physiological and supraphysiological ascorbic acid (AA) concentrations, indicating that the intracellular availability of AA may be crucial in determining its cytotoxic or cytoprotective effects. Using pharmacological inhibitors that target the sodium-dependent vitamin C transporter 2 (SVCT2) and the facilitative glucose transporters (GLUTs)—a preliminary viability study was carried out to determine whether this was mediated through AA transport.

The uptake of the reduced form of AA is inhibited by sulfinpyrazone, a known non-selective SVCT2 inhibitor (Portugal, 2024). There was no specific GLUT10 inhibitor found in order to prevent DHA absorption by several GLUT isoforms, including GLUT10 therefore cytochalasin B, a broad-spectrum pan-GLUT inhibitor was used (Kapoor et al., 2016). DAOY and ONS-76 spheroids were treated with 1μM cisplatin in conjunction with either 100μM (physiological) or 2.5mM (supraphysiological) AA and 30μM sulfinpyrazone or 5μM cytochalasin B. The concentrations of inhibitors were previously optimised to limit toxicity to spheroids, as mentioned above.

Brightfield images were taken of DAOY and ONS-76 spheroids after each timepoint (0, 24, 48 and 72 h of treatment) (**figure D1**). Spheroid disintegration was seen as early as 24 h after DAOY spheroids (**figure D1 (A)**) were treated with cisplatin and sulfinpyrazone without the presence of AA. It was interesting to note that adding 100μM AA to this mixture resulted in more noticeable spheroid disassociation at 72 h compared to adding 2.5mM AA. This suggests that the inhibition of the transporter may worsen AA-mediated disruption to spheroid integrity at physiological levels of AA, while at supraphysiological AA levels, may lessen this effect. On the other hand, the opposite was observed in the absence of cisplatin where the disassociation of DAOY spheroids was increased in 2.5mM AA and sulfinpyrazone treatment group than in the 100μM AA and sulfinpyrazone treatment group. This suggests that supraphysiological AA under transporter inhibition becomes destabilising even in the absence of chemotherapy. These findings suggest that SVCT2-mediated uptake may

be essential for preserving redox equilibrium in SHH-medulloblastoma spheroids. Conversely, the same effect of sulfinpyrazone was not seen on ONS-76 spheroids as seen in DAOY spheroids. Treatment with sulfinpyrazone in combination with either ascorbic acid or cisplatin stopped spheroid growth, in contrast to untreated spheroids, which kept growing over the course of the 72-hour period (**figure D1 (B)**). This may be the case due the modest difference seen in SVCT2 expression between DAOY and ONS-76 (**figure 4.2**).

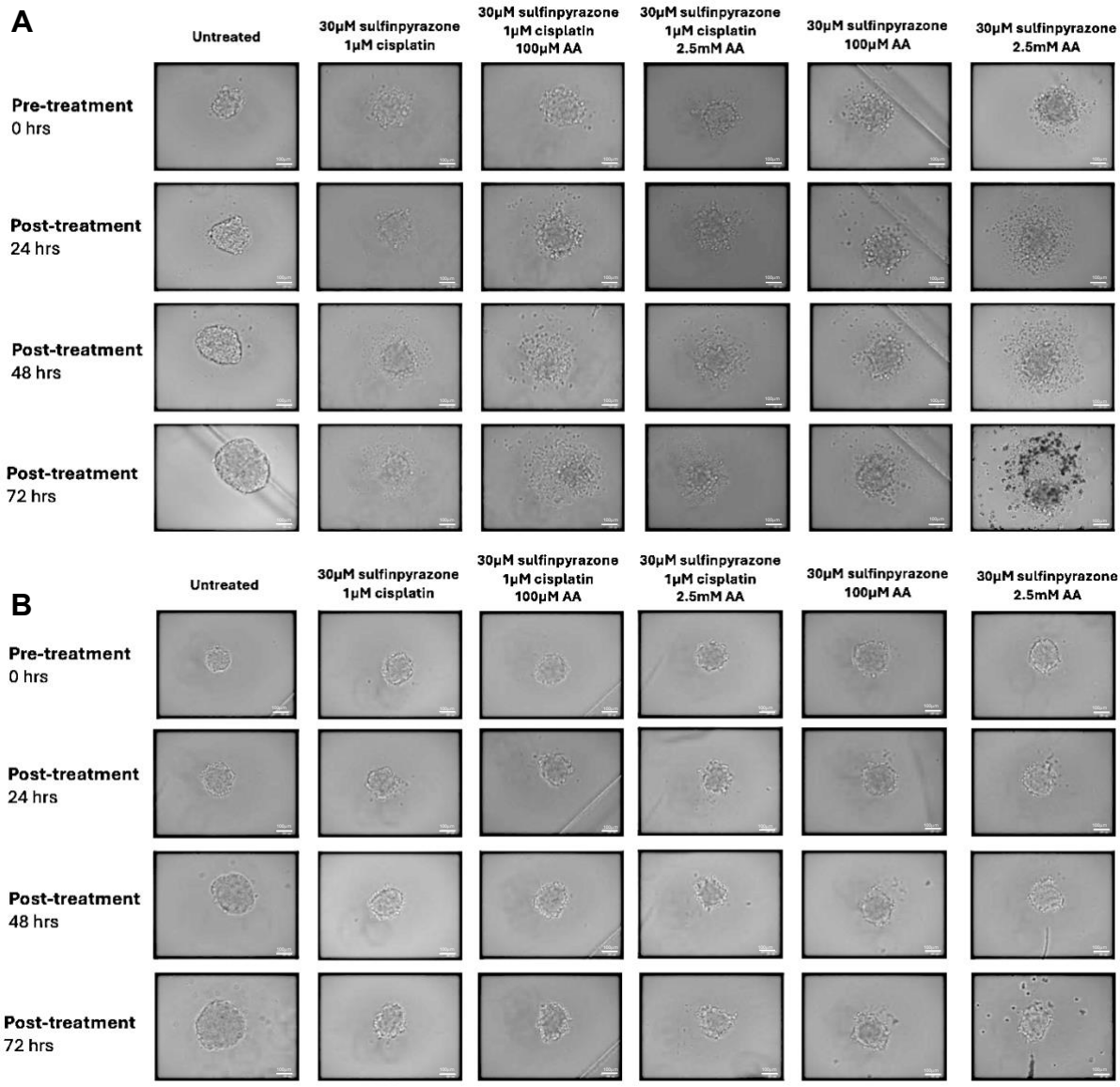

Figure D1. Effect of sulfinpyrazone as a non-selective SVCT2 inhibitor with AA and cisplatin co-treatment on DAOY and ONS-76 spheroids. Representative brightfield images of DAOY (**A**) and ONS-76 (**B**) spheroids treated with; media only (untreated), 30μM sulfinpyrazone + 100μM AA or 2.5mM AA alone and with or without 1μM cisplatin over a 72-hour time course. Addition of sulfinpyrazone to AA and cisplatin treatment produced subsequent spheroid disintegration in DAOY spheroids, however in ONS-76 caused no spheroid disintegration but inhibited overall spheroid growth. n=2 with triple internal replicates. Scale bar = 100μm.

SVCT2 has a mechanistic function in tumour biology. When entry of AA into cells is restricted by decreased or dysregulated SVCT2 expression it lowers the intracellular antioxidant capacity of the tumour cell and maintains hypoxia-inducible factor (HIF)-dependent signalling, which promotes cancer survival and aggressiveness in hypoxic environments (Burgess et al., 2025, Campbell et al., 2015). However, it has been demonstrated that restoring intracellular AA via SVCT2 overexpression or supplementation destabilises HIF-1α, suppresses glycolytic metabolism, and increases tumour sensitivity to chemotherapeutic drugs (Corti et al., 2010). Cytochalasin B was used as a pan-GLUT inhibitor to prevent GLUT mediated uptake of DHA, the oxidised form of AA. DAOY and ONS-76 spheroids were treated with 5μM of cytochalasin B with cisplatin or 100μM/2.5mM AA alone or all three components combined (**figure D2**). Cytochalasin B treatment in conjunction with cisplatin caused early spheroid disintegration within 24 h, which was comparable to the effects seen with sulfinpyrazone. Spheroid disassociation was more noticeable in DAOY spheroids than compared with ONS-76 spheroids. At physiological concentrations of AA with cisplatin, inhibiting GLUT transporters with cytochalasin B, increased cytotoxic stress in DAOY spheroids, compared to 2.5mM AA – as seen earlier with inhibiting SVCT2. In the absence of cisplatin, DAOY spheroids treated with cytochalasin B and 100μM AA qualitatively showed more compromised spheroid viability than compared to cytochalasin B with 2.5mM AA.

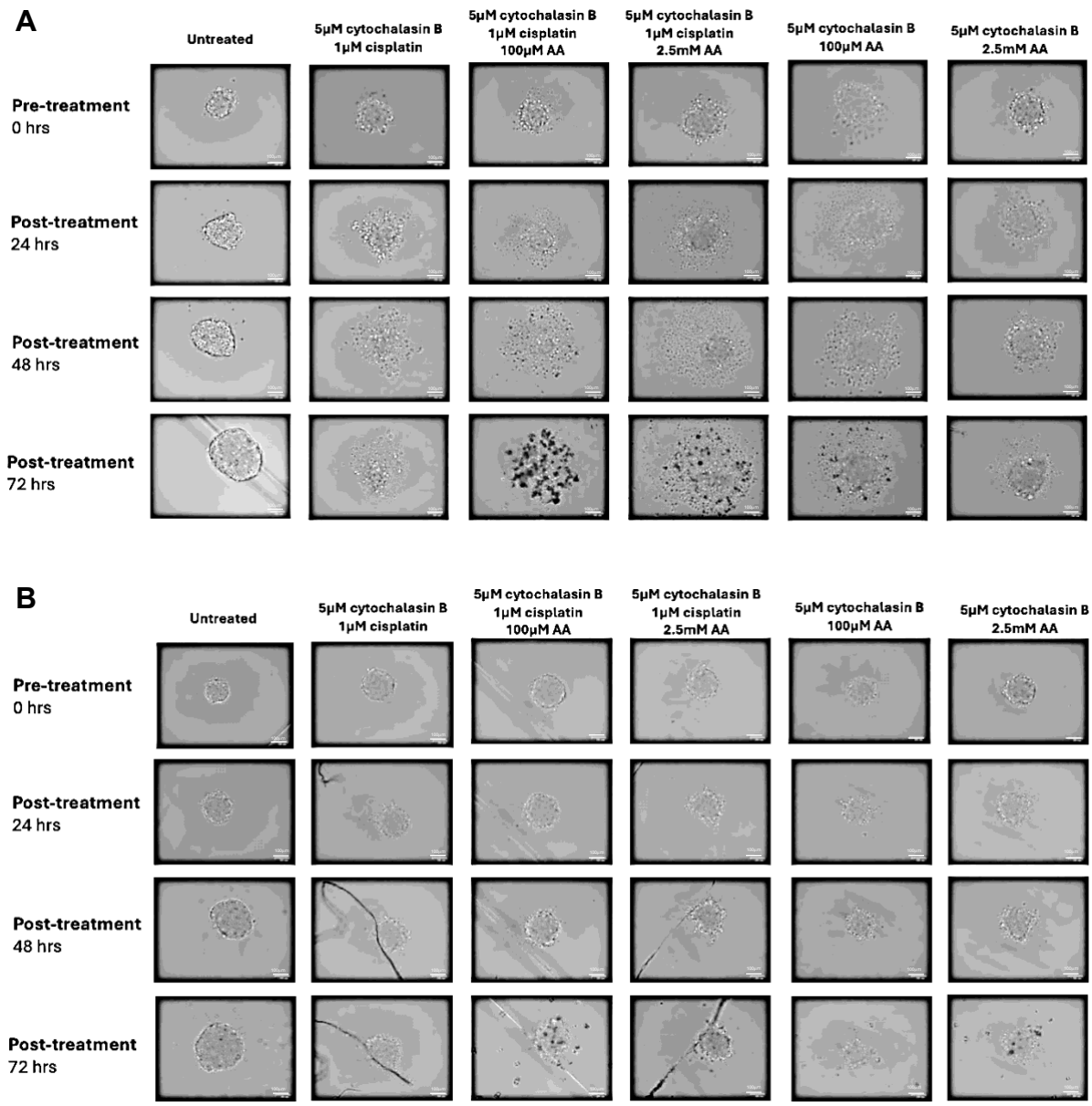

Figure D2. Effect of cytochalasin B as a panGLUT inhibitor with AA and cisplatin co-treatment on DAOY and ONS-76 spheroids. Representative brightfield images of DAOY (**A**) and ONS-76 (**B**) spheroids treated with; media only (untreated), 5μM cytochalasin B + 100μM AA or 2.5mM AA alone and with or without 1μM cisplatin over a 72-h time course. Addition of cytochalasin B to AA and cisplatin treatment produced increased spheroid disintegration in DAOY spheroids in comparison to ONS-76 spheroids. n=2 with triple internal replicates. Scale bar = 100μm.